

Magneto-Optical Investigations of Lead-Free Metal Halide Perovskite Nanocrystals

by

Lin Feng

A thesis
presented to the University of Waterloo
in fulfillment of the
thesis requirement for the degree of
Master of Science
in
Chemistry

Waterloo, Ontario, Canada, 2024

© Lin Feng 2024

Author's Declaration

I hereby declare that I am the sole author of this thesis. This is a true copy of the thesis, including any required final revisions, as accepted by my examiners.

I understand that my thesis may be made electronically available to the public.

Abstract

Inorganic lead-free metal halide perovskites have garnered much attention as low-toxicity alternatives to lead halide perovskite for luminescence and photovoltaic applications. However, the electronic structure and properties of these materials, including the composition dependence of the band structure, spin-orbit coupling, and Zeeman effects remain poorly understood. In this thesis, we focus on two specific systems: $\text{Cs}_3\text{Bi}_2\text{X}_9$ ($\text{X} = \text{Cl}, \text{Br}$) and double perovskite, including $\text{Cs}_2\text{AgBiX}_6$ ($\text{X} = \text{Cl}, \text{Br}$), $\text{Cs}_2\text{AgInCl}_6$ and its Bi-alloyed analogue ($\text{Cs}_2\text{AgIn}_{0.5}\text{Bi}_{0.5}\text{Cl}_6$). Using magnetic circular dichroism (MCD) spectroscopy, we investigate the electronic structure, magneto-optical properties, and excitonic transitions in these lead-free perovskite NCs. Our results reveal that the excitonic spectra of $\text{Cs}_3\text{Bi}_2\text{X}_9$ are predominantly characterized by both direct and indirect band-gap transitions, with only a minor contribution from excitons localized on Bi^{3+} sites. In contrast, the excitonic transitions in $\text{Cs}_2\text{AgBiX}_6$ are primarily derived from direct free- and bound- exciton transition. Additionally, our results demonstrate that halide composition significantly influences the Zeeman splitting energy and g-factors, with $\text{Cs}_3\text{Bi}_2\text{Br}_9$ and $\text{Cs}_2\text{AgBiBr}_6$ exhibiting stronger spin-orbit coupling compared to their chloride counterparts. Moreover, introducing bismuth ion (Bi^{3+}) into $\text{Cs}_2\text{AgInCl}_6$ NCs can enhance the spin-orbit coupling and modify the electronic structure, demonstrating the potential for compositional tuning to optimize these materials for specific applications. Furthermore, temperature-dependent MCD measurements were conducted to further explore the excitonic behavior of these materials, providing insights into their suitability

for further applications. In conclusion, this thesis provides detailed insights into lead-free halide perovskite NCs, emphasizing their potential as environmentally friendly alternatives to lead-based perovskite. These findings offer valuable guidance for the design of low-toxicity, high-performance materials for applications in spintronics, photovoltaics, and optoelectronics.

Acknowledgements

As I reach the end of my master's research, I am filled with gratitude for the guidance and support that I have received along the way.

First and foremost, I would like to express my appreciation to my supervisor, Dr. Pavle Radovanovic. His unwavering support, despite his busy schedule, was instrumental in guiding me through this journey. Our regular meetings helped me address my questions and provided essential guidance on the direction of my research. Additionally, I am deeply grateful for the meticulous feedback he offered on my papers and thesis. This journey would not have been possible without his guidance. I would also like to extend my thanks to Dr. Rodney Smith. From CHEM 313 to CHEM 494, and then throughout my pursuit of a master's degree, his consistent support has been a cornerstone of my academic journey. His encouragement and guidance have been crucial in shaping my research and academic growth. Additionally, I would like to express my gratitude to my other committee member, Dr. Vivek Maheshwari, for his support during the seminar and for the valuable feedback he provided on my thesis and research. Additionally, I would like to thank the members of our group for their encouragement and suggestions. I am especially grateful to I-Hsuan Yeh for her guidance and instruction during the experiment. Lastly, I would like to thank my family, friends, and my boyfriend for their care and love, and for being there to support me during my difficult moments.

Table of Contents

Author's Declaration	ii
Abstract	iii
Acknowledgements	v
List of Figures	ix
List of Abbreviations	xv
Chapter 1. Introduction	1
1.1 Background	1
1.1.1 Semiconductor Nanocrystals	1
1.1.2 Absorption	2
1.1.3 Excitons	3
1.1.4 Phonon	4
1.1.5 Recombination and luminescence	5
1.2 Lead Halide Perovskites Semiconductor	6
1.3 Lead-free perovskite materials	8
1.3.1 Cesium Bismuth Halide NCs $\text{Cs}_3\text{Bi}_2\text{X}_9$	9
1.3.2 Halide Double Perovskites (HDPs)	11
1.4 Spintronics	16
1.6 Theoretical basis for Magnetic Circular Dichroism (MCD)	18
1.6 Motivations and Scope of the Thesis	20
Chapter 2 Experimental Section	23

2.1 Material	23
2.2 Synthesis	23
2.2.1 Cs ₃ Bi ₂ X ₉ Nanocrystal Synthesis	23
2.2.2 Cs ₂ AgBiX ₆ Nanocrystal Synthesis	24
2.2.3 Cs ₂ AgIn _{1-x} Bi _x Cl ₆ Nanocrystal Synthesis	25
2.3 Measurement and Data Analysis	25
2.3.1 Powder X-ray Diffraction	25
2.3.2 Transmission Electron Microscopy (TEM)	26
2.3.3 UV-Vis-NIR Spectroscopy	26
2.3.4 Magnetic Circular Dichroism (MCD)	26
Chapter 3 Magneto optical properties of Cs ₃ Bi ₂ Cl ₉ and Cs ₃ Bi ₂ Br ₉	30
3.1 Structural characterization of Cs ₃ Bi ₂ Cl ₉ and Cs ₃ Bi ₂ Br ₉ NCs	30
3.2 Optical properties of Cs ₃ Bi ₂ Cl ₉ and Cs ₃ Bi ₂ Br ₉ NCs	32
3.3 Magneto-Optical properties of Cs ₃ Bi ₂ Cl ₉ and Cs ₃ Bi ₂ Br ₉ NCs	33
3.4 Conclusion	39
Chapter 4 Magneto optical properties of double perovskites	41
4.1 Cs ₂ AgBiX ₆ NCs	41
4.1.1 Structural characterization of	41
4.1.2 Optical properties of Cs ₂ AgBiCl ₆ and Cs ₂ AgBiBr ₆ NCs	42
4.1.3 Magneto-Optical properties of Cs ₂ AgBiCl ₆ and Cs ₂ AgBiBr ₆ NCs	44
4.2 Cs ₂ AgInCl ₆ NCs	50
4.2.1 Structural characterization of Cs ₂ AgInCl ₆ NCs	50

4.2.2 Optical and Magneto-optical properties of Cs ₂ AgInCl ₆ NCs	51
4.3 Cs ₂ AgIn _{0.5} Bi _{0.5} Cl ₆ NCs	54
4.3.1 Structural characterization of Cs ₂ AgIn _{0.5} Bi _{0.5} Cl ₆ NCs	54
4.3.2 Optical and Magneto-optical properties of Cs ₂ AgIn _{0.5} Bi _{0.5} Cl ₆ NCs	56
4.4 Conclusion	59
Chapter 5 Conclusion and Future Work	61
References	64
Appendix	84
Appendix A	84
Deconvolution for vacancy-ordered perovskites NCs	84
Appendix B	86
Deconvolution for double perovskites NCs	86

List of Figures

Figure 1.1 Schematic diagram of direct versus indirect interband absorptions in Si. Reproduced from Ref. [5].....	2
Figure 1.2 Schematic of Wannier excitons (Mott) and Frenkel excitons. Reproduced from Ref. [9].....	4
Figure 1.3 Schematic diagram for Metal halide perovskite ABX_3 . Reproduced from Ref. [21].....	6
Figure 1.4 Schematic diagram of different substitution methods and consequences. Reproduced from Ref. [44].....	9
Figure 1.5 Schematic diagram of crystal structure of $Cs_3Bi_2X_9$ at room temperature. Gray atoms represent Bi, blue atoms represent halide ion, and purple atoms represent Cs. Reproduced from Ref. [27].....	10
Figure 1.6 Schematic diagram of crystal structure of DPs and potential substitutions approaches. Reproduced from Ref.[60].....	12
Figure 1.7 Electron band structure of $Cs_2AgInCl_6$ with parity of transitions. Reproduced from Ref. [78].....	15
Figure 1.8 Mechanisms of a) A, b) B, and c) C terms in MCD. Dashed curves represent the absorption of LCP (positive) and RCP (negative) light. The solid lines represent the resultant MCD responses. Reproduced from Ref. [111].....	19
Figure 2.1 Schematic diagram of MCD Experimental Setup. In MCD spectroscopy, light from a broadband source is directed through a monochromator and polarizer to produce a	

monochromatic, linearly polarized beam. This beam is then partially passed through a photoelastic modulator, generating left circularly polarized (LCP) and right circularly polarized (RCP) light. The sample is settled within a superconducting magneto-optical cryostat, with the magnetic field lines oriented parallel to the direction of light propagation. As the LCP and RCP light pass through the sample, they are absorbed to different degrees according to the absorption coefficients, resulting in different intensities. These differing intensities combine to form an elliptically polarized beam. The ellipticity (θ) is defined as the angle between the major and minor axes of the ellipse. Reproduced from ref. [116].26

Figure 3.1 PXRD patterns of $\text{Cs}_3\text{Bi}_2\text{X}_9$ NCs compared to reference patterns of $\text{Cs}_3\text{Bi}_2\text{Cl}_9$ (tetragonal, ICSD Coll. Code 432491) and $\text{Cs}_3\text{Bi}_2\text{Br}_9$ (tetragonal, ICSD Coll. Code 1142). The bottom gray line represents the reference patterns of $\text{Cs}_3\text{Bi}_2\text{Cl}_9$ with a Pmcn space group (orthorhombic, ICSD Coll. Code 2067). 31

Figure 3.2 TEM characterization of (a) $\text{Cs}_3\text{Bi}_2\text{Cl}_9$ and (b) $\text{Cs}_3\text{Bi}_2\text{Br}_9$ NCs. 32

Figure 3.3 Absorption spectra of (a) $\text{Cs}_3\text{Bi}_2\text{Cl}_9$ and (b) $\text{Cs}_3\text{Bi}_2\text{Br}_9$ NCs collected at 5 K. .33

Figure 3.4 Optical absorption (top) and MCD (bottom) spectra of (a) $\text{Cs}_3\text{Bi}_2\text{Cl}_9$ NCs and (b) $\text{Cs}_3\text{Bi}_2\text{Br}_9$ NCs in the band gap region, collected at 7 T and 5 K. (Legend: black line - normalized MCD data; pink line - cumulative peak; green line - simulated direct transition; purple line - simulated indirect transition; orange line - Bismuth s-p transition)35

Figure 3.5 MCD spectra of (a)37

Figure 3.6 (a) Integrated intensity of both negative and positive bands for direct

transitions in $\text{Cs}_3\text{Bi}_2\text{Cl}_9$ NCs; (b) Integrated intensity of both negative and positive bands for indirect transitions in $\text{Cs}_3\text{Bi}_2\text{Cl}_9$ NCs; (c) Integrated intensity of both negative and positive bands for direct transitions in $\text{Cs}_3\text{Bi}_2\text{Br}_9$ NCs; (d) Integrated intensity of both negative and positive bands for indirect transitions in $\text{Cs}_3\text{Bi}_2\text{Br}_9$ NCs. 39

Figure 4.1 PXRD patterns of $\text{Cs}_2\text{AgBiX}_6$ NCs compared to reference patterns of $\text{Cs}_2\text{AgBiCl}_6$ (ICSD Coll. Code 291598) and $\text{Cs}_2\text{AgBiBr}_6$ 41

Figure 4.2 TEM characterization of (a) $\text{Cs}_2\text{AgBiCl}_6$ and (b) $\text{Cs}_2\text{AgBiBr}_6$ NCs. Size distribution diagram for (c) $\text{Cs}_2\text{AgBiCl}_6$ and (d) $\text{Cs}_2\text{AgBiBr}_6$ NCs determined from TEM image. The average NCs sizes and standard deviations are shown in the corresponding graphs. 42

Figure 4.3 Absorption spectra of (a) $\text{Cs}_2\text{AgBiCl}_6$ and (b) $\text{Cs}_2\text{AgBiBr}_6$ NCs collected at 5 K. 43

Figure 4.4 MCD spectra of (a) $\text{Cs}_2\text{AgBiCl}_6$ and (b) $\text{Cs}_2\text{AgBiBr}_6$ NCs collected at 5 K and different external magnetic field strengths (1-7 T), as indicated in the graph. 45

Figure 4.5 Optical absorption (top) and MCD (bottom) spectra of (a) $\text{Cs}_2\text{AgBiCl}_6$ and (b) $\text{Cs}_2\text{AgBiBr}_6$ NCs in the band gap region, collected at 7 T and 5 K. (Legend: black line - normalized MCD data; pink line - cumulative peak; blue line - simulated direct transition; green line - simulated bound exciton transition) 46

Figure 4.6 (a) Integrated intensity of both negative and positive bands for direct transitions in $\text{Cs}_2\text{AgBiCl}_6$ NCs; (b) Integrated intensity of both negative and positive bands for bound exciton transitions in $\text{Cs}_2\text{AgBiCl}_6$ NCs; (c) Integrated intensity of both

negative and positive bands for direct transitions in $\text{Cs}_2\text{AgBiBr}_6$ NCs; (d) Integrated intensity of both negative and positive bands for bound exciton transitions in $\text{Cs}_2\text{AgBiBr}_6$ NCs.....	46
Figure 4.7 Normalized 7 T field MCD spectra of (a) $\text{Cs}_2\text{AgBiCl}_6$ and (b) $\text{Cs}_2\text{AgBiBr}_6$ NCs at temperatures ranging from 5 K to 300 K.....	48
Figure 4.8 Relative change of $\Delta A/A$ for $\text{Cs}_2\text{AgBiCl}_6$ and $\text{Cs}_2\text{AgBiBr}_6$ NCs at various temperatures compared to 5 K.....	49
Figure 4.9 (a) PXRD patterns of $\text{Cs}_2\text{AgInCl}_6$ NCs compared to reference patterns of $\text{Cs}_2\text{AgInCl}_6$ (cubic, ICSD Coll. Code #11524).....	51
Figure 4.10 (a) TEM image of $\text{Cs}_2\text{AgInCl}_6$ NCs (b) Size distribution diagram of $\text{Cs}_2\text{AgInCl}_6$. The average NCs sizes and standard deviations are shown in the graph. ...	51
Figure 4.11 Optical absorption spectrum of $\text{Cs}_2\text{AgInCl}_6$ NCs (top) and MCD spectra of $\text{Cs}_2\text{AgInCl}_6$ NCs at different magnetic fields (bottom).....	52
Figure 4.12 Maximum peak intensity of $\text{Cs}_2\text{AgInCl}_6$ from 1 T to 7 T with best- fit linear line.....	53
Figure 4.13 Variable temperature MCD spectra of $\text{Cs}_2\text{AgInCl}_6$ NCs.....	54
Figure 4.14 PXRD patterns of $\text{Cs}_2\text{AgBi}_{0.5}\text{In}_{0.5}\text{Cl}_6$ NCs compared to the PXRD pattern of $\text{Cs}_2\text{AgInCl}_6$ and reference patterns of $\text{Cs}_2\text{AgBi}_{0.5}\text{In}_{0.5}\text{Cl}_6$ (cubic, ICSD Coll. Code #11524).....	55
Figure 4.15 (a) TEM image of $\text{Cs}_2\text{AgBi}_{0.5}\text{In}_{0.5}\text{Cl}_6$ NCs (b) Size distribution diagram of $\text{Cs}_2\text{AgBi}_{0.5}\text{In}_{0.5}\text{Cl}_6$ NCs. The average NCs sizes and standard deviations are shown in the	

graph.....	56
Figure 4.16 Optical absorption spectrum of $\text{Cs}_2\text{AgBi}_{0.5}\text{In}_{0.5}\text{Cl}_6$ NCs (top) and MCD spectra of $\text{Cs}_2\text{AgBi}_{0.5}\text{In}_{0.5}\text{Cl}_6$ NCs at different magnetic fields (bottom).....	57
Figure 4.17 Peak intensity of direct band gap transition and bound exciton transition of $\text{Cs}_2\text{AgBi}_{0.5}\text{In}_{0.5}\text{Cl}_6$ NCs from 1 T to 7 T.....	58
Figure 4.18 (a) Normalized 7 T field MCD spectra of $\text{Cs}_2\text{AgBi}_{0.5}\text{In}_{0.5}\text{Cl}_6$ NCs at temperatures ranging from 5 K to 300 K. (b) Relative change of normalized MCD signal at different temperature compared with the signal at 5 K.....	59
Figure A.1. MCD spectra of $\text{Cs}_3\text{Bi}_2\text{Cl}_9$ collected at (a) 5 K (b) 20 K (c) 50 K (d) 100 K (e) 200 K (f) 300 K. (Legend: black line - normalized MCD data; pink line - cumulative peak; green line - simulated direct transition; purple line - simulated indirect transition; orange line - Bismuth s-p transition).....	84
Figure A.2. MCD spectra of $\text{Cs}_3\text{Bi}_2\text{Br}_9$ collected at (a) 5 K (b) 20 K (c) 50 K (d) 100 K (e) 200 K (f) 300 K. (Legend: black line - normalized MCD data; pink line - cumulative peak; green line - simulated direct transition; purple line - simulated indirect transition; orange line - Bismuth s-p transition).....	85
Figure B.1. MCD spectra of $\text{Cs}_2\text{AgBiCl}_6$ collected at (a) 5 K-7 T (b) 5 K-6 T (c) 5 K-5 T (d) 5 K-4 T (e) 5 K-3 T (f) 5 K-2 T (g) 5 K-1 T. (Legend: black line - normalized MCD data; pink line - cumulative peak; blue line - simulated direct transition; green line - simulated bound exciton transition).....	86
Figure B.2. MCD spectra of $\text{Cs}_2\text{AgBiCl}_6$ collected at (a) 5 K (b) 10 K (c) 20 K (d) 50 K (e)	

100 K (f) 200 K (g) 300 K. (Legend: black line - normalized MCD data; pink line - cumulative peak; blue line - simulated direct transition; green line - simulated bound exciton transition).....87

Figure B.3. MCD spectra of $\text{Cs}_2\text{AgBiBr}_6$ collected at (a) 5 K-7 T (b) 5 K-6 T (c) 5 K-5 T (d) 5 K-4 T (e) 5 K-3 T (f) 5 K-2 T (g) 5 K-1 T. (Legend: black line - normalized MCD data; pink line - cumulative peak; blue line - simulated direct transition; green line - simulated bound exciton transition).....88

Figure B.4. MCD spectra of $\text{Cs}_2\text{AgBiBr}_6$ collected at (a) 5 K (b) 10 K (c) 20 K (d) 50 K (e) 100 K (f) 200 K (g) 300 K. (Legend: black line - normalized MCD data; pink line - cumulative peak; blue line - simulated direct transition; green line - simulated bound exciton transition).....89

Figure B.5. MCD spectra of $\text{Cs}_2\text{AgIn}_{0.5}\text{Bi}_{0.5}\text{Cl}_6$ collected at (a) 5 K-7 T (b) 5 K-6 T (c) 5 K-5 T (d) 5 K-4 T (e) 5 K-3 T (f) 5 K-2 T (g) 5 K-1 T. (Legend: black line - MCD data; pink line - cumulative peak; blue line - simulated direct transition; green line - simulated bound exciton transition)..... 90

Figure B.6. MCD spectra of $\text{Cs}_2\text{AgIn}_{0.5}\text{Bi}_{0.5}\text{Cl}_6$ collected at (a) 5 K (b) 10 K (c) 20 K (d) 50 K (e) 100 K (f) 200 K (g) 300 K. (Legend: black line - normalized MCD data; pink line - cumulative peak; blue line - simulated direct transition; green line - simulated bound exciton transition)..... 91

List of Abbreviations

NCs	Nanocrystals
VBM	Valence Band Maximum
CBM	Conduction Band Minimum
LO phonon	Longitudinal Optical Phonon
ac phonon	acoustic phonons
PL	Photoluminescence
PLQY	Photoluminescence Quantum Yields
MHPs	Metal Halide Perovskites
LEDs	Light-emitting Diodes
HDPs	Halide Double Perovskites
DFT	Density functional theory
FETs	Field-effect Transistors
STEs	Self-trapped Excitons
SOC	Spin-Orbit Coupling
GMR	Giant Magnetoresistance
MRAM	Magnetoresistive Random-Access Memory
MCD	Magnetic Circular Dichroism
LCP	Left Circularly Polarized
RCP	Right Circularly Polarized
PXRD	Powder X-ray Diffraction

ICSD	Inorganic Crystal Structure Database
TEM	Transmission Electron Microscopy
UV-Vis	Ultraviolet-Visible- Spectroscopy
ODE	1-Octadecene
Oleylamine	Olam
Oleic Acid	OA
TMS-Cl/Br	Trimethylsilyl chloride/bromide,
Diphenyl Ether	DPE
DMSs	Dilute Magnetic Semiconductors

Chapter 1.

Introduction

1.1 Background

1.1.1 Semiconductor Nanocrystals

Semiconductor nanocrystals (NCs) are small crystalline particles whose optical and electronic properties are size-dependent.^[1] These nanocrystals typically have dimensions ranging from 1 to 100 nm, exhibiting discrete electronic transitions similar to those of isolated atoms and molecules. This unique behavior facilitates the utilization of the superior properties of semiconductor materials.^[2] Semiconductor materials can be classified into two main types: intrinsic and extrinsic semiconductors. The conductivity of an intrinsic semiconductor, such as silicon (Si) and germanium (Ge), is primarily temperature-dependent and is usually low at room temperature.^[3] Introducing impurities into a pure semiconductor increases its conductivity, resulting in an extrinsic semiconductor. Extrinsic semiconductors are further divided into n-type and p-type, based on the type of charge carriers introduced by the impurities. In n-type semiconductors, donor impurities provide additional electrons to the conduction band. The donor level E_D is slightly below the conduction band edge E_C , allowing electrons to be promoted to the conduction band with minimal energy. The total number of conduction-band electrons n_e is comprised of both donor and intrinsic electrons, while the total number of holes n_h comes from intrinsic sources, making electrons the majority

carriers and holes the minority carriers. Conversely, in p-type semiconductors, acceptor impurities create additional holes. The acceptor level E_A is slightly above the valence band maximum (VBM), allowing electrons from the valence band to transition to E_A with small energy, ionizing the acceptor negatively. In this material, holes are the majority carriers, and electrons are the minority carriers.^{[3][4]}

1.1.2 Absorption

In an ideal semiconductor at absolute zero temperature, the valence band is completely filled with electrons. When photons with sufficient energy are absorbed, they excite electrons, causing them to transition across the band gap into the unoccupied conduction band, thereby leaving holes in the valence band and creating electron-hole pairs. This process, wherein electron transitions occur between the bands due to photon absorption, is referred to as absorption. In the process of absorption, both energy and momentum conservation must be satisfied. Therefore, this band-to-band transition can be classified into direct and indirect transitions, as illustrated in Figure 1.1 In an indirect transition process, electrons not only absorb photons but also exchange vibrational energy with the lattice, either by emitting or absorbing a phonon.^[5]

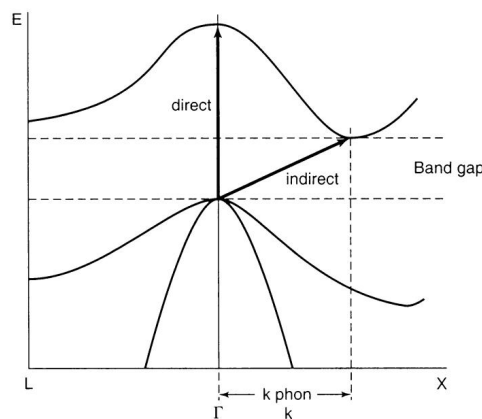


Figure 1.1 Schematic diagram of direct versus indirect interband absorptions in Si. Reproduced from Ref. [5]

In addition, the electronic transitions between bands in semiconductors are subject to selection rules that determine whether a transition is allowed or forbidden. In molecular systems, these rules stipulate that the total spin number must remain unchanged during the transition ($\Delta S=0$), while the total orbital angular momentum may change by $\Delta L=0, \pm 1$, with the exception of transitions where $L=0$ in both states.^{[6][7]} Additionally, the orbital selection rule requires that transitions occur only between states of opposite parity (i.e., one state must be even, and the other odd).^{[6][7]} In UV-vis spectroscopy, "allowed" transitions result in much more intense absorption bands compared to "forbidden" transitions.^[6]

1.1.3 Excitons

As previously mentioned, during the absorption process, electrons are excited from the fully occupied valence band to the unoccupied in the conduction band, resulting in the creation of holes in the valence band. Due to their opposite charges, a Coulomb attraction arises between the electrons and holes, forming a hydrogen-like bound state known as an exciton.^[8] Excitons are typically classified into two categories as shown in Figure 1.2: Wannier excitons and Frenkel excitons. Wannier excitons can extend over many atomic sites in the crystal, while Frenkel excitons are typically localized.^[9] The lowest energy level of an exciton is above the ground state energy of the crystal, and the energy difference is $E_g - E_b$, which is slightly less than the band gap energy E_g . Here, E_b represents the exciton binding energy, which is the energy required to dissociate an exciton into its constituent electron and hole charge carriers. A higher exciton binding energy indicates a

more stable exciton with a longer lifetime.^[9] Frenkel excitons are generally considered more stable due to their higher binding energy, while Wannier excitons, with their lower binding energy, are less stable and tend to dissociate easily at room temperature.^[10] Typically, when $k_B T > E_b$, (where k_B is the Boltzmann constant), most excitons dissociate, allowing free electrons and holes to become the dominant charge carriers.

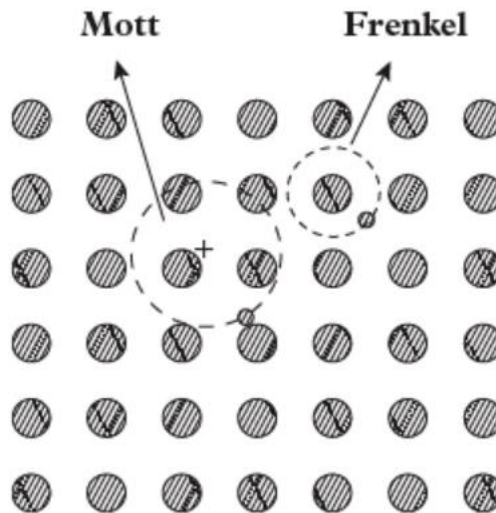


Figure 1.2 Schematic of Wannier excitons (Mott) and Frenkel excitons. Reproduced from Ref. [9]

1.1.4 Phonon

The phonon describes the particle nature of an oscillator. Phonon waves are elastic waves, vibrating in a longitudinal and/or in a transversal mode.^[11] Phonons can be categorized into optical and acoustic phonons, which are separated by a frequency gap. The lower branch, known as the acoustic phonon, reaches its minimum frequency as the wave vector k approaches zero, and its maximum frequency at the boundary of the Brillouin zone. Conversely, the upper branch, called the optical phonon, has its highest frequency at the center of the Brillouin zone, with the frequency gradually decreasing towards the boundary of the zone.^[12] It is worth noting that phonons are

temperature-dependent; as the temperature increases, phonons become more active, while their activity decreases with lowering temperatures. Additionally, phonons participate in optical processes by interacting with electrons or excitons, which is known as electron-phonon coupling or exciton-phonon coupling. The Fröhlich mechanism is the most common type of exciton-phonon interaction. Due to the oscillation of oppositely charged ions moving in the opposite directions, long-wavelength longitudinal optical (LO) phonons induce a long-range macroscopic electric field in the vibrating lattice along the wave vector k direction. This electric field, or the equivalent macroscopic crystal polarization, then interacts via Coulomb forces with charge carriers or excitons.^[12]

1.1.5 Recombination and luminescence

Emission is the process opposite to absorption. As previously mentioned, photoexcitation generates electrons and holes. The relaxation of an excited electron back to the valence band results in the annihilation of the exciton and may be accompanied by the emission of a photon (luminescence). The relaxation of excited electrons back to the valence band can result in exciton annihilation, potentially accompanied by photon emission, a process known as luminescence or radiative recombination.^[13] However, not all excited-state energy returns to the ground state through radiative recombination. The process in which excited-state energy is converted into other forms of energy as it relaxes to the ground state is known as non-radiative recombination. Luminescent properties are fundamental to many applications.^{[14][15][16]} Perovskite, as a popular photoluminescent material in recent years, have garnered significant attention due to their excellent properties and substantial potential for applications in various technologies.^{[17][18]}

1.2 Lead Halide Perovskites Semiconductor

Perovskites are a class of materials defined by the stoichiometry ABX_3 , possessing a crystal structure analogous to that of $CaTiO_3$, which was first identified by Gustav Rose in 1839.^[19] For metal halide perovskites (MHPs), the A-site is occupied by a monovalent cation, which can be either organic or inorganic. The most common organic cations are methylammonium $[(CH_3NH_3)^+, MA^+]$ and formamidinium $[(HC(NH_2)_2)^+, FA^+]$, while the most prevalent inorganic cation is cesium (Cs^+). The B-site is typically occupied by a divalent metal cation, most commonly lead (Pb^{2+}), and the X-site is occupied by a halide anion (I^- , Br^- , or Cl^-).^[20] The three-dimensional (3D) structure of MHPs comprises corner-sharing $[PbX_6]^{4-}$ octahedra, with A^+ cations occupying the voids formed by four adjacent $[PbX_6]^{4-}$ octahedra, as shown in Figure 1.3.^[21]

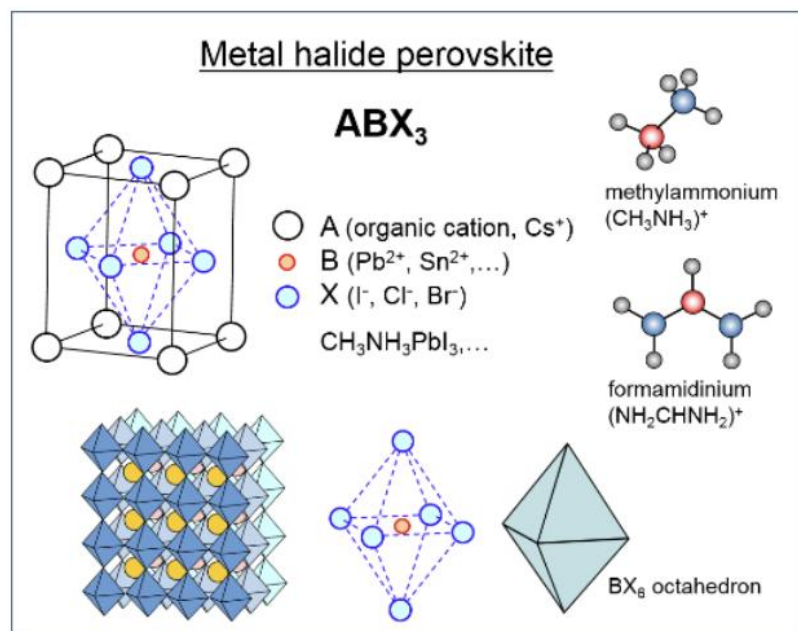


Figure 1.3 Schematic diagram for Metal halide perovskite ABX_3 . Reproduced from Ref. [21]

Goldschmidt's tolerance factor (t) (Equation 1) and the octahedral factor (μ) (Equation 2) are two significant factors used to assess the structural stability of MHPs. r_A ,

r_B , and r_X are the ionic radii of the A-cation, B-cation, and X-anion, respectively. These factors help determine the compatibility of specific ions within the crystal structure, thereby providing insight into the overall stability and potential formation of the perovskite phase.^[22] A tolerance factor (t) between 0.9 and 1.0 favors the formation of an ideal cubic structure, while an octahedral factor (μ) between 0.4 and 0.9 will lead to the formation of BX_6 octahedra.^[23] The 3D cubic phase is characteristic of the high-temperature phase of MHPs. At lower temperatures, phase transitions will occur, resulting in structures such as tetragonal, orthorhombic, trigonal, or hexagonal phases.^{[24][25]}

$$t = \frac{r_A + r_X}{\sqrt{2}(r_B + r_X)} \quad (1)$$

$$\mu = \frac{r_B}{r_X} \quad (2)$$

MHPs are widely recognized as promising photosensitive semiconductors.^{[24][26][27][28]} In the past decade, these materials have found applications in various optoelectronic devices, including X-ray scintillators,^[29] light-emitting diodes (LEDs),^[30] photodetectors,^[31] and lasers.^[32] Among MHPs, all-inorganic cesium lead halide perovskite ($CsPbX_3$; X=Cl, Br, and I) NCs have received particular attention due to their remarkable properties and potentially higher stability. For instance, colloidal $CsPbX_3$ NCs exhibit a widely tunable band gap energy across the entire visible light spectrum by adjusting the halide composition and particle size.^[33] Additionally their photoluminescence quantum yields (PLQY) can range from 50% to 90%.^[25] They also have been reported to possess a high absorption coefficient,^[34] high carrier mobility ($\sim 4500 \text{ cm}^2 \text{ V}^{-1} \text{ s}^{-1}$) and large diffusion lengths ($> 9.2 \text{ } \mu\text{m}$).^[35] Moreover, a strong spin-orbit

coupling effect has been observed in lead halide perovskite NCs, greatly enhancing their potential for applications involving optical control and manipulation.^[36] However, the instability and toxicity of lead-based perovskites significantly limit their further development.^{[37][38]} Thus, the development of stable and low-toxicity perovskite nanomaterials has increasingly garnered interest within the scientific community.

1.3 Lead-free perovskite materials

The ideal scenario would be to replace lead (Pb) in halide perovskites with non-toxic elements without compromising performance. The material's structure and electronic configuration are critical factors in determining its optoelectronic properties. Therefore, various feasible lead substitutes have been selected based on considerations of element size, charge, properties, electronic structure, and structural tolerance.^[39] As shown in Figure 1.4, current substitution strategies can generally be categorized as homovalent substitution (e.g., using Sn^{2+} or Ge^{2+}),^{[40][41]} and heterovalent substitution, typically involving Bi^{3+} .^[42] The latter has received more attention due to the chemical stability and electronic structure of Bi^{3+} that closely resembles that of Pb^{2+} .^[43] To maintain charge neutrality, heterovalent replacements further can be categorized into three subtypes: cation splitting, mixed valence anions, and ordered vacancies.^[44] In the following part of this chapter, we will primarily focus on bismuth-substituted perovskite-like materials, such as $\text{Cs}_3\text{Bi}_2\text{X}_9$, as well as double perovskite containing one monovalent and one trivalent element substitution.

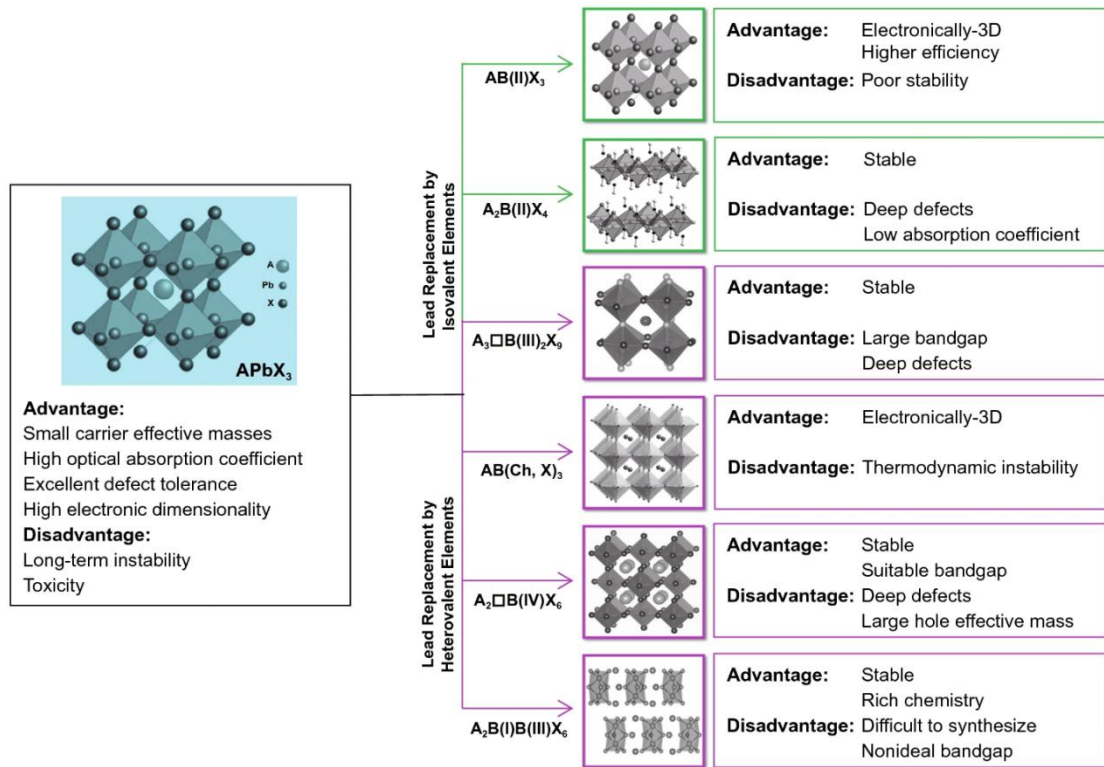


Figure 1.4 Schematic diagram of different substitution methods and consequences.

Reproduced from Ref. [44]

1.3.1 Cesium Bismuth Halide NCs Cs₃Bi₂X₉

Cs₃Bi₂X₉ (shown in 1.5) exhibits a trigonal crystal lattice (space group $P\bar{3}m1$) at room temperature, considered a layered form of vacancy-ordered perovskite. This structure can be seen as a tripled unit cell of the traditional perovskite, in which only two-thirds of the octahedral sites (e.g., Pb²⁺ sites in prototypical CsPbX₃) are occupied, while the remaining sites are vacant.^[45] These vacancies are segregated, leading to the formation of corrugated layers composed of corner-sharing BiBr₆ octahedra.^[45] Additionally, a monoclinic phase which exhibits similar framework has also been reported at low temperatures.^{[46][47]}

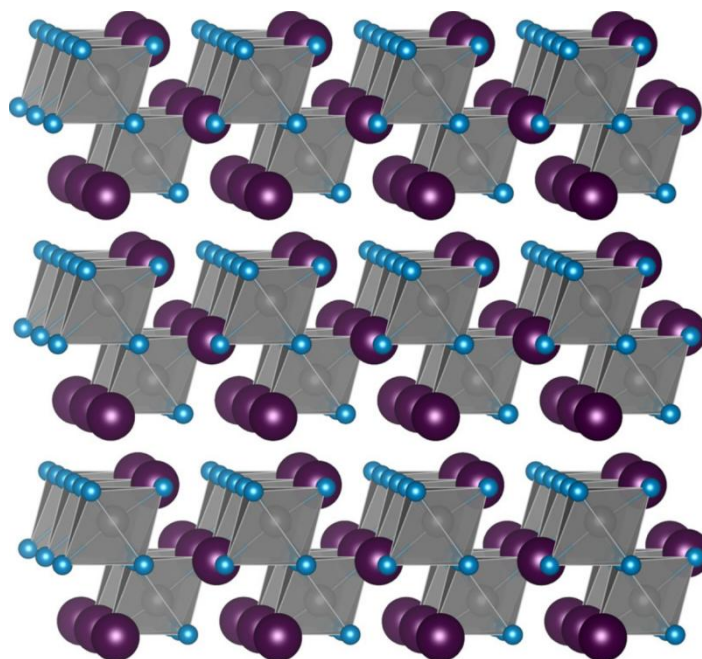


Figure 1.5 Schematic diagram of crystal structure of $\text{Cs}_3\text{Bi}_2\text{X}_9$ at room temperature. Gray atoms represent Bi, blue atoms represent halide ion, and purple atoms represent Cs. Reproduced from Ref. [27]

Previous density functional theory (DFT) calculation revealed that the VBM of $\text{Cs}_3\text{Bi}_2\text{X}_9$ is primarily comprised of halide-p and Bi-6s orbitals, while the conduction band minimum (CBM) is predominantly composed of Bi-6p orbitals, with negligible contribution from Cs^+ .^[48] This band gap composition is similar to that of lead-based perovskites, where the valence band is formed by the mixing of halide p orbitals and Pb-6s orbitals, and the conduction band is composed of mixed Pb-6p and halide p orbitals.^[49] Such a similar electronic structure makes it a promising candidate for perovskite-like materials. Although its optoelectronic properties are not as good as those of lead-based counterparts, its PLQY has increased from 4.5% to 19.4% in the past few years.^{[50][51]} Additionally, the close proximity of its indirect and direct bandgaps offers significant potential for converting it into a direct bandgap material, which could further improve the PLQY.^[52] Moreover, $\text{Cs}_3\text{Bi}_2\text{X}_9$ NCs demonstrate excellent moisture stability,

thermal stability, and photostability, which makes it highly promising for applications in the field of LEDs.^{[50][51]} Furthermore, Cs₃Bi₂X₉ exhibits satisfactory performance in photocatalysis.^{[53][54][55]} The rapid electrical response of Cs₃Bi₂X₉ indicates significant potential for use in photodetector devices.^{[56][57]} In addition, Mn²⁺-doped Cs₃Bi₂Cl₉ NCs exhibit a bright orange emission resulting from the Mn²⁺ d-d transition, expanding the intrinsic photoluminescence properties of the NC host lattice.^[58] Er³⁺-doped Cs₃Bi₂Cl₉ phosphor shows efficient temperature-sensitive upconversion luminescence for different excitation sources.^[59] These properties make it a promising candidate material for multi-mode luminescence and optical thermometer applications.

1.3.2 Halide Double Perovskites (HDPs)

Halide double perovskites are a class of materials derived from the traditional perovskite structure. These materials are represented by the formula Cs₂B(i)B'(iii)X₆, where the 'B' site is occupied by two different cations: a monovalent ion B(i) and a trivalent metal ion B'(iii) (Figure 1.6). HDPs are obtained by substituting adjacent divalent Pb²⁺ ions with one monovalent and one trivalent metal cation. This ordered arrangement maintains the overall charge balance within the structure and doubles the unit cell of the traditional perovskite structure.^[60] The tolerance factor and octahedral factor of double perovskite are typically considered similar to those of lead halide perovskites, but the average value of B (i) and B' (iii) is taken as the atomic radius R_B for the B-site.^[60] In addition, Bartel et al.^[61] reported a new tolerance factor (τ') (Equation 3). This is an empirical function that takes into account the oxidation states of the ions.

$$t' = \frac{r_X}{r_B} - n_A \left(n_A - \frac{r_A/r_X}{\ln(r_A+r_B)} \right) \quad (3)$$

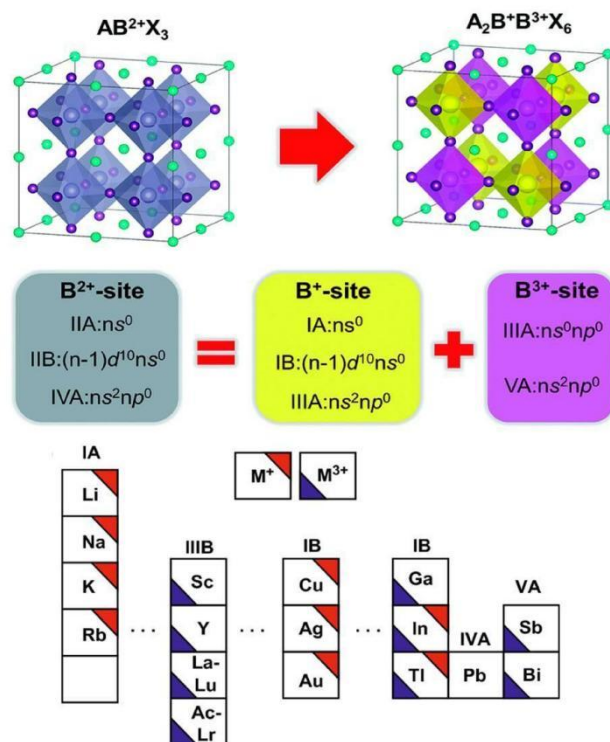


Figure 1.6 Schematic diagram of crystal structure of DPs and potential substitutions approaches. Reproduced from Ref.[60]

Double perovskites have been widely studied because of their compositional diversity and superior stability.^[62] Additionally, a variety of compositions enabled by cation substitution facilitates the control and modulation of their optical and electronic properties, making them promising candidates for diverse optoelectronic applications.^{[18][63][64]} Among the various HDPs, B-site substitutions with AgBi and AgIn have received the most attention due to Cs_2AgBiX_6 having a relatively small bandgap, while Cs_2AgInX_6 is notable for its direct bandgap characteristics.

1.3.2.1 Cerium silver bismuth halide NCs Cs_2AgBiX_6 (X=Cl and Br)

Cs_2AgBiX_6 is generally considered an indirect band gap semiconductor. DFT calculations have predicted that the band gap energies for $Cs_2AgBiCl_6$ and $Cs_2AgBiBr_6$

are 1.84 eV and 1.41 eV, respectively.^[65] The VBM is mainly composed of Ag-d and halogen-p orbitals in both compounds, while the CBM is comprised of Bi-p and halogen-p states, with some contribution from Ag-s orbitals.^[66] Additionally, by altering the halide composition in $\text{Cs}_2\text{AgBi}(\text{Cl}_{1-x}\text{Br}_x)_6$ ($0 \leq x \leq 1$) NCs, excitonic absorption peaks can be continuously tuned from 367 to 450 nm, and the corresponding photoluminescence (PL) peaks from 395 to 475 nm.^[67]

Additionally, $\text{Cs}_2\text{AgBiBr}_6$ has been reported to exhibit strong electron-phonon coupling. The PL emission in $\text{Cs}_2\text{AgBiBr}_6$ has been demonstrated to be associated with color centers and is influenced by strong electron-phonon coupling.^[68] Steele et al.^[69] reported a Frohlich coupling constant close to 230 meV and a relatively large Huang – Rhys factor ($S = 15.4$). Electron-phonon coupling is a significant factor influencing carrier transport. The relatively low carrier mobility observed in $\text{Cs}_2\text{AgBiX}_6$ materials is a key limitation that hampers their performance in optoelectronic applications. However, it has been reported that hydrogenated $\text{Cs}_2\text{AgBiBr}_6$ can effectively increase both the concentration and mobility of charge carriers.^[70] Moreover, McClure et al.^[71] reported the effective charge carrier masses for both lead-based perovskites and $\text{Cs}_2\text{AgBiX}_6$ double perovskites. They found that although double perovskites have a less dispersed conduction band, the estimated hole effective masses for the double perovskites are smaller than those of their lead analogs. This characteristic introduces new possibilities for further enhancing charge carrier mobility in perovskite materials. In addition, there has been a growing interest in exploring the application of $\text{Cs}_2\text{AgBiBr}_6$ in field-effect transistors (FETs).^[72] Furthermore, $\text{Cs}_2\text{AgBiX}_6$ demonstrates exceptional stability under

conditions of light,^[73] heat,^[74] and humidity,^[70] making it a promising material for applications in various fields such as photovoltaics,^[71] photocatalysis,^[75] photodetectors,^[76] and other optoelectronic devices.^[77]

1.3.2.2 Cerium silver indium chloride NCs $\text{Cs}_2\text{AgInCl}_6$

$\text{Cs}_2\text{AgInCl}_6$ is another noteworthy double perovskite material, distinguished by its direct bandgap, which contributes to its superior PL properties compared to Bi-based double perovskites. However, $\text{Cs}_2\text{AgInCl}_6$ exhibits a relatively wide bandgap of approximately 3.33 eV, due to the parity-forbidden nature of the direct transition at the Γ point between the CBM and the VBM.^[78] DFT calculations have revealed that the VBM is primarily composed of Ag 4d and Cl 3p orbitals, while the CBM is mainly derived from In 5s orbitals.^[79] As shown in the Figure 1,7, transitions from the VBM (Γ_3^+) and the the next lower valence band state (Γ_4^+) to the CBM (Γ_1^+) are parity-forbidden, while parity-allowed transitions occur from the second lower valence band state (Γ_4^-) to the CBM (Γ_1^+).^[78] Although the band-edge states at the Γ point have the same parity, the band-edge states at the adjacent L point have the opposite parity. This difference in parity enables optical transitions between the Γ and L points, which, in turn, leads to a small optical absorption coefficient near the fundamental band gap.^{[78][79]}

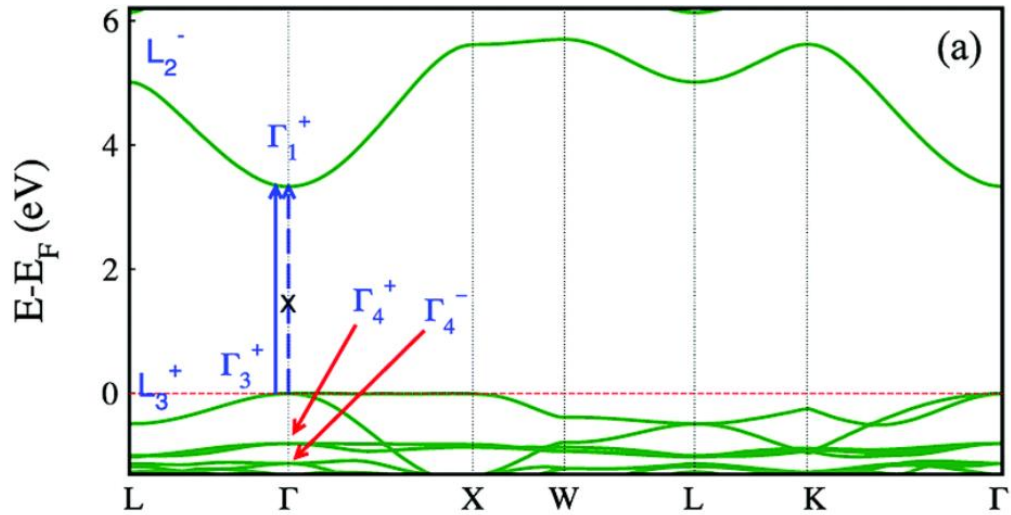


Figure 1.7 Electron band structure of $\text{Cs}_2\text{AgInCl}_6$ with parity of transitions. Reproduced from Ref. [78]

$\text{Cs}_2\text{AgInCl}_6$ exhibits excellent stability and shows promising potential for applications in ultraviolet photodetection.^[80] However, due to its dark transition caused by inversion symmetry, the reported PLQY of $\text{Cs}_2\text{AgInCl}_6$ is not ideal, being approximately 1.6%.^[81] The luminescence primarily originates from the emission of self-trapped excitons (STEs), with partial contributions from exciton radiative recombination.^[82] An effective way to break the parity symmetry is by doping or alloying with other elements. Liu et al.^[83] have demonstrated that partial substitution of Bi^{3+} for In^{3+} ions can break the parity-forbidden transitions and improve the emissions of self-trapped exciton (STE). Moreover, bismuth-doped $\text{Cs}_2\text{AgInCl}_6$ can introduce $[\text{BiCl}_6]^{3-}$ states below the original CBM, while keeping the direct bandgap.^{[84][85]} The PLQY of $\text{Cs}_2\text{AgInCl}_6$ co-doped with bismuth and sodium can reach up to 86%, making it a highly prospective material for LED devices.^{[82][86]}

1.4 Spintronics

Spintronics is an emerging field within nanoelectronics that studies the spin degree of freedom of charge carriers. It manipulates the spin and charge properties of electrons to enhance device performance, such as fast processing speeds, lower power consumption, and higher integration density.^[87] The interest in spintronics was sparked by the discovery of the giant magnetoresistance (GMR) effect a phenomenon where the electrical resistance of a material shows a significant change in response to an applied magnetic field.^[88] This effect arises from the alignment of magnetic moments in a thin film composed of alternating ferromagnetic and nonmagnetic layers. When the magnetic moments in the ferromagnetic layers are aligned parallel, the electrical resistance is low, and when they are antiparallel, the resistance is high.^[88] In the past few years, various GMR-based devices, such as magnetoresistive random-access memory (MRAM), have been widely used in industry and have continued to develop from generation to generation.^{[89][90]} Researchers also have begun exploring the generation and utilization of spin-polarized currents in bulk semiconductors and single semiconductor nanostructures,^{[91][92]} to realize the integration of conventional semiconductor technology with semiconductor-based spintronics devices.^{[93][94]}

Spin-orbit coupling (SOC) originates from the rotation of negatively charged electrons around a positively charged atomic nucleus. Electrons with orbital angular momentum generate a magnetic moment and an associated magnetic field, similar to a circulating current. Due to the electron's spin, it also possesses a magnetic moment. The interaction between the electron's spin magnetic moment and the magnetic field produced

by its orbital motion is referred to as spin-orbit coupling.^[95] The magnitude of SOC is influenced by the charge of the atomic nucleus, which is determined by the atomic number (Z). A larger nuclear charge results in a stronger current generated by the circulating electron. Consequently, the spin-orbit interaction is proportional to Z^4 .^[96] Due to large Z of lead, the SOC effect is particularly pronounced in lead-based perovskites. A strong spin-orbit coupling effects^[97] and magnetic exchange interactions^[98] have been observed in lead halide perovskite NCs, greatly enhancing their potential for applications involving optical and magnetic control and manipulation. Moreover, extensive research has been conducted on the coherent spin dynamics of charge carriers in lead-based perovskites.^{[99][100][101]} The Rashba SOC effect is a key feature in these materials, where structural inversion asymmetry leads to the splitting of spin energy levels, resulting in spin-polarized bands with significant momentum offsets.^[102] Extensive studies have reported large Rashba splitting and high spin polarization at room temperature in lead-based perovskites.^{[103][104]} This effect facilitates the generation of highly spin-polarized charge currents in chiral non-magnetic halide perovskites at room temperature, even in the absence of external magnetic fields.^[101] Additionally, Zhang et al^[105] discovered persistent spin helix states in two-dimensional halide perovskites, which have the potential to significantly increase spin lifetimes. Moreover, strong SOC in lead halide perovskite NCs induces a significant Autler-Townes effect, leading to enhanced exciton energy shifts and enabling efficient coherent optical manipulation across a wide range of wavelengths at room temperature.^[97] In addition, spin-orbit-coupled exciton-polariton condensates have been observed in lead perovskites, which hold

potential as quantum simulators for many-body spin-orbit coupling (SOC) processes.^[106] Therefore, in addition to traditional optical research, the strong SOC in lead halide perovskites makes them highly promising for spintronic applications. The ability to manipulate spin-polarized bands and control spin textures in these materials offers significant potential for the development of advanced spintronic devices, such as spin light-emitting diodes (spin-LEDs)^[107] and spin field-effect transistors (spin-FETs).^[108]

Bi^{3+} also has a high atomic number, with an electron configuration of $6s^26p^0$ similar to Pb^{2+} . Similarly it has been found to exhibit strong spin-orbit coupling.^[109] The conduction band of $\text{Cs}_2\text{AgBiX}_6$, primarily composed of Bi p orbitals, will split into two distinct bands due to strong SOC.^[109] However, more detailed information in terms of SOC effect remains limited.

1.6 Theoretical basis for Magnetic Circular Dichroism (MCD)

Magnetic circular dichroism (MCD) arises from the differences in absorption coefficients of left and right circularly polarized light when subjected to an applied magnetic field.^[110] Therefore, MCD is defined as the difference in absorption between left circularly polarized (LCP, A_{lcp}) and right circularly polarized (RCP, A_{rcp}) light under a longitudinal magnetic field, as expressed in Equation 3.

$$\Delta A = A_{\text{lcp}} - A_{\text{rcp}} \quad (3)$$

This differential absorption is caused by the Zeeman effect, which leads to the splitting of energy levels under the influence of the magnetic field, thereby changing the electronic absorption transitions. The intensity of MCD can be simplified as the sum of three

Faraday terms (A, B, and C terms), as represented by Equation 4

$$\Delta A = \gamma\mu_B B \left[A_1 \left(-\frac{df(E)}{dE} \right) + \left(B_0 + \frac{C_0}{k_B T} \right) f(E) \right] \quad (4)$$

where γ is a constant whose value depends on the chosen units. μ_B represents the Bohr magneton, B is the magnetic field, k_B stands for the Boltzmann constant, T is the temperature, E denotes energy, and $f(E)$ is the line-shape function. The parameters A_1 , B_0 , C_0 correspond to the A, B, and C terms of MCD, respectively. Each term represents the interaction between the ground or excited states and the external magnetic field, as shown in Figure 1.8^[111].

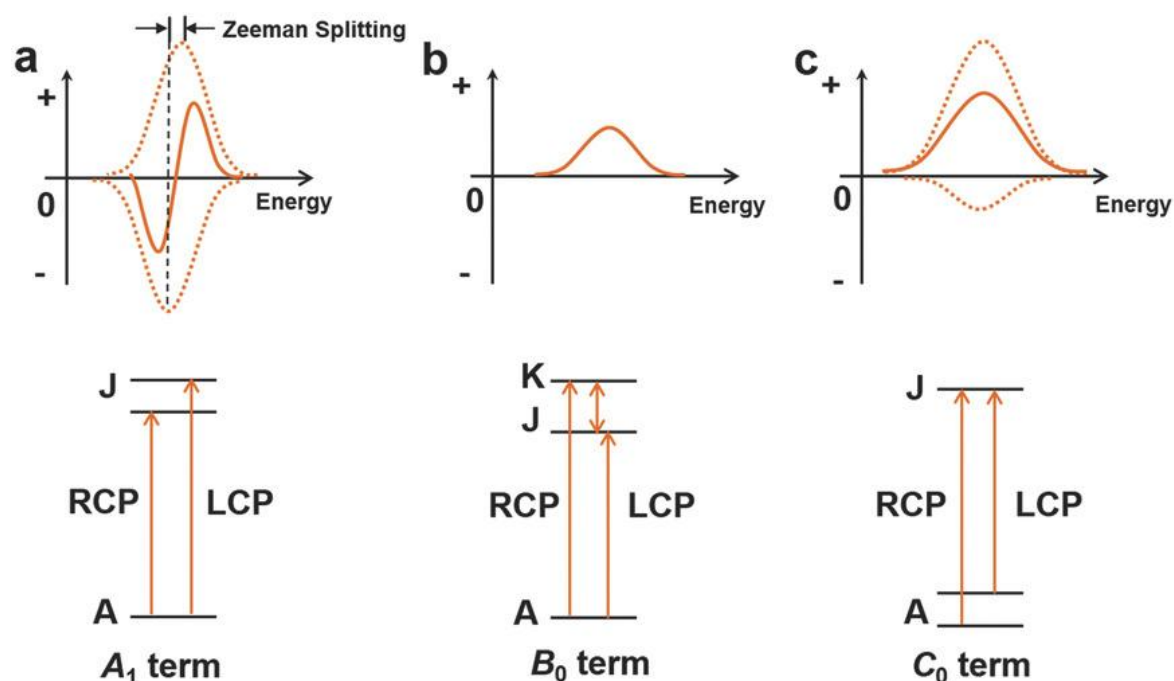


Figure 1.8 Mechanisms of a) A, b) B, and c) C terms in MCD. Dashed curves represent the absorption of LCP (positive) and RCP (negative) light. The solid lines represent the resultant MCD responses. Reproduced from Ref. [111]

The A term in MCD represents temperature-independent signals with a derivative line shape (Figure 1.8a). This term provides insight into the degeneracy of excited states. Under the influence of a magnetic field, degenerate excited states split into J_{-1} and J_{+1}

levels. According to selection rules, LCP light is absorbed, inducing transitions from the ground state to J_{+1} and RCP light induces transitions from the ground state to J_{-1} . The energy difference between A to J_{+1} and A to J_{-1} is the Zeeman splitting, and the corresponding Lande g -factor calculated.^[111] The B term is also temperature-independent and represents the interaction of the ground state and the excited state under an external magnetic field influenced by another state (K). Additionally, the C term is temperature-dependent and arises from the Zeeman splitting of the degenerate ground state population under an external magnetic field. The intensity of the C term is strongly affected by temperature due to the sensitivity of the field-split ground state population.^[111]

1.6 Motivations and Scope of the Thesis

The study of electronic structure is significant for semiconductors. A detailed study of the electronic structure provides deeper insights into the intrinsic properties of semiconductor materials, enabling the development of new materials with superior and more controllable performance.

Lead-based perovskites have shown tremendous promise in the fields of optoelectronics and photovoltaics, owing to their exceptional optical and electrical properties. However, the further large-scale commercialization of lead-based perovskites is consistently limited by concerns regarding toxicity and stability. Although additional encapsulation strategies can enhance their stability, the issue of lead leakage appears to remain unresolved.^[112] Replacing lead with other elements that have similar electronic structures but lower toxicity, such as bismuth, is an effective way to address the

aforementioned issues. Although the synthesis and applications of lead-free perovskites have been increasingly explored, their electronic properties, including the band structure origin, spin-orbit coupling, and intrinsic Zeeman effects, remain controversial, underexplored, or poorly understood. Understanding the electronic structure and properties of these lead-free perovskite materials can further improve their performance and expand their application range in fields such as spintronics and quantum technologies.

In this thesis, we focus on two types of lead-free perovskites: bismuth-substituted vacancy-ordered perovskite-like material $\text{Cs}_3\text{Bi}_2\text{X}_9$ ($\text{X} = \text{Cl}$ and Br) and double perovskites $\text{Cs}_2\text{B}(\text{i})\text{B}'(\text{iii})\text{X}_6$ ($\text{X} = \text{Cl}$ and Br). Chapter 2 provides a detailed description of the synthesis and characterization methods employed in this project, as well as the composition and analysis techniques for MCD. In Chapter 3, the electronic structure of $\text{Cs}_3\text{Bi}_2\text{X}_9$ is investigated, with a focus on the origins of the excitonic transitions and their Zeeman splitting. Additionally, the influence of halide elements on these properties is explored by varying the anion composition. In Chapter 4 we explored the electronic structure and magneto-optical properties of all-inorganic lead-free double halide perovskite NCs using MCD spectroscopy. We also investigated how variations in halide composition influence the electronic structure and excitonic Zeeman splitting in these double halide perovskite NCs by performing variable-temperature and variable-field MCD measurements on $\text{Cs}_2\text{AgBiCl}_6$ and $\text{Cs}_2\text{AgBiBr}_6$. Similarly, the influence of cation composition on these properties was explored by conducting comparative MCD measurement on $\text{Cs}_2\text{AgInCl}_6$ and Bi^{3+} -doped $\text{Cs}_2\text{AgInCl}_6$ NCs. In the final chapter, we

review and summarize the key findings of our research, while also introducing potential directions for future studies. The results of this work demonstrate that lead-free halide perovskite NCs are promising materials for quantum technologies (e.g., spintronics), which have a low toxicity and compositionally tunable electronic structure and properties.

In summary, given the critical need for sustainable, high-performance materials in the optoelectronic industry, this thesis is motivated by the potential of lead-free halide perovskite NCs to serve as viable alternatives to lead-based perovskites. By systematically investigating the electronic, magneto-optical, and excitonic properties of these materials, this research aims to contribute to the development of next-generation quantum devices that are both effective for electronic technology and environmentally friendly.

Chapter 2

Experimental Section

2.1 Material

All chemicals were used as received. Cesium carbonate [Cs_2CO_3 , 99.995%], Trimethylsilyl chloride (TMS-Cl, $\leq 100\%$), Trimethylsilyl bromide (TMS-Br, $\leq 100\%$), and Benzoyl chloride (Bz-Cl 99%) were purchased from Sigma-Aldrich. Bismuth(III) acetate [$\text{Bi}(\text{OAc})_3$, 99%] was purchased from thermo scientific. Silver acetate [$\text{Ag}(\text{OAc})$, 99%], diphenyl ether (DPE, 90%), oleic acid (OA, 90%), Oleylamine (Olam, 70%), and octadecene (1-ODE, technical grade 90%) were purchased from Fisher Chemical. Additionally, hexane (Fischer Chemical, $\geq 99.9\%$), isopropanol (Sigma-Aldrich, 99.8%), toluene (Alfa Aesar, 99.7%), ethyl acetate (thermo scientific, 99.5%) were utilized for washing the NCs and preparing dispersions for various characterization techniques.

2.2 Synthesis

2.2.1 $\text{Cs}_3\text{Bi}_2\text{X}_9$ Nanocrystal Synthesis

$\text{Cs}_3\text{Bi}_2\text{Cl}_9$ and $\text{Cs}_3\text{Bi}_2\text{Br}_9$ NCs were synthesized by a modified hot injection method^{[47][113]}. Briefly, cesium carbonate (0.125 mmol), bismuth acetate (0.5 mmol), 10 mL of 1-dodecanol, 0.6 mL of oleylamine (Olam), and 3 mL of oleic acid (OA) were combined in a 50 mL three-necked flask. The mixture was then degassed under vacuum at

100 °C for 1 hour with magnetic stirring. After that, the temperature of the mixture was increased to 160°C, and TMS-Cl/Br (trimethylsilyl chloride/bromide, 0.5 mL) was swiftly injected under a nitrogen atmosphere. After 30 seconds, the reaction mixture was rapidly cooled to room temperature by immersion in an ice-water bath. Subsequently, the solution was centrifuged at 3000 rpm for 3 minutes to remove larger particles. Ethyl acetate was then added to precipitate the nanocrystals, followed by centrifugation for 10 minutes. Afterward, the supernatant was decanted, and the NCs were resuspended in hexane. A brief centrifugation (30 seconds) was performed to remove any remaining insoluble material.

2.2.2 Cs₂AgBiX₆ Nanocrystal Synthesis

Cs₂AgBiX₆ was synthesized by a modified hot injection method^[114]. A mixture of Cs₂CO₃ (0.35 mmol), Ag(OAc) (0.5 mmol), and Bi(OAc)₃ (0.5 mmol) was dissolved in a solution containing octadecene (10 mL), oleic acid (2.5 g), and oleylamine (0.5 g). This reaction mixture was then heated to 90°C under vacuum conditions for 45 minutes. Subsequently, the temperature of the solution was increased to 140°C under a nitrogen atmosphere, and TMS-Cl/Br (2.7 mmol) was rapidly injected. After 30 seconds, the mixture was quickly cooled to room temperature using an ice-water bath. The resulting product was centrifuged at 3000 rpm for 3 minutes to remove large particles. The supernatant was then washed with isopropanol (IPA), and the NCs were subsequently resuspended in toluene.

2.2.3 Cs₂AgIn_{1-x}Bi_xCl₆ Nanocrystal Synthesis

Cs₂AgInX₆ was synthesized by a modified hot injection method^[115]. A mixture of Cs₂CO₃ (0.35 mmol), Ag(OAc) (0.5 mmol), In(OAc)₃ (0.5-x mmol) and Bi(OAc)₃ (x mmol) were dissolved in a solution containing diphenyl ether (10 mL), oleic acid (2.5 g), and oleylamine (1mL). This reaction mixture was then heated to 90°C under vacuum conditions for 45 minutes. Subsequently, the temperature of the solution was increased to 140°C under a nitrogen atmosphere, and Bz-Cl (2.5mmol) was rapidly injected. After 30 seconds, the mixture was quickly cooled to room temperature using an ice-water bath. The resulting product was centrifuged at 3000 rpm for 3 minutes to remove large particles. The supernatant was then washed with isopropanol (IPA), and the NCs were subsequently resuspended in hexane.

2.3 Measurement and Data Analysis

2.3.1 Powder X-ray Diffraction

Powder X-ray diffraction (PXRD) is an essential tool for identifying the structure of crystalline samples. XRD patterns for all sample were obtained using an INEL diffractometer, equipped with a position-sensitive detector and a monochromatic Cu K α radiation source ($\lambda = 1.5418 \text{ \AA}$), in Dr. Holger Kleinke's group in Department of Chemistry at the University of Waterloo. Samples are dropped on an aluminum sample holder. The baseline of all samples were processed with software Match!, and the reference patterns were obtained from Inorganic Crystal Structure Database (ICSD).

2.3.2 Transmission Electron Microscopy (TEM)

Transmission electron microscopy (TEM) images provide information on the size and morphology of the NCs. The TEM images were collected with a JEOL-2010F microscope operating at 200 kV. Samples were made by drop-casting diluted suspensions of NCs onto copper 300 mesh TEM grids.

2.3.3 UV-Vis-NIR Spectroscopy

UV-vis-NIR spectroscopy is employed to measure the absorption of materials within a certain range of wavelength. It provides information on the electronic structure of different transitions, including band edge and higher energy states. A Varian Cary 5000 UV-vis-NIR spectrophotometer was used to collect the absorption spectra of colloidal NCs. Colloidal solution was measured in a quartz cuvette.

2.3.4 Magnetic Circular Dichroism (MCD)

Magnetic Circular Dichroism (MCD) spectroscopy measures the differential absorption of left- and right-circularly polarized light. The experimental setup is illustrated in Figure 2.1.^[116]

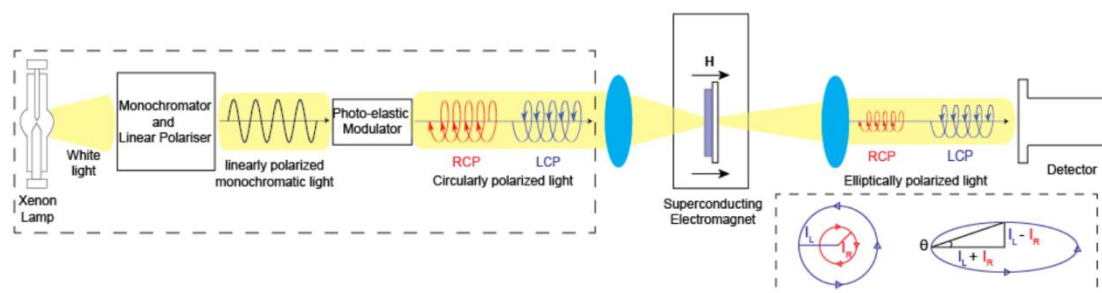


Figure 2.1 Schematic diagram of MCD Experimental Setup. In MCD spectroscopy,

light from a broadband source is directed through a monochromator and polarizer to produce a monochromatic, linearly polarized beam. This beam is then partially passed through a photoelastic modulator, generating left circularly polarized (LCP) and right circularly polarized (RCP) light. The sample is settled within a superconducting magneto-optical cryostat, with the magnetic field lines oriented parallel to the direction of light propagation. As the LCP and RCP light pass through the sample, they are absorbed to different degrees according to the absorption coefficients, resulting in different intensities. These differing intensities combine to form an elliptically polarized beam. The ellipticity (θ) is defined as the angle between the major and minor axes of the ellipse. Reproduced from ref. [116].

During the experiment, a JASCO J-815 spectropolarimeter was adopted to collect the difference in absorption of left and right circularly polarized light under a settled magnetic field which was parallel to the light propagation direction. Meanwhile, an Oxford SM 4000 magneto-optical cryostat was employed, providing a versatile sample environment with adjustable temperature ranging from 1.5 to 300 K and variable magnetic field strength up to 7 T. The samples were prepared by drop-casting colloidal NCs onto quartz substrates.

The MCD spectra were collected at various magnetic field strengths, ranging from 1 T to 7 T. To ensure accurate data analysis, all spectra were baseline-corrected by subtracting the spectrum collected at 0 T. As mentioned before, MCD intensity is defined as $\Delta A = A_L - A_R$ (Equation 3), and the ellipticity (θ) is then can be converted into $\Delta A/A$ by Equation 5,

$$\frac{\Delta A}{A_0} = \frac{\theta}{32982 * A} \quad (5)$$

where θ is measured in millidegrees, and A represents the band gap absorbance, which is determined from the absorption spectrum simultaneously collected by the CD detector.

In addition, the Zeeman splitting and corresponding Lande g-factor can be determined by Equation 6 and Equation 7,

$$\Delta E = \frac{\sqrt{2e}}{2} * \sigma * \frac{\Delta A}{A_0} \text{ [Equation 6]}$$

$$\Delta E = g_{ex}\mu_B B \text{ [equation 7]}$$

where 2σ represents the full width at $1/e$ of the maximum absorbance (A_0), μ_B is the Bohr magneton, and B denotes the magnetic field.

The deconvolution of MCD signals is a critical analytical method used in this thesis. Since the samples in this project are undoped or non-magnetically doped, they typically exhibit A-term MCD signals with a derivative line shape.^[117] As mentioned in Chapter 1.6, the A-term arises from the Zeeman splitting of the excited state, caused by the difference between transition of left- and right-circularly polarized light from the ground state to the split excited states. Therefore, we employed positive and negative Gaussian functions in Origin to fit the MCD signal, adjusting the peak widths and intensities of different transitions to achieve an optimal fit. Once the various transitions and their peak values are identified, we combined the positive and negative Gaussian functions corresponding to the same transitions to obtain the MCD peak profile of excitonic transitions. In this thesis, we perform deconvolution for both variable field and variable temperature MCD measurements. For the variable field MCD fitting, the peak width and position are kept constant while the peak intensity increases with the magnetic field. For the variable temperature MCD fitting, at low temperatures, the peak width and position remain unchanged, and the peak intensity is adjusted to achieve the best fit. At higher temperatures, due to changes in the bandgap and exciton energy levels, both the peak

position and intensity are appropriately adjusted to obtain the optimal fit.

Chapter 3 Magneto optical properties of Cs₃Bi₂Cl₉ and Cs₃Bi₂Br₉

3.1 Structural characterization of Cs₃Bi₂Cl₉ and Cs₃Bi₂Br₉ NCs

Cs₃Bi₂X₉ (X=Cl, Br) NCs were synthesized by a hot injection method, using a procedure similar to that previously reported (Chapter 2.2.1).^{[31][65]} Figure 3.1 shows powder X-ray diffraction (PXRD) data for Cs₃Bi₂Cl₉ and Cs₃Bi₂Br₉ NCs, together with the corresponding bulk reference patterns. Cs₃Bi₂Br₉ exhibits a trigonal crystal lattice (space group $P\bar{3}m1$) at room temperature, which represents a layered form of the vacancy-ordered perovskites (discussed in chapter 1.3.1). In addition, while some articles report one-dimensional *Pm**cn* crystal structure for Cs₃Bi₂Cl₉, based on the XRD pattern, the structure of our sample is consistent with the $P\bar{3}m1$, similar to Cs₃Bi₂Br₉.^[118] The results for Cs₃Bi₂Cl₉ and Cs₃Bi₂Br₉ NCs with identical structures have already been reported.^[119] As evident from Figure 3.1, all XRD peaks for Cs₃Bi₂Br₉ NCs are shifted to lower angles relative to those for Cs₃Bi₂Cl₉ NCs, which can be attributed to lattice expansion due to the larger ionic radius of Br⁻ than Cl⁻. The changes in the relative intensity of some peaks are likely due to lattice defects or NC variations in NC faceting. For instance, the peak associated with the (003) and (201) diffraction planes, exhibits a notable increase in intensity from Cs₃Bi₂Cl₉ to Cs₃Bi₂Br₉ NC samples.^[69] The assignments of various peaks for both samples also are provided in the Figure 3.1.

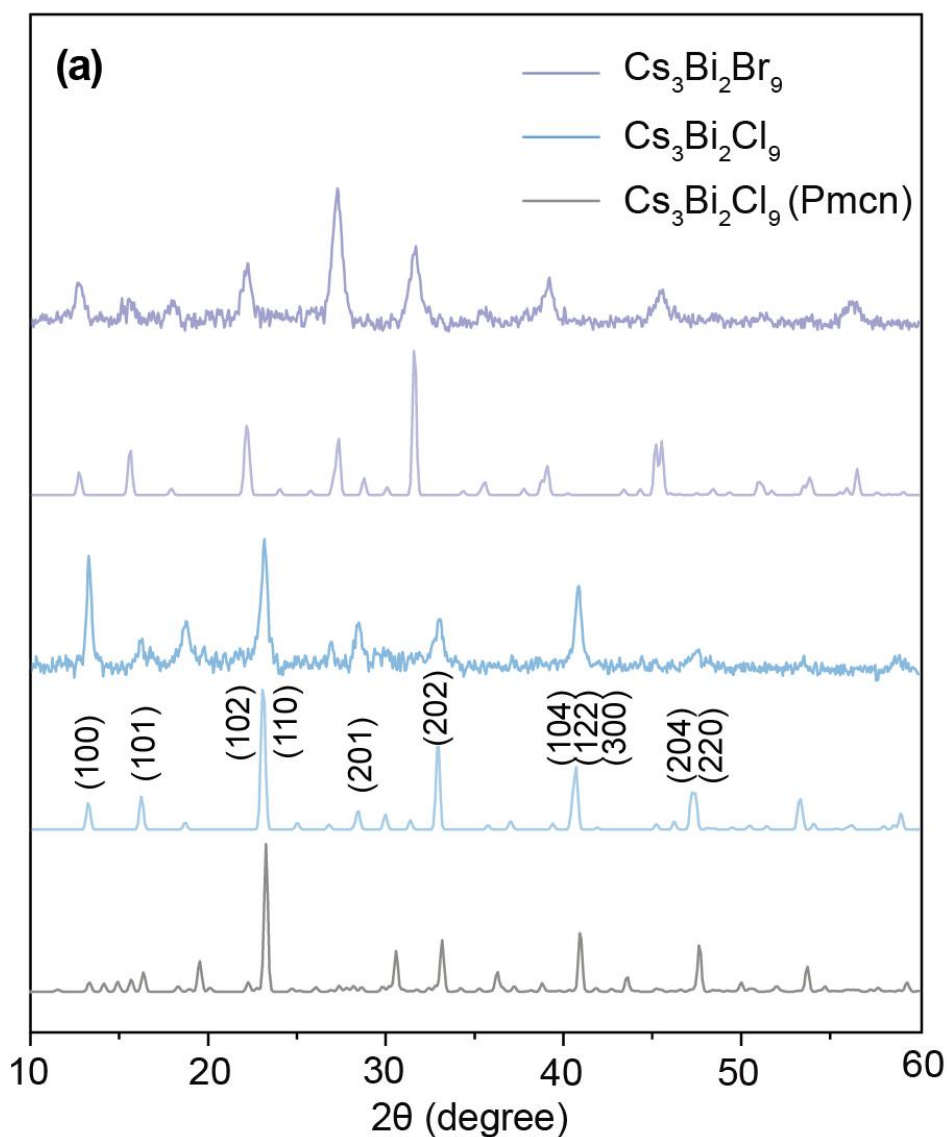


Figure 3.1 PXRD patterns of $\text{Cs}_3\text{Bi}_2\text{X}_9$ NCs compared to reference patterns of $\text{Cs}_3\text{Bi}_2\text{Cl}_9$ (tetragonal, ICSD Coll. Code 432491) and $\text{Cs}_3\text{Bi}_2\text{Br}_9$ (tetragonal, ICSD Coll. Code 1142). The bottom gray line represents the reference patterns of $\text{Cs}_3\text{Bi}_2\text{Cl}_9$ with a Pmncn space group (orthorhombic, ICSD Coll. Code 2067).

Transmission electron microscopy (TEM) images were used to determine the morphology and size of $\text{Cs}_3\text{Bi}_2\text{Cl}_9$ and $\text{Cs}_3\text{Bi}_2\text{Br}_9$ NCs. As shown in Figure 3.2 a and b, most of the NCs exhibit irregular shapes with average sizes of 22 nm ($\text{Cs}_3\text{Bi}_2\text{Cl}_9$) and 20 nm ($\text{Cs}_3\text{Bi}_2\text{Br}_9$). These observations are consistent with previously reported morphologies and sizes.^[31]

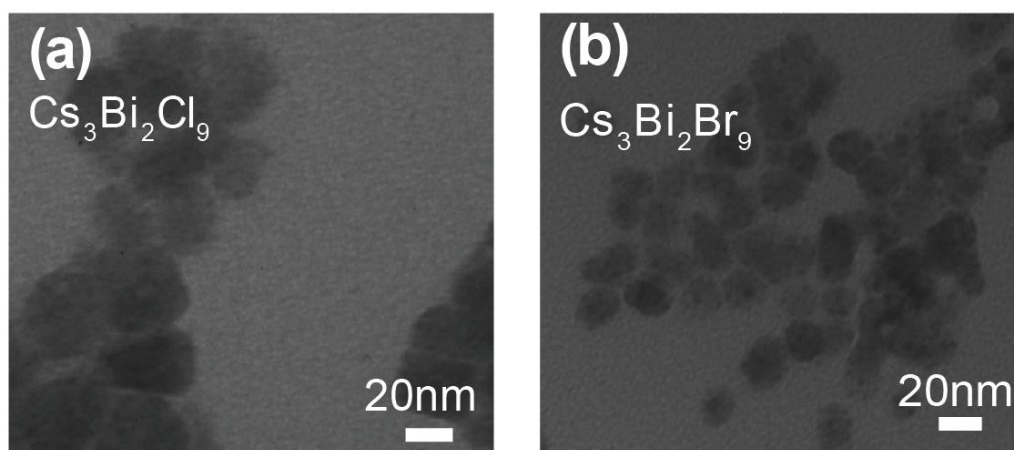


Figure 3.2 TEM characterization of (a) $\text{Cs}_3\text{Bi}_2\text{Cl}_9$ and (b) $\text{Cs}_3\text{Bi}_2\text{Br}_9$ NCs.

3.2 Optical properties of $\text{Cs}_3\text{Bi}_2\text{Cl}_9$ and $\text{Cs}_3\text{Bi}_2\text{Br}_9$ NCs

The absorption spectra of $\text{Cs}_3\text{Bi}_2\text{Cl}_9$ and $\text{Cs}_3\text{Bi}_2\text{Br}_9$ NCs measured at 5 K are presented in Figure 3.3. Both spectra exhibit a distinct peak, with maximum intensities observed at 368 nm for $X = \text{Cl}$ and 428 nm for $X = \text{Br}$. Furthermore, a shoulder is also observed in both spectra at ca. 390 nm for $X = \text{Cl}$ and 458 nm for $X = \text{Br}$. These spectra are consistent with previously reported results.^[31]

As mentioned in chapter 1.3.1, the VBM of $\text{Cs}_3\text{Bi}_2\text{X}_9$ is primarily comprised of halide-p and Bi-6s orbitals, whereas the CBM is predominantly formed by Bi-6p orbitals. Therefore, based on the band structure composition, the origin of the absorption band edge transition in $\text{Cs}_3\text{Bi}_2\text{X}_9$ is widely attributed to the transition between the bismuth 6s-6p orbitals ($^1\text{S}_0 \rightarrow ^3\text{P}_1$).^[31] Additionally, the small peak at higher energy (330 nm for $\text{Cs}_3\text{Bi}_2\text{Cl}_9$ and 380 nm for $\text{Cs}_3\text{Bi}_2\text{Br}_9$) is often considered as the absorption of $\text{Cs}_3\text{Bi}_2\text{X}_6$ impurities in the solution or $^1\text{S}_0 \rightarrow ^3\text{P}_1$ transition in the isolated $[\text{BiX}_6]^{3-}$ octahedra, due to the similarity in peak positions.^{[31][69][120]} However, Geng et al. have reported that both the main peak and the small high-energy peak exhibit size dependency, indicating that they

do not originate from the $^1S_0 \rightarrow ^3P_1$ transition.^[121] Meanwhile, they assigned these two peaks to the transitions of the first exciton and second exciton.^[70] In addition, peaks below 300 nm in and below 350 nm in $\text{Cs}_3\text{Bi}_2\text{Br}_9$ are likely associated with transitions to higher energy states.

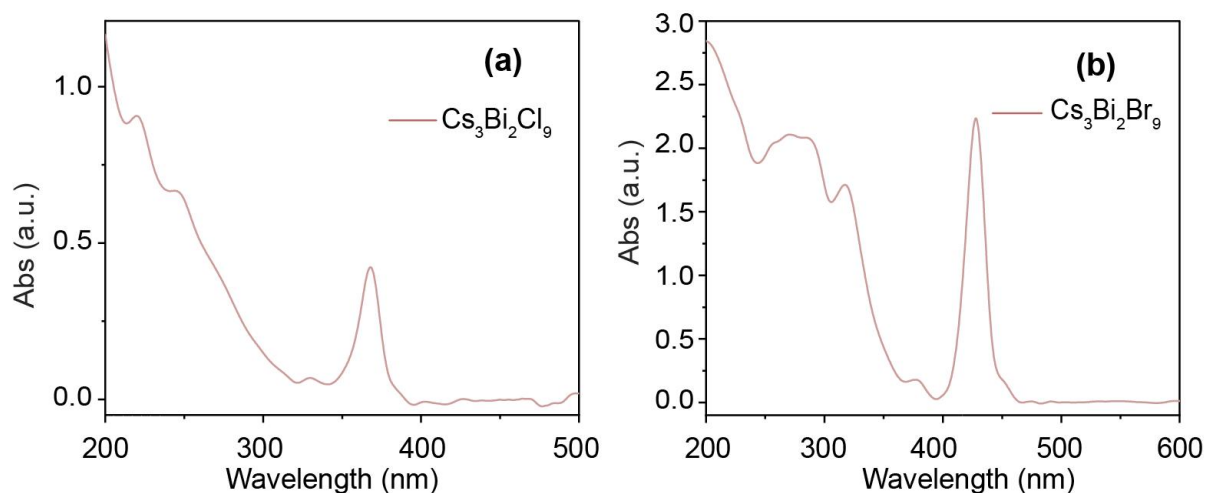


Figure 3.3 Absorption spectra of (a) $\text{Cs}_3\text{Bi}_2\text{Cl}_9$ and (b) $\text{Cs}_3\text{Bi}_2\text{Br}_9$ NCs collected at 5 K.

3.3 Magneto-Optical properties of $\text{Cs}_3\text{Bi}_2\text{Cl}_9$ and $\text{Cs}_3\text{Bi}_2\text{Br}_9$ NCs

To explore the origin of the absorption transition, we performed 7 T MCD measurements on $\text{Cs}_3\text{Bi}_2\text{X}_9$ NCs (Figure 3.4, bottom panels). The black trace in Figure 3.4 shows a normalized MCD spectrum of $\text{Cs}_3\text{Bi}_2\text{X}_9$ NCs. The MCD spectra were normalized by converting the ellipticity (θ) into $\Delta A/A$, as described in eq 3 (chapter 2.3.4). Additionally, various transitions within the absorption region can collectively overlap, resulting in the generation of the MCD signal. For example, the MCD spectrum of $\text{Cs}_3\text{Bi}_2\text{Cl}_9$ consists of structured positive and negative lobes that generally correspond well to the absorption spectrum. The onset of the negative signal is observed at ca. 394 nm, followed by a shoulder around 380 nm. To assign each feature, we deconvolution the

spectrum assuming derivative-shaped signals characteristic for an A -term MCD typically observed for undoped semiconductor materials.^[117] The most prominent derivative-shaped signal (green line) is aligned with the main absorption peak, and can be assigned to direct VB-CB transition. One possible explanation for the tail is the existence of an indirect band-gap transition (purple line). Zhang et al^[122] observed two adjacent peaks in the PL spectra of $\text{Cs}_3\text{Bi}_2\text{X}_9$ NCs at room temperature, which might originate from exciton recombination through direct and indirect transitions. Previous DFT calculations also indicated the presence of direct transitions at the Γ point and low-energy indirect transitions from the Γ point to the A point. Despite the existence of an indirect excitation, these calculations emphasize that the primary optical excitation still occurs at the Γ point^[28]. The shoulder at ca. 380 nm in the MCD spectrum is characterized by much narrower, derivative-shaped peaks. Therefore, this feature may be attributed to the localized exciton around the Bi^{3+} ion (orange line). The pink line shows the cumulative fit to the experimental spectrum. An excellent agreement with the measured spectrum is achieved in the range of ca. 360-400 nm. On the high-energy side of the positive lobe there is a mismatch, which may be related to the existence of higher energy conduction-band excited states in $\text{Cs}_3\text{Bi}_2\text{Cl}_9$.^{[36][71]} As our focus is on the band-edge transitions, this feature has not been extensively investigated.

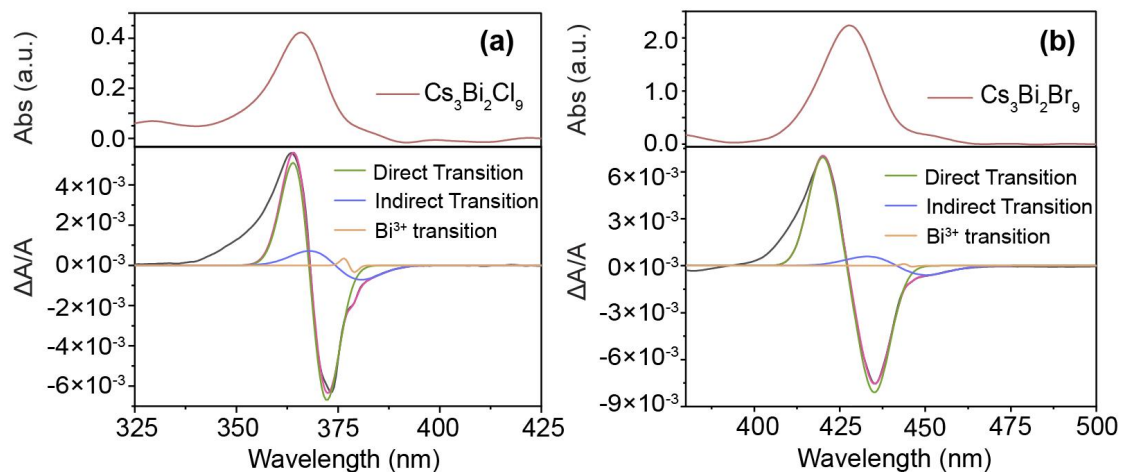


Figure 3.4 Optical absorption (top) and MCD (bottom) spectra of (a) $\text{Cs}_3\text{Bi}_2\text{Cl}_9$ NCs and (b) $\text{Cs}_3\text{Bi}_2\text{Br}_9$ NCs in the band gap region, collected at 7 T and 5 K. (Legend: black line - normalized MCD data; pink line - cumulative peak; green line - simulated direct transition; purple line - simulated indirect transition; orange line - Bismuth s-p transition)

Although it has been established that the CB and VB are primarily composed of Bi 6p orbitals and halogen p orbitals, respectively, it is noteworthy that the contribution of halogen orbitals to the CB increases with the increasing atomic number of the halogen ion.^[123] Therefore, we performed the same analysis for $\text{Cs}_3\text{Bi}_2\text{Br}_9$ NCs to explore the influence of different anions on the electronic structure of these lead-free halide-perovskite-like systems. As shown in Figure 3.4b, the $\text{Cs}_3\text{Bi}_2\text{Br}_9$ samples also exhibit both excitonic direct (green line) and indirect (blue line) transitions. However, the intensity of the excitonic transition localized on Bi^{3+} is noticeably reduced (orange line), possibly because of the higher amount of charge dispersed on Br compared to Cl. This in turn leads to a reduced charge distribution on the Bi centers, reducing the exciton localization.^[123] These results demonstrate that MCD spectroscopy can be used as an effective tool for a deconvolution of the complex excitonic spectra of MHP NCs,

allowing for more specific assignment of the excitonic transitions compared to the optical absorption spectroscopy.

Using MCD spectra, we also calculated the excitonic Zeeman splitting (ΔE_Z) and Lande g-factor for both samples by equation 4 and equation 5 (chapter 2.3.4). The calculated Zeeman splitting for the direct excitonic transition in $\text{Cs}_3\text{Bi}_2\text{Cl}_9$ is $\Delta E_Z = 0.50$ meV, with the corresponding g-value of $g=1.24$. For $\text{Cs}_3\text{Bi}_2\text{Br}_9$, $\Delta E_Z = 0.63$ meV, with $g=1.56$. One potential explanation for the increased Zeeman splitting and exciton g-factor determined for $\text{Cs}_3\text{Bi}_2\text{Br}_9$ is the larger SOC effect. This phenomenon is influenced by the halide composition of MHP materials. The Hamiltonian for SOC can be generally formulated as:

$$H_{\text{SOC}} = \frac{\hbar}{4m_0^2c^2} * \mathbf{p} * \boldsymbol{\sigma} * \nabla V_0 \quad (4)$$

where V_0 represents the Coulomb potential acting the electron, m_0 and \mathbf{p} are the electron mass and momentum, respectively, c is the velocity of light, and $\boldsymbol{\sigma} = (\sigma_x, \sigma_y, \sigma_z)$ denotes the vector of Pauli spin matrices.^[96] In halide perovskites containing heavy nuclei (e.g., Pb, Bi, I), SOC becomes significant, because it is directly proportional to the gradient of the Coulomb potential ∇V_0 , and \mathbf{p} .^{[96][124]} Due to the higher atomic number of Br, there is an associated increase in the effective nuclear charge, which subsequently enhances the gradient of the Coulomb potential in $\text{Cs}_3\text{Bi}_2\text{Br}_9$ relative to $\text{Cs}_3\text{Bi}_2\text{Cl}_9$. As a result, SOC is larger in the $\text{Cs}_3\text{Bi}_2\text{Br}_9$ compared to $\text{Cs}_3\text{Bi}_2\text{Cl}_9$ NCs. The SOC is responsible for splitting of the electronic band states, which in turn results in greater ΔE_Z and the corresponding g-factor.

To further investigate the origin of excitonic splitting, the MCD spectra of $\text{Cs}_3\text{Bi}_2\text{Cl}_9$

(Figure 3.5a) and $\text{Cs}_3\text{Bi}_2\text{Br}_9$ (Figure 3.5b) NCs were collected at different temperatures from 5 to 300 K.

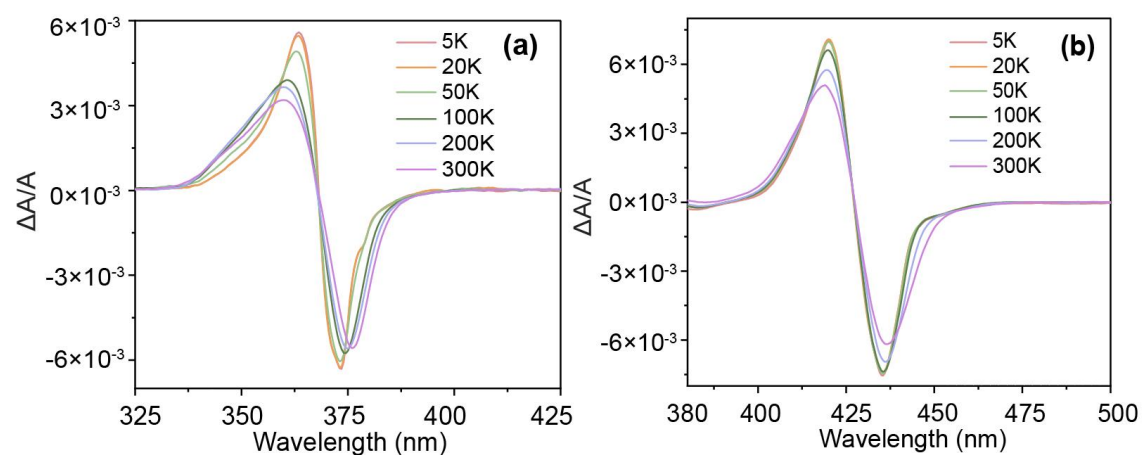


Figure 3.5 MCD spectra of (a) $\text{Cs}_3\text{Bi}_2\text{Cl}_9$ and (b) $\text{Cs}_3\text{Bi}_2\text{Br}_9$ NCs across various temperatures.

The deconvolution of $\text{Cs}_3\text{Bi}_2\text{Cl}_9$ and $\text{Cs}_3\text{Bi}_2\text{Br}_9$ NCs at different temperatures was conducted to analyze the changes in each component with increasing temperature. The detailed fitting plots are shown in Appendix A (Figure A.1 and Figure A.2). Moreover, temperature dependence of the integrated intensities of the positive and negative MCD signals for $\text{Cs}_3\text{Bi}_2\text{Cl}_9$ NCs are shown in Figure 3.6a for direct band gap transition, and Figure 3.6b for indirect band gap transition. The analogous data for $\text{Cs}_3\text{Bi}_2\text{Br}_9$ NCs are shown in Figure 3.6c and d. The intensities of the positive and negative lobe of the MCD signal change symmetrically for both direct and indirect band gap transitions. The direct band gap transitions remain largely unchanged as the temperature increases from 5 to 50 K, followed by a gradual decrease in intensity with a further increase in temperature (Figure 3.6 a,c). As the temperature rises above ca. 100 K, phonon modes become more active, leading to exciton dissociation, consequently weakening the band gap transitions. Additionally, a strong exciton-phonon coupling has been reported before, which also

potentially influences both direct and indirect band gap transition.^[30] In contrast, below 50 K, phonon modes are very weak, resulting in minimal changes of the MCD signal intensities. The indirect band gap transitions follow similar behavior below ca. 50 K and above 100 K, but show a noticeable increase in intensity between 50 and 100 K (Figure 3.6 b and d). A plausible cause of a change in the indirect band gap MCD intensity at 100 K is the occurrence of the phase transition.^[30] Due to the soft lattice nature of MHPs, the $[\text{BiX}_6]^{3-}$ octahedra exhibit structural changes when subjected to external stimuli.^[125] The presence of Bi^{3+} $6s^2$ lone electron pair induces intra-octahedral distortion, leading to off-centering of the Bi^{3+} site while preserving a $P\bar{3}m1$ trigonal lattice structure upon reducing the temperature from 300 to 100 K.^[126] A phase transition occurs between 100 and 90 K on cooling down the samples, which modifies the crystallographic identities of the $[\text{BiX}_6]^{3-}$ octahedral layers without affecting their c-axis alignment.^[123] Below 100 K, further intra-octahedral distortion takes place ultimately leading to a transition from a trigonal to a monoclinic lattice structure.^[126]

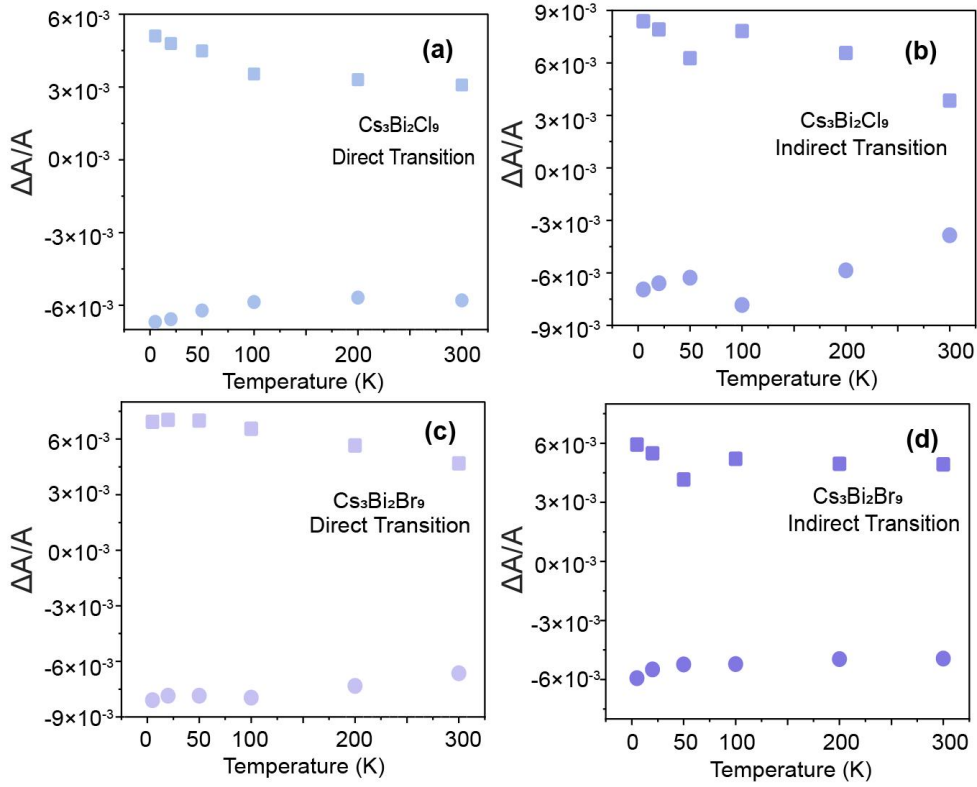


Figure 3.6 (a) Integrated intensity of both negative and positive bands for direct transitions in $\text{Cs}_3\text{Bi}_2\text{Cl}_9$ NCs; (b) Integrated intensity of both negative and positive bands for indirect transitions in $\text{Cs}_3\text{Bi}_2\text{Cl}_9$ NCs; (c) Integrated intensity of both negative and positive bands for direct transitions in $\text{Cs}_3\text{Bi}_2\text{Br}_9$ NCs; (d) Integrated intensity of both negative and positive bands for indirect transitions in $\text{Cs}_3\text{Bi}_2\text{Br}_9$ NCs.

3.4 Conclusion

In this chapter, we used MCD spectroscopy, as an alternative method, to investigate the electronic structure of lead-free MHP NCs, with a particular emphasis on the origin of the excitonic transitions and their Zeeman splitting. Robust MCD signal was observed up to room temperature for $\text{Cs}_3\text{Bi}_2\text{X}_9$ NCs, with the Zeeman splitting energy and the corresponding g-factor comparable to those reported for conventional lead halide perovskite NCs.^[98] Halide composition is found to have a strong effect on the Zeeman

splitting energy and the corresponding g-factor, increasing ΔE_Z increasing from 0.502 to 0.632 meV and g increasing from ca. 1.24 to 1.56 by substituting Cl for Br. This work provides the first direct measurements of excitonic Zeeman splitting in lead-free MHP NCs at room temperature, demonstrating their promise for technological applications in spintronics and opto-electronics. Composition-dependent MCD results determined in this work suggest that magneto-optical properties of MHP can be further improved through structure and composition, while reducing their toxicity and increasing their stability.

Chapter 4 Magneto optical properties of double perovskites

4.1 Cs₂AgBiX₆ NCs

4.1.1 Structural characterization of Cs₂AgBiCl₆ and Cs₂AgBiBr₆

The X-ray diffraction patterns that we collected for Cs₂AgBiX₆ NCs (Figure 4.1) are in very good agreement with those previously reported Cs₂AgBiCl₆ and Cs₂AgBiBr₆ materials. Some minor peaks were not observed, which is likely due to peak broadening associated with small NC sizes. Both NCs exhibit a cubic structure with a Fm $\bar{3}$ m space group. A shift to lower angles can be observed when transitioning from Cl to Br, attributed to the larger ionic radius of Br⁻. Additionally, variations in the relative intensities of some peaks are due to changes in the in-plane orientation within the crystal structure.

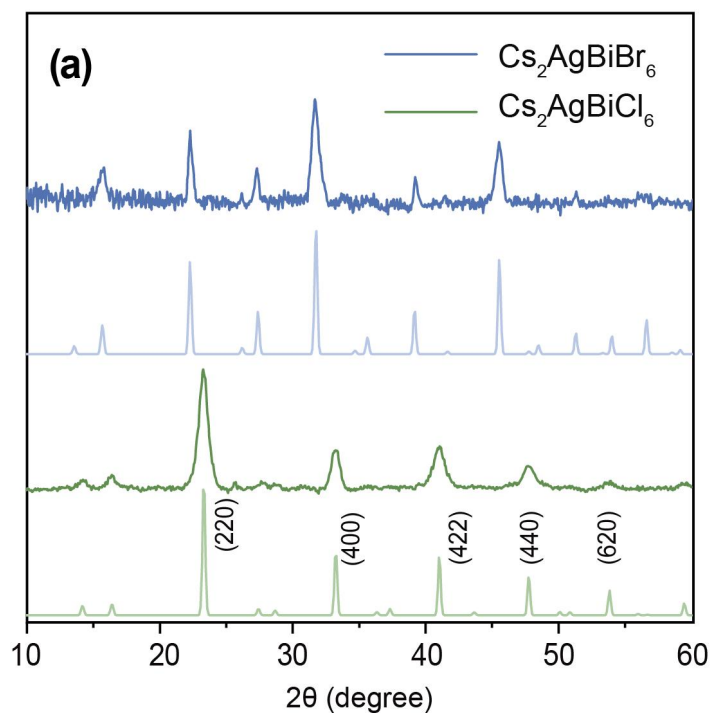


Figure 4.1 PXR D patterns of Cs₂AgBiX₆ NCs compared to reference patterns of Cs₂AgBiCl₆ (ICSD Coll. Code 291598) and Cs₂AgBiBr₆.

Additionally, TEM images were used to determine the morphology for $\text{Cs}_2\text{AgBiCl}_6$ and $\text{Cs}_2\text{AgBiBr}_6$ NCs (Figure 4.2). The majority of the nanocrystals are highly crystalline, exhibiting a cubic shape, which is consistent with previously reported morphologies.^[127] $\text{Cs}_2\text{AgBiCl}_6$ exhibits a size length of 8.52 ± 1.00 nm, while $\text{Cs}_2\text{AgBiBr}_6$ shows a side length of 7.79 ± 0.61 nm.

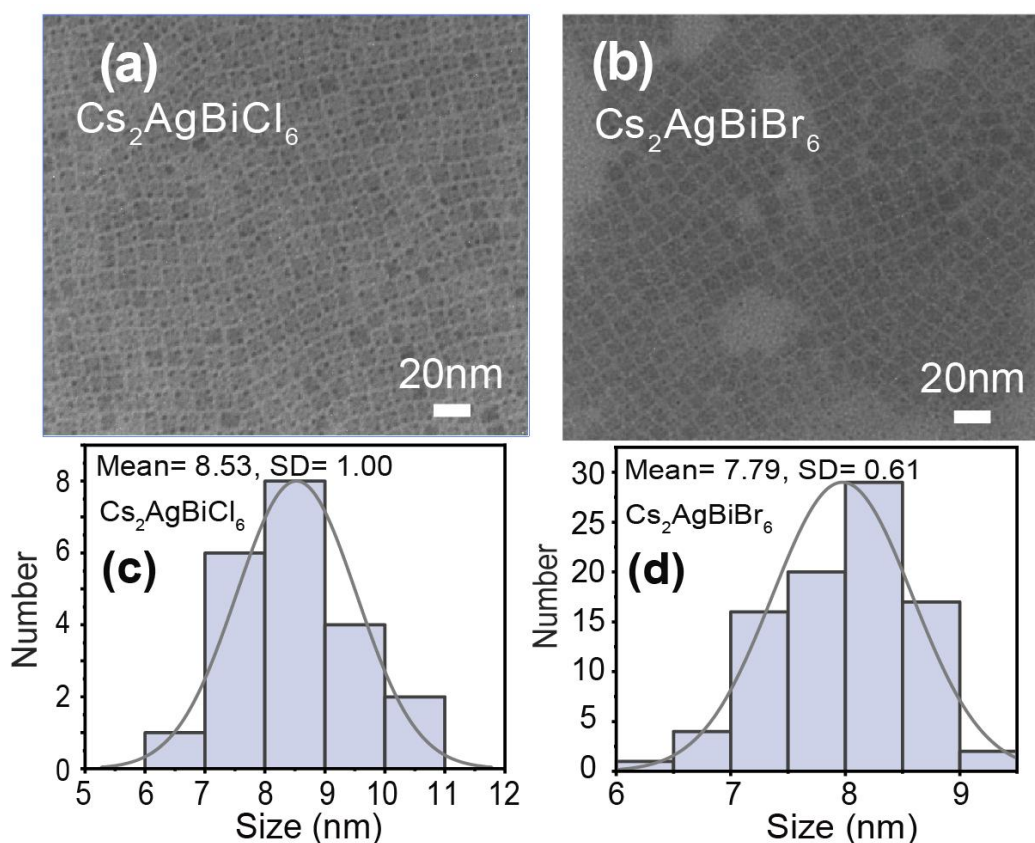


Figure 4.2 TEM characterization of (a) $\text{Cs}_2\text{AgBiCl}_6$ and (b) $\text{Cs}_2\text{AgBiBr}_6$ NCs. Size distribution diagram for (c) $\text{Cs}_2\text{AgBiCl}_6$ and (d) $\text{Cs}_2\text{AgBiBr}_6$ NCs determined from TEM image. The average NCs sizes and standard deviations are shown in the corresponding graphs.

4.1.2 Optical properties of $\text{Cs}_2\text{AgBiCl}_6$ and $\text{Cs}_2\text{AgBiBr}_6$ NCs

The 5 K absorption spectra of $\text{Cs}_2\text{AgBiCl}_6$ and $\text{Cs}_2\text{AgBiBr}_6$ NCs are presented in

Figure 4.3a and Figure 4.3b. respectively. A well-defined feature is observed at ca.369 nm for $X = \text{Cl}$ and 427 nm for $X = \text{Br}$, consistent with previously reported results.^[114] $\text{Cs}_2\text{AgBiX}_6$ compounds are typically considered to have an indirect band gap transition, where the CB minimum is located at the Γ point and the VB maximum is located at the X point. Previous calculations of bandgap values at various k-points have provided a detailed understanding of how different electronic states contribute to the band edges.^[128] The main features observed in our absorption spectra correspond more closely to the direct bandgap character at the X point.^{[128][129]}

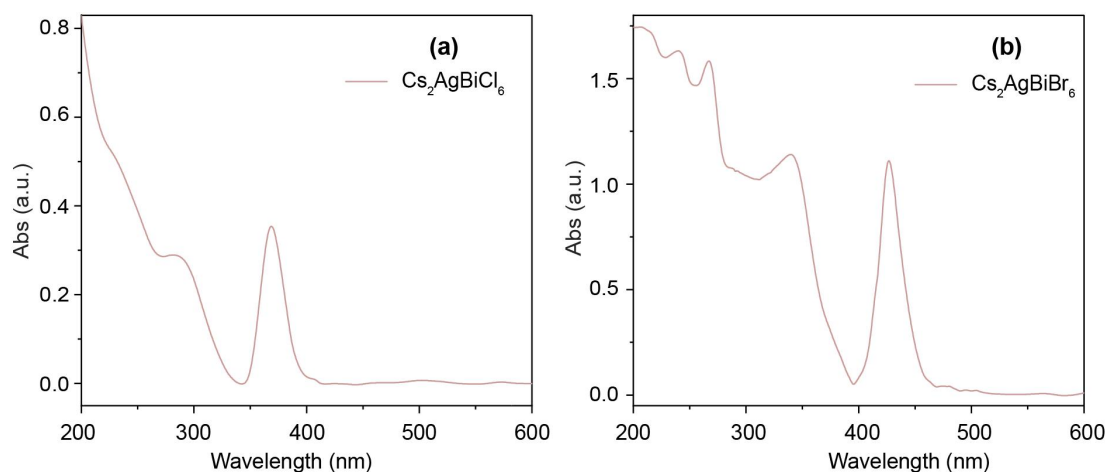


Figure 4.3 Absorption spectra of (a) $\text{Cs}_2\text{AgBiCl}_6$ and (b) $\text{Cs}_2\text{AgBiBr}_6$ NCs collected at 5 K.

However, the nature of absorption remains controversial. The origin of the excitonic absorption peak in $\text{Cs}_2\text{AgBiX}_6$ has been reported but remains inconclusive. Dey et al.^[130] attributed the prominent absorption peak in $\text{Cs}_2\text{AgBiBr}_6$ to defect-related bound excitons, while Lv et al.^[131] suggested that this peak arises from the formation of free excitons just below the conduction band. Zelewski et al.^[132] reported that the reflection spectrum of $\text{Cs}_2\text{AgBiBr}_6$ at 2.8 eV shows resonance features indicative of band-edge and free exciton absorption. Furthermore, Wright et al. observed ultrafast localization of charge carriers in

$\text{Cs}_2\text{AgBiBr}_6$. However, due to the high binding energy, they were unable to confirm the formation of free excitons (Mott exciton) during initial excitation.^[133] In addition, there are multiple peaks occur at high energy range, which are related to the higher energy states.

4.1.3 Magneto-Optical properties of $\text{Cs}_2\text{AgBiCl}_6$ and $\text{Cs}_2\text{AgBiBr}_6$ NCs

To better investigate the origin and nature of the absorption transitions in the band gap energy region for $\text{Cs}_2\text{AgBiX}_6$, variable-field MCD measurements were conducted, shown in Figure 4.4. The MCD signal arises from Zeeman splitting, which is the magnetic field-induced perturbation affecting the electronic states that participate in the absorption transitions.^[117] The derivative-shaped MCD spectra, consisting of a combination of positive and negative bands, are aligned with the band gap absorption for both samples. These signals are associated with the differential absorptions of left and right circularly polarized light, and are characteristic for an A -term MCD. The asymmetric band shapes of the MCD signals may result from the mixing of states with different characteristics. Especially, in $\text{Cs}_2\text{AgBiBr}_6$, the shoulder observed at ca. 412.5 nm across all fields confirms this assumption.

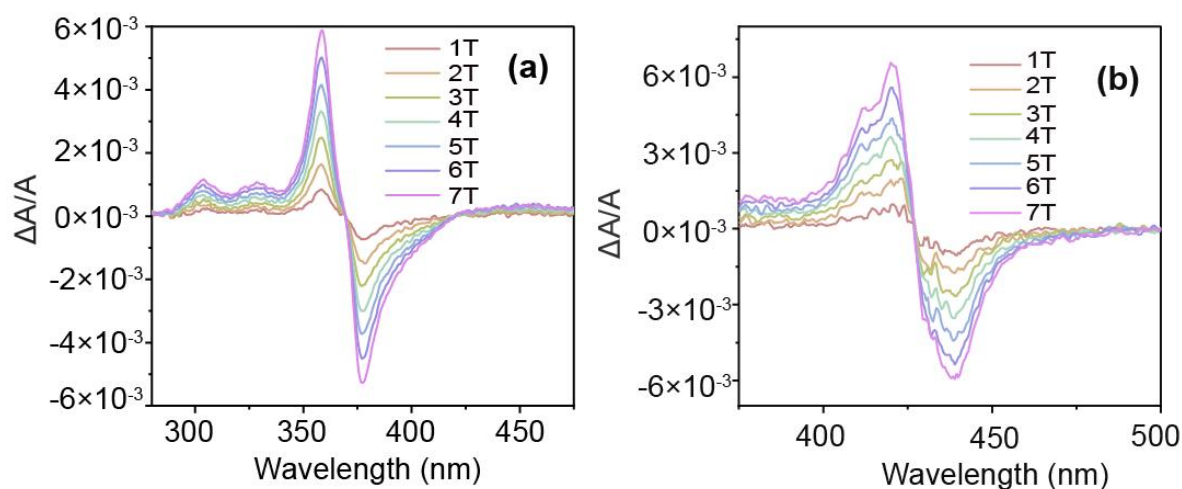


Figure 4.4 MCD spectra of (a) $\text{Cs}_2\text{AgBiCl}_6$ and (b) $\text{Cs}_2\text{AgBiBr}_6$ NCs collected at 5 K and different external magnetic field strengths (1-7 T), as indicated in the graph.

To achieve a more precise analysis of the individual components, deconvolution was applied to these spectra, allowing for a deconvolution of various contributing transitions (Figure B.1 and B.3 in Appendix). Using MCD spectra collected at 5 K and 7 T as an example, shown in Figure 4.5a and b, two distinct derivative-shaped signals can be identified. These features correspond to direct (purple line) and bound (green line) exciton transitions, which are present simultaneously.^{[130][132]} The formation of bound excitons is primarily due to internal defects. Li et al.^[134] reported the potential for various defects in double perovskites, identifying Ag^+ vacancies as the most stable and readily formed. These shallow vacancies occur at the valence band edge, acting as hole traps and localizing the holes in the valence band. The highly flat localized state leads to an infinite effective mass of the trapped hole. The trapped hole then forms a bound exciton with the heavy electron.^[130] The low energy region (400 to 425 nm) of the MCD spectrum of $\text{Cs}_2\text{AgBiCl}_6$ shows a well-defined shoulder. Since the indirect band gap transitions generally occur at much lower energies (around 600 nm), this assignment can be ruled out.^{[67][135]} The observed long tail in this region may be attributed to minor defects in the

lattice structure.^[128]

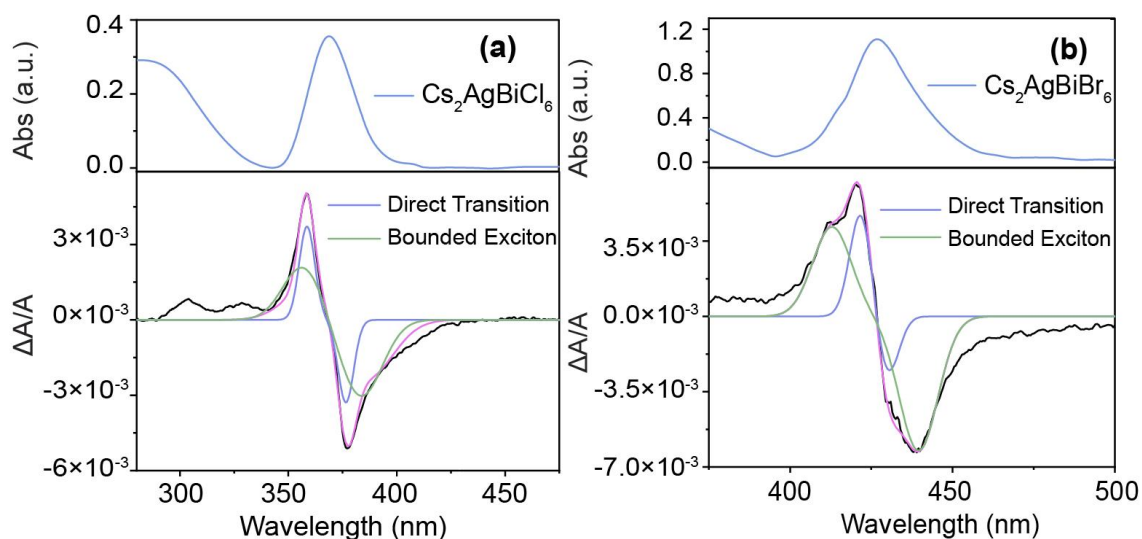


Figure 4.5 Optical absorption (top) and MCD (bottom) spectra of (a) $\text{Cs}_2\text{AgBiCl}_6$ and (b) $\text{Cs}_2\text{AgBiBr}_6$ NCs in the band gap region, collected at 7 T and 5 K. (Legend: black line - normalized MCD data; pink line - cumulative peak; blue line - simulated direct transition; green line - simulated bound exciton transition)

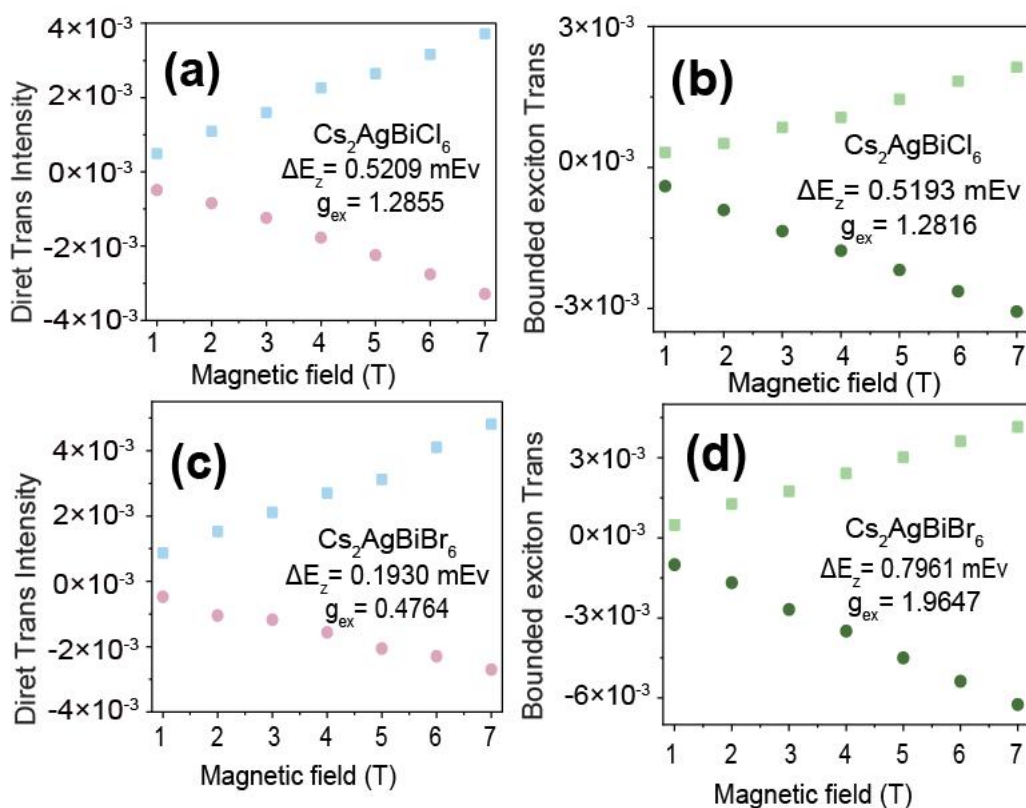


Figure 4.6 (a) Integrated intensity of both negative and positive bands for direct transitions in $\text{Cs}_2\text{AgBiCl}_6$ NCs; (b) Integrated intensity of both negative and positive

bands for bound exciton transitions in Cs₂AgBiCl₆ NCs; (c) Integrated intensity of both negative and positive bands for direct transitions in Cs₂AgBiBr₆ NCs; (d) Integrated intensity of both negative and positive bands for bound exciton transitions in Cs₂AgBiBr₆ NCs.

The *A*-term characteristic, exhibited by the MCD signal, indicates Zeeman splitting of the originally degenerate excited states. The Zeeman effect arises from the splitting of the energy levels of the electrons and holes that form the exciton.^[136] Direct (Figure 4.6a) and bound (Figure 4.6b) exciton transitions in Cs₂AgBiCl₆ NCs both show a linear increase in intensity with increasing magnetic field strength (see also Figure B.1 and B.3 in Appendix B). The linear behavior indicates a diamagnetic nature of the NCs, as expected. The Zeeman splitting and the corresponding *g* factors for these transitions for a 7 T magnetic field have been calculated; the direct excitonic transition has a Zeeman splitting of 0.52 meV with a *g* factor of 1.29 (Figure 6a), while the bound exciton has a Zeeman splitting of 0.52 meV with a *g* factor of 1.28 (Figure 4.6b). Similarly, the deconvoluted intensities for the direct and bound excitonic transitions in Cs₂AgBiBr₆ NCs are shown in Figure 4.6c and 4.6d, respectively. Interestingly, for Cs₂AgBiBr₆ NCs our results indicate that the bound excitonic transition dominates the excitonic absorption region. The direct excitonic transition in Cs₂AgBiBr₆ exhibits a Zeeman splitting of 0.19 meV with a *g* factor of 0.48 (Figure 4.6c), while the bound exciton shows a Zeeman splitting of 0.80 meV with a *g* factor of 1.96 (Figure 4.6d). The bound excitonic absorption in Cs₂AgBiBr₆ is more pronounced than in Cs₂AgBiCl₆ due to the lower formation energy of Ag vacancies (V_{Ag}) in Cs₂AgBiBr₆ compared to Cs₂AgBiCl₆, which facilitates the formation of bound excitons around these defects.^[128] It is also noteworthy

that the direct electronic transition exhibits asymmetric positive and negative bands in $\text{Cs}_2\text{AgBiBr}_6$ NCs. This asymmetry may be attributed to the strong electron-phonon coupling in $\text{Cs}_2\text{AgBiBr}_6$.^[137] Phonon interactions could alter the probabilities of electronic transitions for left and right circularly polarized light, resulting in asymmetric MCD signals.^[138] Moreover, as discussed earlier, the direct band gap transition occurs at the X point, while the conduction band minimum is located at the Γ point. This leads to the electron scattering toward the lowest energy state. The exciton-phonon coupling stabilizes the excited state as a polaron through collective lattice distortion. Similar results have been observed in hybrid lead perovskites.^[139]

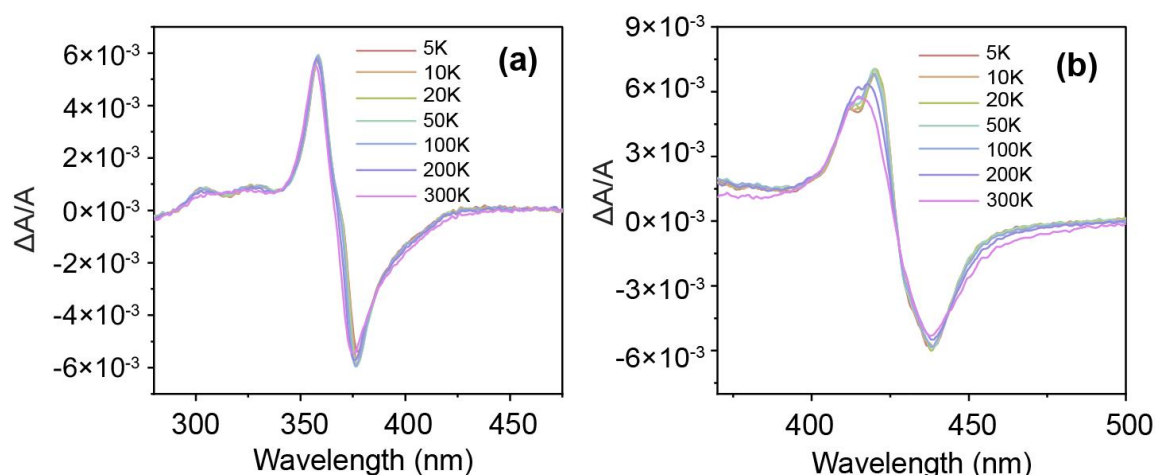


Figure 4.7 Normalized 7 T field MCD spectra of (a) $\text{Cs}_2\text{AgBiCl}_6$ and (b) $\text{Cs}_2\text{AgBiBr}_6$ NCs at temperatures ranging from 5 K to 300 K.

To further elucidate the origin of excitonic splitting, the MCD spectra of $\text{Cs}_2\text{AgBiCl}_6$ and $\text{Cs}_2\text{AgBiBr}_6$ nanocrystals were measured at various temperatures ranging from 5 K to 300 K. Figure 4.7a and b shows the normalized MCD spectra. MCD signal intensity for $\text{Cs}_2\text{AgBiCl}_6$ NCs exhibits mostly temperature-independent behavior, while the peak for $\text{Cs}_2\text{AgBiBr}_6$ NCs around 420 nm shows a notable decrease in intensity with increasing

temperature. Consequently, we deconvoluted the MCD signals for both samples at different temperatures (Figure B.2 and B.4 in Appendix B) and compared the relative change in intensity at various temperatures with respect to the intensity at 5 K (Figure 4.8).

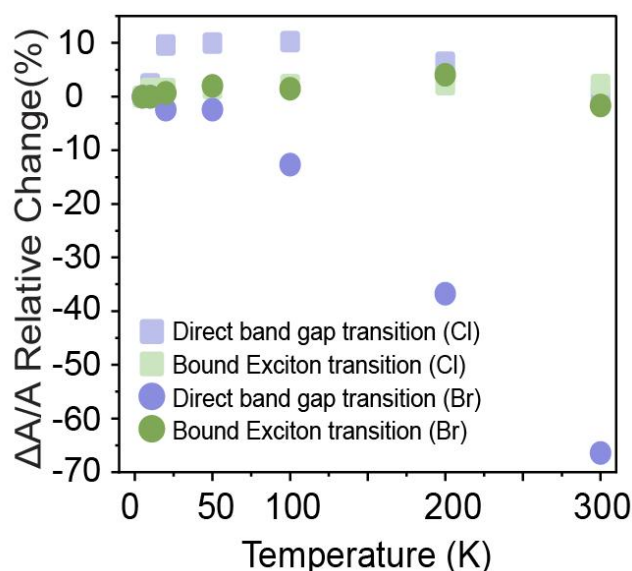


Figure 4.8 Relative change of $\Delta A/A$ for $\text{Cs}_2\text{AgBiCl}_6$ and $\text{Cs}_2\text{AgBiBr}_6$ NCs at various temperatures compared to 5 K

At low temperatures (below 100K), the change in temperature is not significant. A small increase in thermal excitation within the material may lead to the generation of more excitons and a slight increase in MCD signal intensity with temperature in this temperature range.^[133] At high temperatures (above 100K), phonon modes start to become active. Lei et al.^[140] reported the carrier-phonon coupling constants for acoustic phonons ($\gamma_{ac} = 81 \pm 16 \mu\text{eV}$) and LO phonons ($\gamma_{LO} = 226 \pm 14 \text{ meV}$), which are significantly larger than the carrier-phonon coupling constants typically found in lead-based perovskites, usually ranging from 40 to 60 meV. Therefore, the intensities of both direct band gap and the bound exciton transitions in both samples decrease with increasing temperature, likely due to increased phonon activity causing exciton dissociation.^[9] Moreover, at higher

temperatures, the mobility of charge carriers in localized states increases, resulting in a long tail at low-energies.^[133] Additionally, compared to $\text{Cs}_2\text{AgBiCl}_6$, $\text{Cs}_2\text{AgBiBr}_6$ exhibits stronger temperature dependence, particularly for the direct band gap transition. For example, deconvolution analysis for the $\text{Cs}_2\text{AgBiBr}_6$ NCs at 300 K revealed that bound exciton remains dominant at high temperatures, while the direct excitonic transition decreases significantly (Figure A2.2). This behavior is consistent with the expected temperature dependence of free excitons.^[9] The temperature dependence due to halide anion variation is also observed in lead-based perovskites, with CsPbCl_3 showing temperature independence and CsPbBr_3 displaying relatively strong temperature dependence.^[141] One possible explanation for the MCD behavior at different temperatures is that the valence band is primarily composed of spin-split states of Bi^{3+} , with the negligible contribution of Cl to the split-off state. In contrast, bromide has a relatively stronger influence on spin-orbit coupling, thus exhibiting temperature dependence at higher temperature.

4.2 $\text{Cs}_2\text{AgInCl}_6$ NCs

4.2.1 Structural characterization of $\text{Cs}_2\text{AgInCl}_6$ NCs

$\text{Cs}_2\text{AgInCl}_6$ were synthesized by a hot injection method (Chapter 2.2.1).^[81] The XRD pattern of $\text{Cs}_2\text{AgInCl}_6$ and its corresponding reference pattern are shown in Figure 4.9a. $\text{Cs}_2\text{AgInCl}_6$ crystallizes in a cubic unit cell with the space group $\text{Fm}\bar{3}\text{m}$. Our sample demonstrates a good match with the reference pattern.

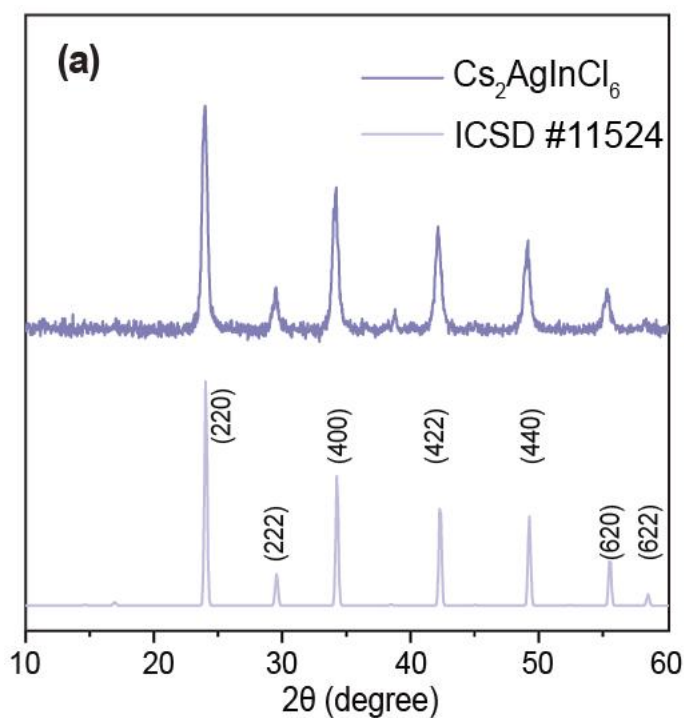


Figure 4.9 (a) PXRD patterns of $\text{Cs}_2\text{AgInCl}_6$ NCs compared to reference patterns of $\text{Cs}_2\text{AgInCl}_6$ (cubic, ICSD Coll. Code #11524).

Figure 4.10 a and b exhibit the TEM image and the size distribution of $\text{Cs}_2\text{AgInCl}_6$ NCs, showing a cubic morphology with an average diameter of 13.08 ± 1.39 nm.

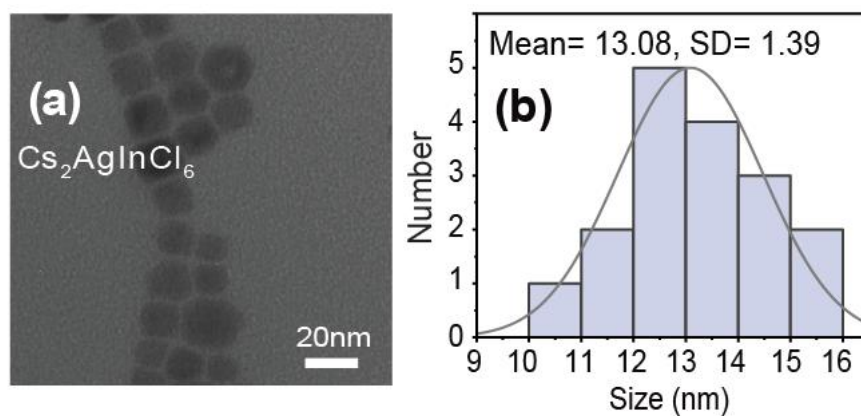


Figure 4.10 (a) TEM image of $\text{Cs}_2\text{AgInCl}_6$ NCs (b) Size distribution diagram of $\text{Cs}_2\text{AgInCl}_6$. The average NCs sizes and standard deviations are shown in the graph.

4.2.2 Optical and Magneto-optical properties of $\text{Cs}_2\text{AgInCl}_6$ NCs

The absorption spectra, displayed in the top panel of Figure 4.11, show an increase

in absorption around 300 nm, which is consistent with previous reports.^[80] As we mentioned in Chapter 1.3.2.2, $\text{Cs}_2\text{AgInCl}_6$ NCs exhibits direct band gap properties, with both the VBM and the CBM located at the Γ point. However, due to the same parity between VBM (Γ_3^+) and CBM (Γ_1^+), the main transition occur from the second lower valence band state (Γ_4^-) to the CBM (Γ_1^+).^[78] Moreover, since the conduction band state at the adjacent L point (L_2^-) has opposite parity, optical transitions near the Γ point become possible, which may result in very weak light absorption near the band gap.^[78] However, this was not observed in our absorption spectrum, likely due to the extremely low absorption coefficient.

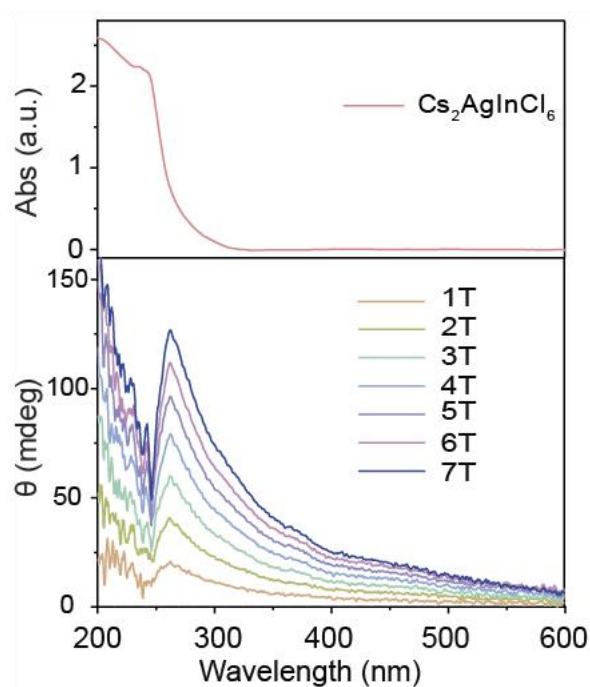


Figure 4.11 Optical absorption spectrum of $\text{Cs}_2\text{AgInCl}_6$ NCs (top) and MCD spectra of $\text{Cs}_2\text{AgInCl}_6$ NCs at different magnetic fields (bottom).

MCD measurements can detect weak transitions that are not observable in optical absorption spectra.^[111] Therefore, we conducted variable-field and variable-temperature MCD measurements on $\text{Cs}_2\text{AgInCl}_6$ NCs. The 5 K variable-field MCD spectra of

$\text{Cs}_2\text{AgInCl}_6$ NCs are shown in the bottom panel of Figure 4.11. The MCD spectra are dominated by an intense peak at 262 nm, which is assigned to the transition from the second lower valence band state (Γ_4^-) to the CBM (Γ_1^+).^[78] A weak shoulder at ca. 400 nm is likely associated with optical absorption near the band gap.^[78]

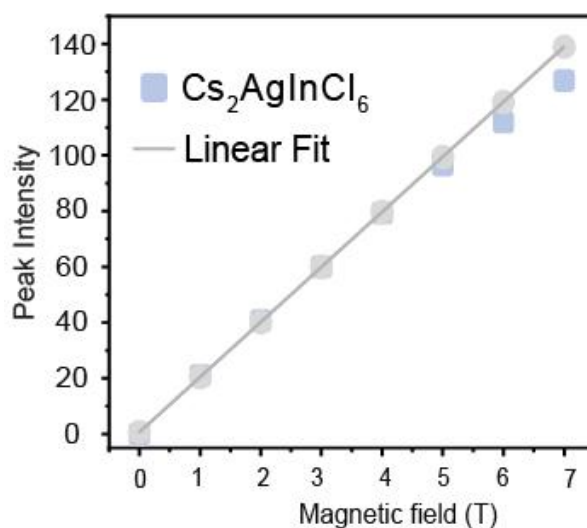


Figure 4.12 Maximum peak intensity of $\text{Cs}_2\text{AgInCl}_6$ from 1 T to 7 T with best-fit linear line.

Figure 4.12 plots the intensity of the experimental MCD signal at the peak maximum as a function of the magnetic field (blue markers), accompanied by its corresponding best-fit linear line (depicted in gray). The data show linear behavior with a slight saturation at high fields. This saturation behavior might be due to spin induced band splitting enabled by photon-induced formation of paramagnetic Ag^{2+} ions. Similar results have been reported in Ag-doped CdSe.^[142] During this process, electrons are photoexcited into the CB, with some of these electrons becoming trapped on surface defect states. Consequently, the photogenerated holes in the VB are captured by nonmagnetic Ag^+ ($4d^{10}$) sites, transforming them into the magnetic Ag^{2+} $4d^9$ species. Given that only a small fraction of Ag^+ is oxidized, the saturation behavior is not very pronounced.

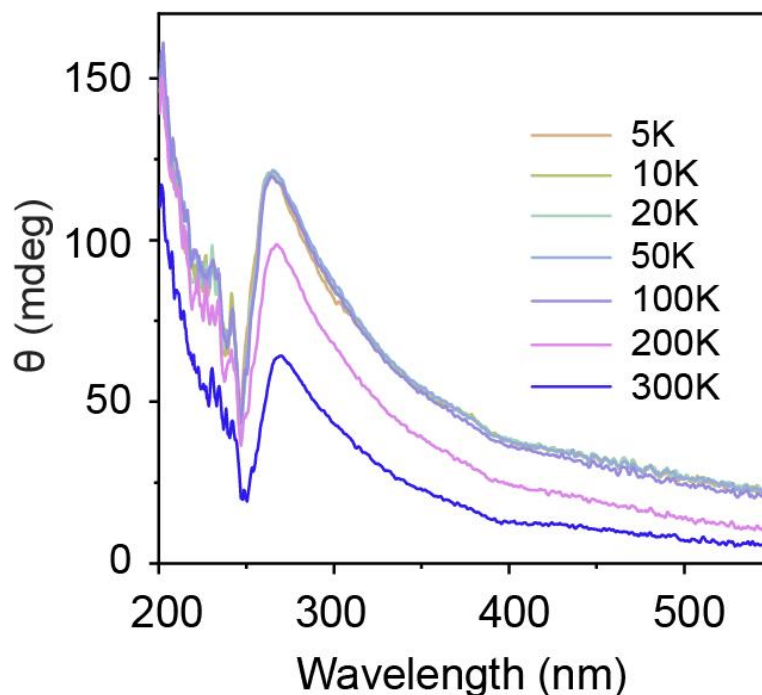


Figure 4.13 Variable temperature MCD spectra of $\text{Cs}_2\text{AgInCl}_6$ NCs.

In addition, the variable-temperature MCD measurements for $\text{Cs}_2\text{AgInCl}_6$ NCs are shown in Figure 4.13. $\text{Cs}_2\text{AgInCl}_6$ NCs exhibit temperature independence from 5 K to 100 K, after which the main peak decreases in intensity with further increase in temperature. This is likely due to enhanced exciton dissociation at higher temperatures, resulting in reduced MCD intensity.

4.3 $\text{Cs}_2\text{AgIn}_{0.5}\text{Bi}_{0.5}\text{Cl}_6$ NCs

4.3.1 Structural characterization of $\text{Cs}_2\text{AgIn}_{0.5}\text{Bi}_{0.5}\text{Cl}_6$ NCs

The synthesis of $\text{Cs}_2\text{AgBi}_{0.5}\text{In}_{0.5}\text{Br}_6$ is similar to that of $\text{Cs}_2\text{AgInCl}_6$, also employing the hot-injection method (as described in Section 2.2.1).^[81] The XRD pattern that we collected for $\text{Cs}_2\text{AgBi}_{0.5}\text{In}_{0.5}\text{Cl}_6$ NCs (Figure 4.14) is in very good agreement with those previously reported materials. Bi^{3+} -doped $\text{Cs}_2\text{AgInCl}_6$ NCs exhibit a crystal structure similar to that of $\text{Cs}_2\text{AgInCl}_6$, with a cubic space group of $\text{Fm}\bar{3}\text{m}$. In comparison with the

$\text{Cs}_2\text{AgInCl}_6$ sample, the XRD peaks of the Bi^{3+} -doped sample shift to smaller angles. This shift is consistent with lattice expansion caused by the substitution of smaller In^{3+} ions (ionic radius 94 pm) with larger Bi^{3+} ions (ionic radius 117 pm).

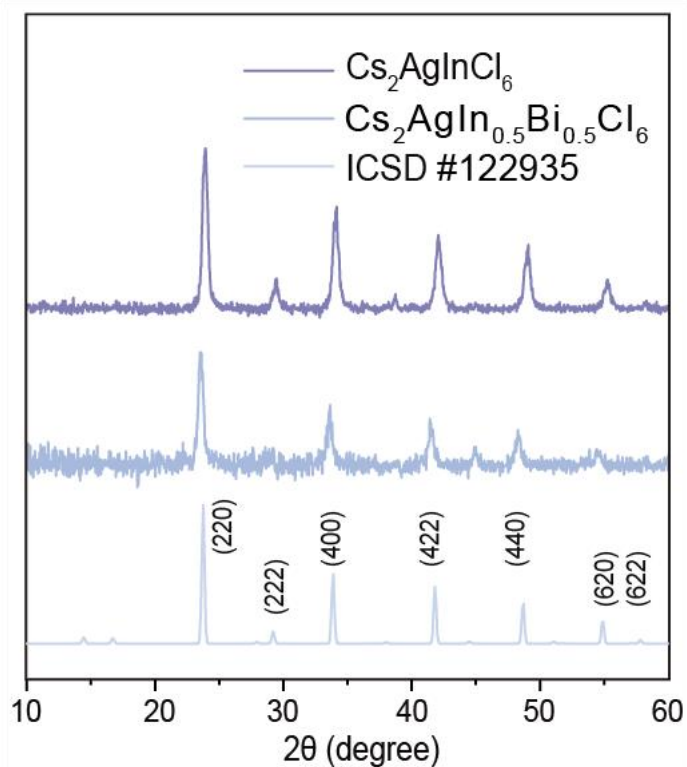


Figure 4.14 PXRD patterns of $\text{Cs}_2\text{AgBi}_{0.5}\text{In}_{0.5}\text{Cl}_6$ NCs compared to the PXRD pattern of $\text{Cs}_2\text{AgInCl}_6$ and reference patterns of $\text{Cs}_2\text{AgBi}_{0.5}\text{In}_{0.5}\text{Cl}_6$ (cubic, ICSD Coll. Code #11524)

In addition, Figure 4.15a and b shows the TEM image and size distribution of $\text{Cs}_2\text{AgBi}_{0.5}\text{In}_{0.5}\text{Cl}_6$ NCs, revealing a cubic shape with an average diameter of around 18.65 ± 2.25 nm.

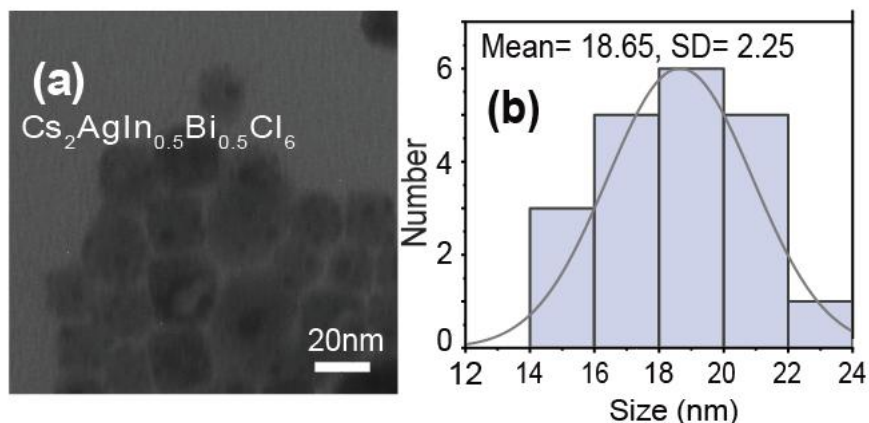


Figure 4.15 (a) TEM image of $\text{Cs}_2\text{AgBi}_{0.5}\text{In}_{0.5}\text{Cl}_6$ NCs (b) Size distribution diagram of $\text{Cs}_2\text{AgBi}_{0.5}\text{In}_{0.5}\text{Cl}_6$ NCs. The average NCs sizes and standard deviations are shown in the graph.

4.3.2 Optical and Magneto-optical properties of $\text{Cs}_2\text{AgIn}_{0.5}\text{Bi}_{0.5}\text{Cl}_6$ NCs

Figure 4.16a shows the absorption (top) and variable-field MCD (bottom) spectra of $\text{Cs}_2\text{AgBi}_{0.5}\text{In}_{0.5}\text{Br}_6$. The MCD spectra at all fields feature a pronounced peak around 372 nm, attributed to the band-edge transition. Previous reports have suggested that increase in Bi concentration does not significantly shift the absorption peak but does increase the absorption intensity.^[143] Moreover, the MCD signal shows a similar shape to that for $\text{Cs}_2\text{AgBiCl}_6$ NCs. Therefore, we speculate that the MCD signal is composed of both direct and bound excitonic transitions. The coexistence of free and self-trapped excitons in the PL emission of $\text{Cs}_2\text{AgIn}_x\text{Bi}_{1-x}\text{Cl}_6$ also have been reported.^{[81][144]}

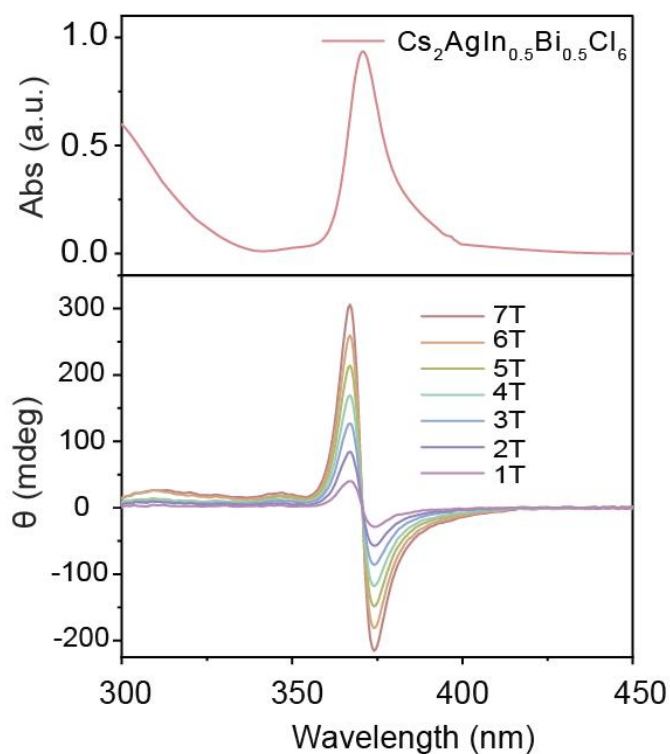


Figure 4.16 Optical absorption spectrum of $\text{Cs}_2\text{AgBi}_{0.5}\text{In}_{0.5}\text{Cl}_6$ NCs (top) and MCD spectra of $\text{Cs}_2\text{AgBi}_{0.5}\text{In}_{0.5}\text{Cl}_6$ NCs at different magnetic fields (bottom).

Figure 4.17 shows the magnetic field dependence of the MCD intensity of the deconvoluted direct band gap and bound excitonic transitions, both of which show linear behavior (also see Figure B.5 in Appendix). At 5 K and 7 T, the calculated Zeeman splitting and g factor for the direct excitonic transition are 0.32 meV and 0.79, respectively. For bound excitonic transition the Zeeman splitting and the corresponding g-value are 0.28 meV and 0.69. The decrease in these parameters compared to $\text{Cs}_2\text{AgBiCl}_6$ NCs is likely due to the conduction band of $\text{Cs}_2\text{AgInCl}_6$ being primarily composed of In 5s orbitals, which have a smaller contribution to spin-orbit coupling, thereby reducing the Zeeman splitting and g-factor under the magnetic field. Moreover, the atomic number (Z) significantly influences spin-orbit coupling. Compared to bismuth, indium has a lower atomic mass, which also reduces the spin-orbit coupling effect.^[124]

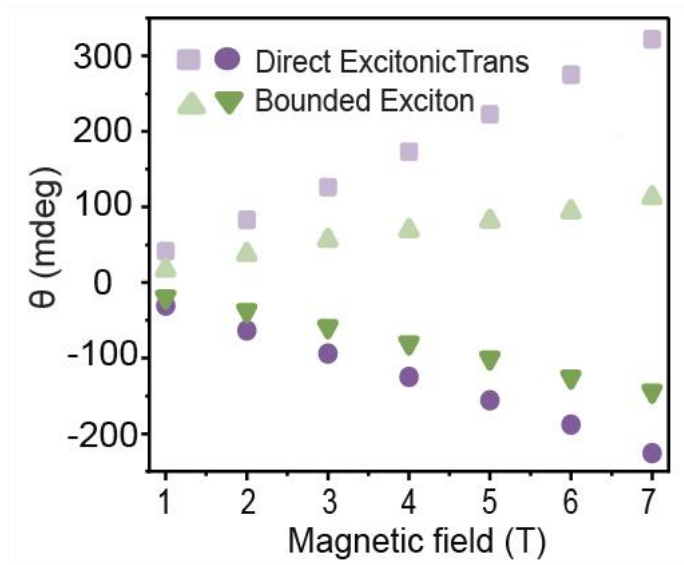


Figure 4.17 Peak intensity of direct band gap transition and bound exciton transition of $\text{Cs}_2\text{AgBi}_{0.5}\text{In}_{0.5}\text{Cl}_6$ NCs from 1 T to 7 T.

Additionally, variable-temperature MCD measurements were conducted to further verify the nature of the new band edge introduced by Bi doping. While $\text{Cs}_2\text{AgIn}_{0.5}\text{Bi}_{0.5}\text{Cl}_6$ NCs exhibits MCD signals similar to those of $\text{Cs}_2\text{AgBiCl}_6$ double perovskite, indicating that their absorption features arise from the same two component transitions, $\text{Cs}_2\text{AgIn}_{0.5}\text{Bi}_{0.5}\text{Cl}_6$ demonstrates a more pronounced temperature dependence (Figure 4.18). Therefore, similar deconvolution was applied to the MCD signals at all temperatures (Figure B.6 in Appendix B). Figure 4.18b illustrates the relative changes in the deconvoluted MCD signals at different temperatures compared to the data collected at 5 K. The deconvoluted MCD signals for both direct and bound excitonic transitions slightly increase with temperature from 5 K to 100 K. This behavior is similar to that observed for Ag-Bi double perovskite NCs and may be attributed to the reduction in the direct band gap energy.^[133] Furthermore, when the temperature exceeds 100 K, the intensities of both MCD signals decrease with increasing temperature. However, compared to bound excitonic transitions, the direct band-gap transitions exhibit more

pronounced changes. This behavior is consistent with the excitons at high temperatures, confirming our peak assignment.

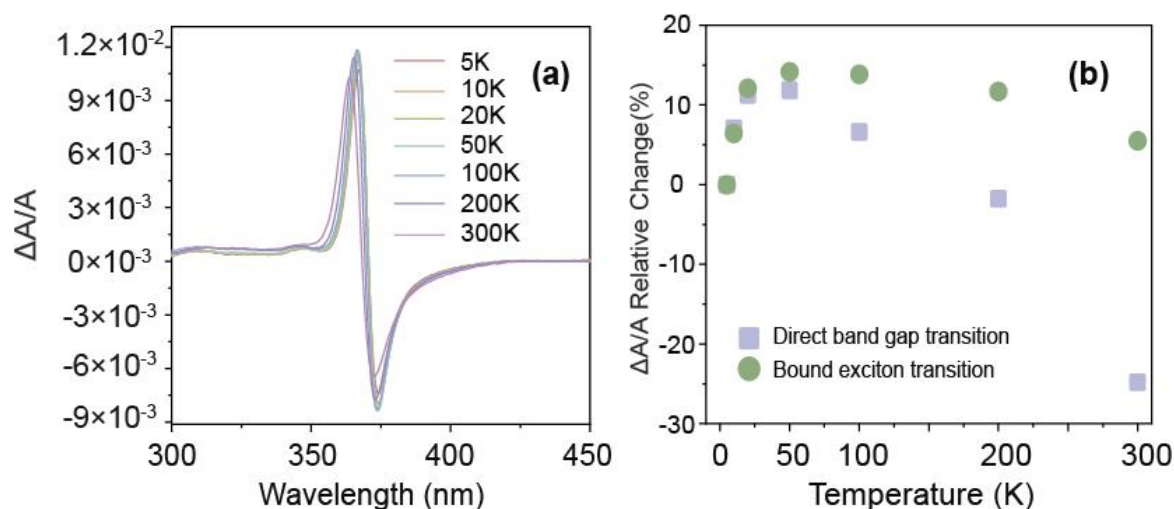


Figure 4.18 (a) Normalized 7 T field MCD spectra of Cs₂AgBi_{0.5}In_{0.5}Cl₆ NCs at temperatures ranging from 5 K to 300 K. (b) Relative change of normalized MCD signal at different temperature compared with the signal at 5 K.

4.4 Conclusion

In summary, in this chapter we investigated the electronic structure and magneto-optical properties of all-inorganic lead-free double halide perovskite NCs using MCD spectroscopy. The MCD spectra reveal the presence of two distinct derivative-shaped signals for Cs₂AgBiX₆ NCs, which were assigned to direct and bound excitonic transitions. While excitonic Zeeman splitting for these two transitions are similar in Cs₂AgBiCl₆ NCs, significantly larger Zeeman splitting is observed for bound exciton compared to direct exciton in Cs₂AgBiBr₆ NCs. We attribute this effect to the lower formation energy of Ag vacancies in Cs₂AgBiBr₆ compared to Cs₂AgBiCl₆, which is responsible for the bound exciton formation. By performing comparative MCD measurements on Cs₂AgInCl₆ and Bi³⁺-doped Cs₂AgInCl₆ NCs, we observed weak

optical transitions near the valence band minimum of the $\text{Cs}_2\text{AgInCl}_6$ material and discovered that Bi doping can effectively break the symmetry and introduce new conduction bands characteristics. Moreover, the effect of cation composition on the electronic structure of and excitonic Zeeman splitting in double halide perovskite NCs was also investigated. Larger Zeeman splitting induced by alloying Bi into $\text{Cs}_2\text{AgInCl}_6$ NCs could be associated with increased spin-orbit coupling due to the change in the electronic structure of NCs and larger atomic number of Bi compared to In. The results of this work demonstrate that lead-free halide perovskite NCs, characterized by low toxicity and tunable electronic structures and properties, exhibit significant potential as promising materials for applications in quantum technologies, including spintronics and multifunctional materials.

Chapter 5

Conclusion and Future Work

This thesis explores lead-free halide perovskite NCs as promising materials for advanced optoelectronic applications, with a particular focus on their electronic, magneto-optical, and excitonic properties. Through a comprehensive study of their magneto-optical characteristics, we aim to deepen our understanding of the potential of lead-free halide perovskites in next-generation quantum technologies, including their use in optoelectronics and spintronics. Moreover, examining these magneto-optical properties enables us to identify and optimize materials that could serve as low-toxicity alternatives to traditional lead-based perovskites, while maintaining or even enhancing the desirable optoelectronic properties essential for future applications.

The research content of this thesis is mainly distributed across two chapters. In the third chapter, we explore the electronic structure and magneto-optical properties of $\text{Cs}_3\text{Bi}_2\text{X}_9$ ($X = \text{Cl}, \text{Br}$) NCs using MCD spectroscopy. This work marks the first direct observation of exciton Zeeman splitting in these lead-free perovskites at room temperature. The results highlight the significant influence of halide composition on electronic properties; for instance, substituting Cl with Br leads to an increase in Zeeman splitting energy and g-factor. Additionally, due to the enhanced spin-orbit coupling and strong magneto-optical characteristics of $\text{Cs}_3\text{Bi}_2\text{X}_9$ NCs, they have great potential for applications in spintronics and optoelectronics. In the fourth chapter, the research extends to double perovskite nanocrystals, focusing on the two most prominent types: $\text{Cs}_2\text{AgBiX}_6$

(X = Cl, Br) and $\text{Cs}_2\text{AgInX}_6$, as well as the Bi-doped $\text{Cs}_2\text{AgInCl}_6$ NCs. Comparable MCD measurements were performed at various temperatures and magnetic fields to explore the nature of exciton transitions, as well as to determine the Zeeman splitting and g-factors in these materials. The results indicate that $\text{Cs}_2\text{AgBiBr}_6$ NCs exhibits stronger spin-orbit coupling effects and more pronounced bound exciton transitions compared to $\text{Cs}_2\text{AgBiCl}_6$ NCs, which can be attributed to the lower formation energy of silver vacancies and enhanced electron-phonon interactions. In contrast, $\text{Cs}_2\text{AgInCl}_6$ shows weaker spin-orbit coupling, resulting in reduced Zeeman splitting and g-factors. However, Bi alloying further enhances the Zeeman splitting and g-factor.

Future research could build on this foundation by exploring additional compositional variations and doping strategies to further optimize the performance of these materials. For example, we have synthesized a series of Na^+ doped $\text{Cs}_2\text{AgInCl}_6$ NCs. Na^+ doping can break the inversion symmetry of the $\text{Cs}_2\text{AgInCl}_6$ lattice, enabling radiative recombination processes that are otherwise symmetry-forbidden.^[82] Moreover, Na^+ does not contribute directly to the CBM or VBM of $\text{Cs}_2\text{AgInCl}_6$. Instead, the introduction of Na^+ forms NaCl_6 octahedra within the crystal lattice, which can act as a barrier to the spatial distribution of STEs. This confinement of STEs can further enhance the overlap between electron and hole orbitals, thereby increasing the transition dipole moment.^[81] These effects collectively lead to improved radiative efficiency and stronger emission. Notably, the PLQY of Na^+ doped $\text{Cs}_2\text{AgInCl}_6$ NCs has been shown to reach up to 86%, demonstrating the substantial impact of Na^+ doping on the optical properties of these materials.^{[82][86]} In addition to the exploration of Na^+ -doped $\text{Cs}_2\text{AgInCl}_6$, further research

on double perovskites using other B^{3+} cations, such as antimony (Sb^{3+}), presents an intriguing direction. Substituting Bi^{3+} with Sb^{3+} in double perovskites could lead to materials with distinct electronic and optical properties, including a smaller bandgap and a more dispersive band structure.^[145] Exploring additional compositional variations can help us design the electronic band structure to achieve specific desired properties, such as enhanced charge-carrier mobility, increased SOC effect, improved light absorption, and fine-tuning of the bandgap for targeted applications.^[146] Additionally, we have already initiated efforts to dope double perovskites with paramagnetic transition metal ions (Mn^{2+}) to create dilute magnetic semiconductors (DMSs). This approach opens up new possibilities for tuning the magnetic properties of these materials, potentially enhancing their suitability for spintronic applications.

In summary, these studies collectively provide significant insights into the magneto-optical and electronic properties of lead-free halide perovskite NCs, highlighting their potential as viable alternatives to lead-based perovskites. Moreover, they pave the way for the development of high-performance, environmentally friendly materials for next-generation technological applications. The ability to customize desired properties through compositional adjustments makes these materials strong candidates for a wide range of applications, including spintronics, photovoltaics, optoelectronics, and quantum information technology.

References

- [1] Tandon, B., & Radovanovic, P. V. Size Control of the Mechanism of Exciton Polarization in Metal Oxide Nanocrystals through Fermi Level Pinning. *ACS Nano*, **2023**, *17*, 14069–14078.
- [2] Smith, A. M., & Nie, S. Semiconductor Nanocrystals: Structure, Properties, and Band Gap Engineering. *Acc. Chem. Res.* **2010**, *43*, 190–200.
- [3] Grundmann, M. Chapter 7. In *The Physics of Semiconductors*. Springer: Berlin, 2006; pp. 185–211.
- [4] National Council of Educational Research and Training (NCERT). *Physics Part-II*, 2020; NCERT: New Delhi. <https://ncert.nic.in/textbook/pdf/leph206.pdf> (accessed 2024-07-03).
- [5] Hummel, R. E. Quantum Mechanical Treatment of the Optical Properties. In *Electronic Properties of Materials*. Springer: New York, U.S, 2011; pp. 247–257
- [6] Grundmann, M. *The Physics of Semiconductors An Introduction Including Nanophysics and Applications*, 3rd ed. Springer International Publishing: Cham, Switzerland., 2016; pp. 268–298.
- [7] Lin, C.-Y.; Lu, Z. *Selection Rules and Transition Moment Integral*. Chemistry LibreTexts. [https://chem.libretexts.org/Bookshelves/Physical_and_Theoretical_Chemistry_Textbook_Maps/Supplemental_Modules_\(Physical_and_Theoretical_Chemistry\)/Spectroscopy/Fundamentals_of_Spectroscopy/Selection_rules_and_transition_moment_integral](https://chem.libretexts.org/Bookshelves/Physical_and_Theoretical_Chemistry_Textbook_Maps/Supplemental_Modules_(Physical_and_Theoretical_Chemistry)/Spectroscopy/Fundamentals_of_Spectroscopy/Selection_rules_and_transition_moment_integral) (accessed 2024-08-15).
- [8] Basu, P. K.; Mukhopadhyay, B.; Basu, R. Basic Properties of Semiconductors. In

- Semiconductor Nanophotonics*. Oxford University Press: Oxford, U.K, 2022; pp. 22-61.
- [9] Basu, P. K.; Mukhopadhyay, B.; Basu, R. Excitons in Semiconductors. In *Semiconductor Nanophotonics*. Oxford University Press: Oxford, U.K, 2022, pp. 177-225
- [10] Kéna-Cohen, S. *Strong Exciton-Photon Coupling in Organic Semiconductor Microcavities*; Ph.D. Dissertation, Princeton University, Princeton, NJ, 2010.
- [11] Hummel, R. E. Chapter 20. In *Electronic Properties of Materials*, 4th ed. Springer: New York, U.S, 2011; pp 421–426.
- [12] Pelant, I.; Valenta, J. Phonons and Their Participation in Optical Phenomena. In *Luminescence Spectroscopy of Semiconductors*. Oxford University Press: Oxford, U.K., 2012; pp. 98-122
- [13] Grundmann, M. Chapter 10. In *The Physics of Semiconductors*. Springer: Berlin, 2006; pp. 309–343.
- [14] Wu, Y., Li, F., Wu, Y., Wang, H., Gu, L., Zhang, J., Qi, Y., Meng, L., Kong, N., Chai, Y., Hu, Q., Xing, Z., Ren, W., Li, F., & Zhu, X. Lanthanide luminescence nanothermometer with working wavelength beyond 1500 nm for cerebrovascular temperature imaging in vivo. *Nat. Commun.* **2024**, *15*, 2341–2341.
- [15] Chen, W.; & Cao, D. Luminescence Nanomaterials and Applications. *Nanomater.* **2023**, *13*, 1047.
- [16] Chang, S., Koo, J. H., Yoo, J., Kim, M. S., Choi, M. K., Kim, D.-H., & Song, Y. M. Flexible and Stretchable Light-Emitting Diodes and Photodetectors for Human-Centric Optoelectronics. *Chem. Rev.* **2024**, *124*, 768–859.

- [17] Quan, L. N., Rand, B. P., Friend, R. H., Mhaisalkar, S. G., Lee, T.-W., & Sargent, E. H. perovskites for Next-Generation Optical Sources. *Chem. Rev.* **2019**, *119*, 7444–7477.
- [18] Muscarella, L. A., & Hutter, E. M. Halide Double-Perovskite Semiconductors beyond Photovoltaics. *ACS Energy Lett.* **2022**, *7*, 2128–2135.
- [19] Mathan Kumar, P., Das, A., Seban, L., & Nair, R. G. Fabrication and Life Time of Perovskite Solar Cells. In *Perovskite Photovoltaics*. Elsevier: United States, 2018, pp. 231–287.
- [20] Jena, A. K., Kulkarni, A., & Miyasaka, T. Halide Perovskite Photovoltaics: Background, Status, and Future Prospects. *Chem. Rev.* **2019**, *119*, 3036–3103.
- [21] Helmholtz-Zentrum Berlin. Perovskite Solar Cells.
https://www.helmholtz-berlin.de/forschung/oe/se/silizium-photovoltaik/arbeitsgebiet/e/perowskite/index_en.html (accessed 2024-07-24).
- [22] Zhang, F.; Shi, W.; Wang, Y.; Li, Y.; Yuan, Y.; Gao, Y.; Zeng, X.; Sun, J. Phase Stabilization of Cesium Lead Iodide perovskites for Use in Efficient Optoelectronic Devices. *ACS Energy Lett.* **2020**, *5*, 1823–1830.
- [23] Deng, J., Li, J., Yang, Z., & Wang, M. All-inorganic lead halide perovskites: a promising choice for photovoltaics and detectors. *J. Mater. Chem. C* **2019**, *7*, 12415–1244.
- [24] Dey, A.; Ye, J.; De, A.; Debroye, E.; Ha, S. K.; Bladt, E.; Kshirsagar, A. S.; Wang, Z.; Yin, J.; Wang, Y.; Quan, L. N.; Yan, F.; Gao, M.; Li, X.; Shamsi, J.; Debnath, T.; Cao, M.; Scheel, M. A.; Kumar, S.; Steele, J. A.; Gerhard, M.; Chouhan, L.; Xu, K.; Wu, X.; Li, Y.; Zhang, Y.; Dutta, A.; Han, C.; Vincon, I.; Rogach, A. L.; Nag, A.; Samanta, A.; Korgel, B. A.; Shih, C.-J.; Gamelin, D. R.; Son, D. H.; Zeng, H.; Zhong, H.; Sun,

- H.; Demir, H. V.; Scheblykin, I. G.; Mora-Seró, I.; Stolarczyk, J. K.; Zhang, J. Z.; Feldmann, J.; Hofkens, J.; Luther, J. M.; Pérez-Prieto, J.; Li, L.; Manna, L.; Bodnarchuk, M. I.; Kovalenko, M. V.; Roeffaers, M. B. J.; Pradhan, N.; Mohammed, O. F.; Bakr, O. M.; Yang, P.; Müller-Buschbaum, P.; Kamat, P. V.; Bao, Q.; Zhang, Q.; Krahne, R.; Galian, R. E.; Stranks, S. D.; Bals, S.; Biju, V.; Tisdale, W. A.; Yan, Y.; Hoye, R. L. Z.; Polavarapu, L. State of the Art and Prospects for Halide Perovskite Nanocrystals. *ACS Nano*. **2021**, *15*, 10775–10981.
- [25] Simenas, M., Gagor, A., Banys, J., & Maczka, M. Phase Transitions and Dynamics in Mixed Three- and Low-Dimensional Lead Halide Perovskites. *Chem. Rev.* **2024**, *124*, 2281–2326.
- [26] Zhou, Y., Chen, J., Bakr, O. M., & Mohammed, O. F. Metal Halide perovskites for X-ray Imaging Scintillators and Detectors. *ACS Energy Lett.* **2021**, *6*, 739–768.
- [27] Kim, J. Y., Lee, J.-W., Jung, H. S., Shin, H., & Park, N.-G. High-Efficiency Perovskite Solar Cells. *Chem. Rev.* **2020**, *120*, 7867–7918.
- [28] Park, Y., & Lee, J.-S. Metal Halide Perovskite-Based Memristors for Emerging Memory Applications. *J. Phys. Chem. Lett.* **2022** *13*, 5638–5647.
- [29] Chen Q., Wu J., Ou X., Huang B., Almutlaq J., Zhumekenov AA., Guan X., Han S., Liang L., Yi Z., Li J., Xie X., Wang Y., Li Y., Fan D., Teh DBL., Mohammed OF., Bakr OM., Wu T., Bettinelli M., Yang H., Huang W., Liu X. All-inorganic perovskite nanocrystal scintillators. *Nature*. **2018**, *561*, 88–93.
- [30] Cao, Y. B., Zhang, D., Zhang, Q., Qiu, X., Zhou, Y., Poddar, S., Fu, Y., Zhu, Y., Liao, J.-F., Shu, L., Ren, B., Ding, Y., Han, B., He, Z., Kuang, D.-B., Wang, K., Zeng, H., & Fan, Z. High-efficiency, flexible and large-area red/green/blue all-inorganic metal halide perovskite quantum wires-based light-emitting diodes. *Nat. Commun.* **2023**, *14*, 4611–4611.

- [31] Bao, C., Yang, J., Bai, S., Xu, W., Yan, Z., Xu, Q., Liu, J., Zhang, W., & Gao, F. High Performance and Stable All-Inorganic Metal Halide Perovskite-Based Photodetectors for Optical Communication Applications. *Adv. Mater.* **2018**, *30*, e1803422.
- [32] Lei, L., Dong, Q., Gundogdu, K., & So, F. Metal Halide perovskites for Laser Applications. *Adv. Funct. Mater.* **2021**, *31*, 2010144.
- [33] Proescu, L., Yakunin, S., Bodnarchuk, M. I., Krieg, F., Caputo, R., Hendon, C. H., Yang, R. X., Walsh, A., & Kovalenko, M. V. Nanocrystals of Cesium Lead Halide perovskites (CsPbX_3 , X = Cl, Br, and I): Novel Optoelectronic Materials Showing Bright Emission with Wide Color Gamut. *Nano Lett.* **2015**, *15*, 3692–3696.
- [34] Ahmad, M., Rehman, G., Ali, L., Shafiq, M., Iqbal, R., Ahmad, R., Khan, T., Jalali-Asadabadi, S., Maqbool, M., & Ahmad, I. Structural, electronic and optical properties of CsPbX_3 (X=Cl, Br, I) for energy storage and hybrid solar cell applications. *J. Alloys Compd.* **2017**, *705*, 828–839.
- [35] Yettapu, G. R., Talukdar, D., Sarkar, S., Swarnkar, A., Nag, A., Ghosh, P., & Mandal, P. Terahertz Conductivity within Colloidal CsPbBr_3 Perovskite Nanocrystals: Remarkably High Carrier Mobilities and Large Diffusion Lengths. *Nano Lett.* **2016**, *16*, 4838–4848.
- [36] Yumoto, G., Hirori, H., Sekiguchi, F. et al. Strong spin-orbit coupling inducing Autler-Townes effect in lead halide perovskite nanocrystals. *Nat Commun.* **2021**, *12*, 3026.
- [37] Niu, G., Guo, X., & Wang, L. Review of recent progress in chemical stability of perovskite solar cells. *J. Mater. Chem. A* **2015**, *3*, 897–898.
- [38] Sato, H., Ishii, C., Nakayama, S. M. M., Ichise, T., Saito, K., Watanabe, Y., Ogasawara, K., Torimoto, R., Kobayashi, A., Kimura, T., Nakamura, Y., Yamagishi,

- J., Ikenaka, Y., & Ishizuka, M. Behavior and toxic effects of Pb in a waterfowl model with oral exposure to Pb shots: Investigating Pb exposure in wild birds. *Environ. Pollut.* **2022**, *308*, 119580–119580.
- [39] López-Fernández, I.; Valli, D.; Wang, C.; Samanta, S.; Okamoto, T.; Huang, Y.; Sun, K.; Liu, Y.; Chirvony, V. S.; Patra, A.; Zito, J.; De Trizio, L.; Gaur, D.; Sun, H.; Xia, Z.; Li, X.; Zeng, H.; Mora-Seró, I.; Pradhan, N.; Polavarapu, L. Lead-Free Halide Perovskite Materials and Optoelectronic Devices: Progress and Prospective. *Adv. Funct. Mater.* **2024**, *34*.
- [40] Obada, D. O., Abolade, S. A., Akinpelu, S. B., Kumar R, S., Ukpong, A. M., & Akande, A. The role of spin-orbit coupling on the optical and thermoelectric properties of pristine and defective CsSnCl₃. *Mater. Sci. Semicond. Process.* **2024**, *178*, 108372.
- [41] Kale, A. J., Pal, B., & Dixit, A. Theoretical Insights on Pb-Free Rhombohedral CsGeI₃ over Cubic CsMX₃ (M-: Pb, Sn, Ge, and X-: Cl, Br, I) Perovskite-Based Single-Junction Solar Cell with Efficiency > 30%. *Phys. Status Solidi A* **2024**, 2300464.
- [42] Volonakis, G., Filip, M. R., Haghighirad, A. A., Sakai, N., Wenger, B., Snaith, H. J., & Giustino, F. Lead-Free Halide Double perovskites via Heterovalent Substitution of Noble Metals. *J. Phys. Chem. Lett.* **2016**, *7*, 1254–1259.
- [43] Chakraborty, S., Xie, W., Mathews, N., Sherburne, M., Ahuja, R., Asta, M., & Mhaisalkar, S. G. Rational Design: A High-Throughput Computational Screening and Experimental Validation Methodology for Lead-Free and Emergent Hybrid perovskites. *ACS Energy Lett.* **2017**, *2*, 837–845.

- [44] Wang, M., Wang, W., Ma, B., Shen, W., Liu, L., Cao, K., Chen, S., & Huang, W. Lead-Free Perovskite Materials for Solar Cells. *Nano-Micro Lett.* **2021**, *13*, 62–62.
- [45] Bass, K. K., Estergreen, L., Savory, C. N., Buckeridge, J., Scanlon, D. O., Djurovich, P. I., Bradforth, S. E., Thompson, M. E., & Melot, B. C. Vibronic Structure in Room Temperature Photoluminescence of the Halide Perovskite Cs₃Bi₂Br₉. *Inorg. Chem.* **2017**, *56*, 42–45.
- [46] Aleksandrova, I., Burriel, R., Bartolome, J., Bagautdinov, B., Blasco, J., Sukhovskiy, A., Torres, J., Vasiljev, A., & Solovjev, L. Low-temperature phase transitions in the trigonal modification of Cs₃Bi₂Br₉ and Cs₃Sb₂I₉. *Ph. Transit.* **2002**, *75*, 607–620.
- [47] Creutz, S. E.; Liu, H.; Kaiser, M. E.; Li, X.; Gamelin, D. R. Structural Diversity in Cesium Bismuth Halide Nanocrystals. *Chem. Mater.* **2019**, *31*, 4685–4697.
- [48] Liu, J., Hu, Q., Yu, H., Xu, H., Yu, J., Han, Q., & Wu, W. Structural Transformation and Photoluminescent Property of Manganese-Doped Bismuth-Based perovskites. *Inorg. Chem.* **2023**, *62*, 9111–9119.
- [49] Ravi, V. K., Markad, G. B., & Nag, A. Band Edge Energies and Excitonic Transition Probabilities of Colloidal CsPbX₃ (X = Cl, Br, I) Perovskite Nanocrystals. *ACS Energy Lett.* **2016**, *1*, 665–671.
- [50] Yang, B., Chen, J., Hong, F., Mao, X., Zheng, K., Yang, S., Li, Y., Pullerits, T., Deng, W., & Han, K. Lead-Free, Air-Stable All-Inorganic Cesium Bismuth Halide Perovskite Nanocrystals. *Angew. Chem. Int. Ed.* **2017**, *56*, 12471–12475.
- [51] Leng, M., Yang, Y., Zeng, K., Chen, Z., Tan, Z., Li, S., Li, J., Xu, B., Li, D., Hautzinger, M. P., Fu, Y., Zhai, T., Xu, L., Niu, G., Jin, S., & Tang, J. All-Inorganic Bismuth-Based Perovskite Quantum Dots with Bright Blue Photoluminescence and Excellent Stability. *Adv. Funct. Mater.* **2018**, *28*, 1704446.

- [52] Luo, T., & Wei, J. First principles study of electronic and optical properties of inorganic and lead-free perovskite: Cs₃Bi₂X₉ (X: Cl, Br, I). *Mater. Chem. Phys.* **2020**, 253, 123374.
- [53] Ji, Y., She, M., Bai, X., Liu, E., Xue, W., Zhang, Z., Wan, K., Liu, P., Zhang, S., & Li, J. In-Depth Understanding of the Effect of Halogen-Induced Stable 2D Bismuth-Based perovskites for Photocatalytic Hydrogen Evolution Activity. *Adv. Funct. Mater.* **2022**, 32.
- [54] Lei, B., Cui, W., Sheng, J., Zhong, F., & Dong, F. Halogen-Site Regulation in Cs₃Bi₂X₉ Quantum Dots for Efficient and Selective Oxidation of Benzyl Alcohol Driven by Solar Light. *Small.* **2024**, 20, e2308088.
- [55] Xu, W.-L., Hu, J., Yang, Q., Lian, Y., Zheng, M., & Du, E. Charge transfer dynamics in C₃N₄ encapsulated Cs₃Bi₂Br₉ nanocrystals heterojunction for photocatalytic application. *J. Alloys Compd.* **2024**, 988.
- [56] Kim, M. K., Cha, J., Jin, H., & Kim, M. Facile synthesis of Cs₃Bi₂Br₉ perovskite nanopla with low-polarity antisolvents for photodetection applications. *Mater. Lett.* **2023**, 333, 133577.
- [57] Ghosh, S., Mukhopadhyay, S., Paul, S., Pradhan, B., & De, S. K. Control Synthesis and Alloying of Ambient Stable Pb-Free Cs₃Bi₂Br_{9(1-x)}I_{9x} (0 ≤ x ≤ 1) Perovskite Nanocrystals for Photodetector Application. *ACS Applied Nano Mater.* **2020**, 3, 11107–11117.
- [58] Yan, J., Zhang, S., Wei, Q., Cao, S., Zhao, J., Zou, B., & Zeng, R. Stoichiometry-Controlled Phase Engineering of Cesium Bismuth Halides and Reversible Structure Switch. *Adv. Opt. Mater.* **2022**, 10.

- [59] Zhao, C., Gao, Y., Zhou, D., Zhu, F., Chen, J., & Qiu, J. High-efficiency dual-mode luminescence of metal halide perovskite $\text{Cs}_3\text{Bi}_2\text{Cl}_9:\text{Er}^{3+}$ and its use in optical temperature measurement with high sensitivity. *J. Alloys Compd.* **2023**, *944*, 169134.
- [60] Usman, M., & Yan, Q. Recent advancements in crystalline Pb-free halide double perovskites. *Crystals.* **2020**, *10*, 62.
- [61] Bartel, C. J., Sutton, C., Goldsmith, B. R., Ouyang, R., Musgrave, C. B., Ghiringhelli, L. M., & Scheffler, M. New tolerance factor to predict the stability of perovskite oxides and halides. *Sci. Adv.* **2019**, *5*, eaav0693.
- [62] Zhang, Z., Zhang, Y., Guo, X., Wang, D., Lao, Y., Qu, B., Xiao, L., & Chen, Z. Realizing High-Efficiency and Stable Perovskite Solar Cells via Double-Perovskite Nanocrystal Passivation. *ACS Appl. Energy Mater.* **2022**, *5*, 1169–1174.
- [63] Han, P., & Han, K. Recent Advances in All-Inorganic Lead-Free Three-Dimensional Halide Double Perovskite Nanocrystals. *Energy & Fuels*, **2021**, *35*, 18871–18887.
- [64] Tailor, N. K., Listorti, A., Colella, S., & Satapathi, S. Lead-Free Halide Double perovskites: Fundamentals, Challenges, and Photovoltaics Applications. *Adv. Mater. Technol.* **2023**, *8*, 2200442.
- [65] Chrafi, Y., Al-Hattab, M., & Rahmani, K. Thermodynamic, optical, and morphological studies of the $\text{Cs}_2\text{AgInX}_6$ double perovskites ($X = \text{Cl}, \text{Br}, \text{and I}$): Insights from DFT study. *J. Alloys Compd.* **2023**, *960*, 170650.
- [66] Filip, M. R., Hillman, S., Haghghirad, A. A., Snaith, H. J., & Giustino, F. Band Gaps of the Lead-Free Halide Double perovskites $\text{Cs}_2\text{AgBiCl}_6$ and $\text{Cs}_2\text{AgBiBr}_6$ from Theory and Experiment. *J. Phys. Chem. Lett.* **2016**, *7*, 2579–2585.

- [67] Yang, B., Chen, J., Yang, S., Hong, F., Sun, L., Han, P., Pullerits, T., Deng, W., & Han, K. Lead-Free Silver-Bismuth Halide Double Perovskite Nanocrystals. *Angew. Chem., Int. Ed.* **2018**, *57*, 5359–5363.
- [68] Zelewski, S. J., Urban, J. M., Surrente, A., Maude, D. K., Kuc, A., Schade, L., Johnson, R. D., Dollmann, M., Nayak, P. K., Snaith, H. J., Radaelli, P., Kudrawiec, R., Nicholas, R. J., Plochocka, P., & Baranowski, M. Revealing the nature of photoluminescence emission in the metal-halide double perovskite Cs₂AgBiBr₆. *J. Mater. Chem. C* **2019**, *7*, 835–8356.
- [69] Steele, J. A., Puech, P., Keshavarz, M., Yang, R., Banerjee, S., Debroye, E., Kim, C. W., Yuan, H., Heo, N. H., Vanacken, J., Walsh, A., Hofkens, J., & Roeffaers, M. B. J. Giant Electron–Phonon Coupling and Deep Conduction Band Resonance in Metal Halide Double Perovskite. *ACS Nano*. **2018**, *12*, 8081–8090.
- [70] Zhang, Z., Sun, Q., Lu, Y., Lu, F., Mu, X., Wei, S.-H., & Sui, M. Hydrogenated Cs₂AgBiBr₆ for significantly improved efficiency of lead-free inorganic double perovskite solar cell. *Nat. Commun.* **2022**, *13*, 3397–3397.
- [71] McClure, E. T., Ball, M. R., Windl, W., & Woodward, P. M. Cs₂AgBiX₆ (X = Br, Cl): New Visible Light Absorbing, Lead-Free Halide Perovskite Semiconductors. *Chem. Mater.* **2016**, *28*, 1348–1354.
- [72] Abiram, G., Gourji, F. H., Pitchaiya, S., Ravirajan, P., Murugathas, T., & Velauthapillai, D. Air processed Cs₂AgBiBr₆ lead-free double perovskite high-mobility thin-film field-effect transistors. *Sci. Rep.* **2022**, *12*, 2455–2455.

- [73] Slavney, A. H., Hu, T., Lindenberg, A. M., & Karunadasa, H. I. A Bismuth-Halide Double Perovskite with Long Carrier Recombination Lifetime for Photovoltaic Applications. *J. Am. Chem. Soc.* **2016**, *138*, 2138–2141.
- [74] Zhou, L., Xu, Y., Chen, B., Kuang, D., & Su, C. Synthesis and Photocatalytic Application of Stable Lead-Free Cs₂AgBiBr₆ Perovskite Nanocrystals. *Small.* **2018**, *14*, 1703762.
- [75] Wu, D., Tao, Y., Huang, Y., Huo, B., Zhao, X., Yang, J., Jiang, X., Huang, Q., Dong, F., & Tang, X. High visible-light photocatalytic performance of stable lead-free Cs₂AgBiBr₆ double perovskite nanocrystals. *J. Catal.* **2021**, *397*, 27–35.
- [76] Fang, F., Li, H., Fang, S., Zhou, B., Huang, F., Ma, C., Wan, Y., Jiang, S., Wang, Y., Tian, B., & Shi, Y. 2D Cs₂AgBiBr₆ with Boosted Light–Matter Interaction for High-Performance Photodetectors. *Adv. Opt. Mater.* **2021**, *9*, 2001930.
- [77] Yang, B., Pan, W., Wu, H., Niu, G., Yuan, J.-H., Xue, K.-H., Yin, L., Du, X., Miao, X.-S., Yang, X., Xie, Q., & Tang, J. Heteroepitaxial passivation of Cs₂AgBiBr₆ wafers with suppressed ionic migration for X-ray imaging. *Nat. Commun.* **2019**, *10*, 1989–1989.
- [78] Zhou, J., Xia, Z., Molochev, M. S., Zhang, X., Peng, D., & Liu, Q. Composition design, optical gap and stability investigations of lead-free halide double perovskite Cs₂AgInCl₆. *J. Mater. Chem. A* **2017**, *5*, 15031–15037.
- [79] Meng, W., Wang, X., Xiao, Z., Wang, J., Mitzi, D. B., & Yan, Y. Parity-Forbidden Transitions and Their Impact on the Optical Absorption Properties of Lead-Free Metal Halide perovskites and Double perovskites. *J. Phys. Chem. Lett.* **2017**, *8*, 2999–3007

- [80] Luo, J., Li, S., Wu, H., Zhou, Y., Li, Y., Liu, J., Li, J., Li, K., Yi, F., Niu, G., & Tang, J. Cs₂AgInCl₆ Double Perovskite Single Crystals: Parity Forbidden Transitions and Their Application For Sensitive and Fast UV Photodetectors. *ACS Photonics*. **2018**, *5*, 398–405.
- [81] Locardi, F., Cirignano, M., Baranov, D., Dang, Z., Prato, M., Drago, F., Ferretti, M., Pinchetti, V., Fanciulli, M., Brovelli, S., De Trizio, L., & Manna, L. Colloidal Synthesis of Double Perovskite Cs₂AgInCl₆ and Mn-Doped Cs₂AgInCl₆ Nanocrystals. *J. Am. Chem. Soc.* **2018**, *140*, 12989–12995.
- [82] Luo, J., Wang, X., Li, S., Liu, J., Guo, Y., Niu, G., Yao, L., Fu, Y., Gao, L., Dong, Q., Zhao, C., Leng, M., Ma, F., Liang, W., Wang, L., Jin, S., Han, J., Zhang, L., Etheridge, J., Tang, J. Efficient and stable emission of warm-white light from lead-free halide double perovskites. *Nature*. **2018**, *563*, 541–545.
- [83] Liu, Y., Jing, Y., Zhao, J., Liu, Q., & Xia, Z. Design Optimization of Lead-Free Perovskite Cs₂AgInCl₆:Bi Nanocrystals with 11.4% Photoluminescence Quantum Yield. *Chem. Mater.* **2019**, *31*, 3333–3339.
- [84] Tran, T. T., Panella, J. R., Chamorro, J. R., Morey, J. R., & McQueen, T. M. Designing indirect-direct bandgap transitions in double perovskites. *Mater. Horiz.* **2017**, *4*, 688–693.
- [85] Tang, H., Xu, Y., Hu, X., Hu, Q., Chen, T., Jiang, W., Wang, L., & Jiang, W. Facile one-pot preparation and luminescence mechanism of stable Bi³⁺-doped Cs₂AgInCl₆ double perovskite nanocrystals. **2022**, *J. Lumin.* *252*, 119246.
- [86] Wang, H., Chen, J., Sun, Y., Wang, F., Yang, J., Zhang, C., Kong, J., & Li, L. Lead-free Cs₂Ag_{1-x}Na_xIn_{1-y}Bi_yCl₆ perovskite films with broad warm-yellow emission for lighting applications. *Sci. Rep.* **2024**, *14*, 14740–14.

- [87] Hirohata, A., Yamada, K., Nakatani, Y., Prejbeanu, I.-L., Diény, B., Pirro, P., & Hillebrands, B. Review on spintronics: Principles and device applications. *J. Magn. Mater.* **2020**, *509*, 166711.
- [88] Ennen, I., Kappe, D., Rempel, T., Glenske, C., & Hütten, A. Giant Magnetoresistance: Basic concepts, microstructure, magnetic interactions and applications. *Sensors*. **2016**, *16*, 904.
- [89] Kao, S.-C., Lin, C.-Y., Liao, W.-B., Wang, P.-C., Hu, C.-Y., Huang, Y.-H., Liu, Y.-T., & Pai, C.-F. Field-free magnetization switching through modulation of zero-field spin-orbit torque efficacy. *APL Mater.* **2023**, *11*, 111104–111108.
- [90] Cubells-Beltrán, M. D., Reig, C., Madrenas, J., De Marcellis, A., Santos, J., Cardoso, S., & Freitas, P. P. Integration of GMR sensors with different technologies. *Sensors*. **2016**, *16*, 939.
- [91] Hegde, M., Farvid, S. S., Hosein, I. D., & Radovanovic, P. V. Tuning Manganese Dopant Spin Interactions in Single GaN Nanowires at Room Temperature. *ACS Nano*. **2011**, *5*, 6365–6373.
- [92] Farvid, S. S., Hegde, M., Hosein, I. D., & Radovanovic, P. V. Electronic structure and magnetism of Mn dopants in GaN nanowires: Ensemble vs single nanowire measurements. *Appl. Phys. Lett.* **2011**, *99*, 222504.
- [93] Tanaka, M. Recent progress in ferromagnetic semiconductors and spintronics devices. *Jpn. J. Appl. Phys.* **2021**, *60*, 10101.
- [94] Telegin, A., & Sukhorukov, Y. Magnetic Semiconductors as Materials for Spintronics. *Magnetochemistry*, **2022**, *8*, 173.

- [95] Spaldin, N. A. *Magnetic Materials: Fundamentals and Applications*, 2nd ed. Cambridge University Press: Cambridge, 2011.
- [96] Winkler, R. *Spin-Orbit Coupling Effects in Two-Dimensional Electron and Hole Systems*; Springer: **2003**.
- [97] Yumoto, G.; Hirori, H.; Sekiguchi, F.; Adachi, S.; Yoshimoto, S.; Tanaka, K. Strong spin-orbit coupling inducing Autler-Townes effect in lead halide perovskite nanocrystals. *Nat. Commun.* **2021**, *12*, 3026.
- [98] Yeh, I.-H., Ghobadifard, M., Feng, L., Galievsky, V., & Radovanovic, P. V. Origin of Dopant-Carrier Exchange Coupling and Excitonic Zeeman Splitting in Mn²⁺-Doped Lead Halide Perovskite Nanocrystals. *Nano Lett.* **2024**, *24*, 10554–10561.
- [99] Belykh, V. V., Yakovlev, D. R., Glazov, M. M., Grigoryev, P. S., Hussain, M., Rautert, J., Dirin, D. N., Kovalenko, M. V., & Bayer, M. Coherent spin dynamics of electrons and holes in CsPbBr₃ perovskite crystals. *Nat. Commun.* **2019**, *10*, 673–673.
- [100] Xu, J., Li, K., Huynh, U. N., Fadel, M., Huang, J., Sundararaman, R., Vardeny, V., & Ping, Y. How spin relaxes and dephases in bulk halide perovskites. *Nat. Commun.* **2024**, *15*, 188–188.
- [101] Kirstein, E., Kopteva, N. E., Yakovlev, D. R., Zhukov, E. A., Kolobkova, E. V., Kuznetsova, M. S., Belykh, V. V., Yugova, I. A., Glazov, M. M., Bayer, M., & Greilich, A. Mode locking of hole spin coherences in CsPb(Cl, Br)₃ perovskite nanocrystals. *Nat. Commun.* **2023**, *14*, 699–699.
- [102] Giovanni, D., Ma, H., Chua, J., Grätzel, M., Ramesh, R., Mhaisalkar, S., Mathews, N., & Sum, T. C. Highly Spin-Polarized Carrier Dynamics and Ultralarge Photoinduced Magnetization in CH₃NH₃PbI₃ Perovskite Thin Films. *Nano Lett.* **2015**, *15*, 1553–1558.

- [103] Kim, Y. H., Zhai, Y., Lu, H., Pan, X., Xiao, C., Gauldin, E. A., Harvey, S. P., Berry, J. J., Vardeny, Z. V., Luther, J. M., & Beard, M. C. Chiral-induced spin selectivity enables a room-temperature spin light-emitting diode. *Science*. **2021**, *371*, 1129–1133.
- [104] Jana, M. K., Song, R., Liu, H., Khanal, D. R., Janke, S. M., Zhao, R., Liu, C., Valy Vardeny, Z., Blum, V., & Mitzi, D. B. Organic-to-inorganic structural chirality transfer in a 2D hybrid perovskite and impact on Rashba-Dresselhaus spin-orbit coupling. *Nat. Commun.* **2020**, *11*, 4699–4699.
- [105] Zhang, L., Jiang, J., Multunas, C., Ming, C., Chen, Z., Hu, Y., Lu, Z., Pendse, S., Jia, R., Chandra, M., Sun, Y. Y., Lu, T. M., Ping, Y., Sundararaman, R., & Shi, J. Room-temperature electrically switchable spin–valley coupling in a van der Waals ferroelectric halide perovskite with persistent spin helix. *Nature Photonics*. **2022**, *16*, 529–537.
- [106] Spencer, M. S., Fu, Y., Schlaus, A. P., Hwang, D., Dai, Y., Smith, M. D., Gamelin, D. R., & Zhu, X. Y. Spin-orbit–coupled exciton-polariton condensates in lead halide perovskites. *Sci. Adv.* **2021**, *7*, eabj7667.
- [107] Wang, J., Zhang, C., Liu, H., McLaughlin, R., Zhai, Y., Vardeny, S. R., Liu, X., McGill, S., Semenov, D., Guo, H., Tsuchikawa, R., Deshpande, V. V., Sun, D., & Vardeny, Z. V. Spin-optoelectronic devices based on hybrid organic-inorganic trihalide perovskites. *Nat. Commun.* **2019**, *10*, 129–129.
- [108] Chen, J., Wu, K., Hu, W., & Yang, J. Tunable Rashba Spin Splitting in Two-Dimensional Polar perovskites. *J. Phys. Chem. Lett.* **2019**, *12*, 1932–1939.
- [109] Volonakis, G., Filip, M. R., Haghghirad, A. A., Sakai, N., Wenger, B., Snaith, H. J., & Giustino, F. Lead-Free Halide Double perovskites via Heterovalent Substitution of Noble Metals. *J. Phys. Chem. Lett.* **2016**, *7*, 1254–1259.

- [110] Mason, W. R. *A Practical Guide to Magnetic Circular Dichroism Spectroscopy*; John Wiley & Sons: Hoboken, NJ, 2007.
- [111] Han, B., Gao, X., Lv, J., & Tang, Z. Magnetic Circular Dichroism in Nanomaterials: New Opportunity in Understanding and Modulation of Excitonic and Plasmonic Resonances. *Adv. Mater.* **2020**, *32*, e1801491.
- [112] Ma, S., Yuan, G., Zhang, Y., Yang, N., Li, Y., & Chen, Q. Development of encapsulation strategies towards the commercialization of perovskite solar cells. *Energy Environ. Sci.* **2021**, *15*, 13–55.
- [113] Yao, M.-M.; Jiang, C.-H.; Yao, J.-S.; Wang, K.-H.; Chen, C.; Yin, Y.-C.; Zhu, B.-S.; Chen, T.; Yao, H.-B. General Synthesis of Lead-Free Metal Halide Perovskite Colloidal Nanocrystals in 1-Dodecanol. *Inorg. Chem.* **2019**, *58*, 11807–11818.
- [114] Creutz, S. E., Cri, E. N., De Siena, M. C., & Gamelin, D. R. Colloidal Nanocrystals of Lead-Free Double-Perovskite (Elpasolite) Semiconductors: Synthesis and Anion Exchange To Access New Materials. *Nano Lett.* **2018**, *18*, 1118–1123.
- [115] Locardi, F., Cirignano, M., Baranov, D., Dang, Z., Prato, M., Drago, F., Ferretti, M., Pinchetti, V., Fanciulli, M., Brovelli, S., De Trizio, L., & Manna, L. Colloidal Synthesis of Double Perovskite Cs₂AgInCl₆ and Mn-Doped Cs₂AgInCl₆ Nanocrystals. *J. Am. Chem. Soc.* **2018**, *140*, 12989–12995.
- [116] Yin, P.; Tan, Y.; Fang, H.; Hegde, M.; Radovanovic, P. V. Plasmon-Induced Carrier Polarization in Semiconductor Nanocrystals. *Nat. Nanotechnol.* **2018**, *13*, 463–467.
- [117] Jacoby, L. M., Crane, M. J., & Gamelin, D. R. Coherent Spin Dynamics in Vapor-Deposited CsPbBr₃ Perovskite Thin Films. *Chem. Mater.* **2022**, *34*, 1937–1945.

- [118] Xiang, G., Wu, Y., Zhang, M., Cheng, C., Leng, J., & Ma, H. Dimension-Dependent Bandgap Narrowing and Metallization in Lead-Free Halide Perovskite $\text{Cs}_3\text{Bi}_2\text{X}_9$ (X = I, Br, and Cl) under High Pressure. *Nanomater.* **2021**, *11*, 2712.
- [119] Yang, H., Cai, T., Liu, E., Hills-Kimball, K., Gao, J., & Chen, O. Synthesis and transformation of zero-dimensional Cs_3BiX_6 (X = Cl, Br) perovskite-analogue nanocrystals. **2020**, *Nano Res.* *13*, 282–291.
- [120] Tran, M. N., Cleveland, I. J., & Aydil, E. S. Resolving the discrepancies in the reported optical absorption of low-dimensional non-toxic perovskites, $\text{Cs}_3\text{Bi}_2\text{Br}_9$ and Cs_3BiBr_6 . *J. Mater. Chem. C* **2020**, *8*, 10456–10463.
- [121] Geng, H., Huang, Z., Geng, H., Liu, S., Naumova, M. A., Salvia, R., Chen, S., Wei, J., Zhang, L., Zou, X., Lin, W., Cai, X., Yuan, M., Hu, Z., Shen, X., Yu, R., Zheng, K., Canton, S. E., & Fu, X. Controlled synthesis of highly stable lead-free bismuth halide perovskite nanocrystals: Structures and photophysics. *Sci. China Mater.* **2023**, *66*, 2079–2089.
- [122] Zhang, Y., Yin, J., Parida, M. R., Ahmed, G. H., Pan, J., Bakr, O. M., Brédas, J.-L., & Mohammed, O. F. Direct-Indirect Nature of the Bandgap in Lead-Free Perovskite Nanocrystals. *J. Phys. Chem. Lett.* **2017**, *8*, 3173–3177.
- [123] Ji, Y.; She, M.; Bai, X.; Liu, E.; Xue, W.; Zhang, Z.; Wan, K.; Liu, P.; Zhang, S.; Li, J. In-Depth Understanding of the Effect of Halogen-Induced Stable 2D Bismuth-Based perovskites for Photocatalytic Hydrogen Evolution Activity. *Adv. Funct. Mater.* **2022**, *32*, 2201721.
- [124] Pradeep Raja Anandan, Nadeem, M., Chun-Ho, L., Singh, S., Guan, X., Kim, J., Shahroki, S., Rahaman, M. Z., Geng, X., Jing-Kai, H., Nguyen, H., Hu, H., Sharma, P., Seidel, J., Wang, X., & Wu, T. Spin-Orbital Coupling in All-Inorganic Metal-Halide perovskites: the Hidden Force that Matters. *arXiv.Org.* **2023**,

- [125] Gao, M.; Zhang, Y.; Lin, Z.; Jin, J.; Folgueras, M. C.; Yang, P. The Making of a Reconfigurable Semiconductor with a Soft Ionic Lattice. *Matter*. **2021**, *4*, 3874–3896.
- [126] Jin, J., Quan, L. N., Gao, M., Chen, C., Guo, P., & Yang, P. Octahedral Distortion and Excitonic Behavior of Cs₃Bi₂Br₉ Halide Perovskite at Low Temperature. *J. Phys. Chem. C* **2023**, *127*, 3523–3531.
- [127] Bekenstein, Y., Dahl, J. C., Huang, J., Osowiecki, W. T., Swabeck, J. K., Chan, E. M., Yang, P., & Alivisatos, A. P. The Making and Breaking of Lead-Free Double Perovskite Nanocrystals of Cesium Silver–Bismuth Halide Compositions. *Nano Lett.* **2018**, *18*, 3502–3508.
- [128] Ghebouli, M. A., Chihi, T., Ghebouli, B., & Fatmi, M. Study of the structural, elastic, electronic and optical properties of lead free halide double perovskites Cs₂AgBiX₆(X = Br, Cl). *Chin. J. Phys.* **2018**, *56*, 323–330.
- [129] Filip, M. R., Hillman, S., Haghighirad, A. A., Snaith, H. J., & Giustino, F. Band Gaps of the Lead-Free Halide Double perovskites Cs₂BiAgCl₆ and Cs₂AgBiBr₆ from Theory and Experiment. *J. Phys. Chem. Lett.* **2016**, *7*, 2579–2585.
- [130] Dey, A., Richter, A. F., Debnath, T., Huang, H., Polavarapu, L., & Feldmann, J. Transfer of Direct to Indirect Bound Excitons by Electron Intervalley Scattering in Cs₂AgBiBr₆ Double Perovskite Nanocrystals. *ACS Nano*, **2020**, *14*, 5855–5861.
- [131] Lv, C., Yang, X., Shi, Z., Wang, L., Sui, L., Li, Q., Qin, J., Liu, K., Zhang, Z., Li, X., Lou, Q., Yang, D., Zang, J., Liu, R., Liu, B., & Shan, C.-X. Pressure-Induced Ultra-Broad-Band Emission of a Cs₂AgBiBr₆ Perovskite Thin Film. *J. Phys. Chem. C* **2020**, *124*, 1732–1738.
- [132] Zelewski, S. J., Urban, J. M., Surrente, A., Maude, D. K., Kuc, A., Schade, L., Johnson, R. D., Dollmann, M., Nayak, P. K., Snaith, H. J., Radaelli, P., Kudrawiec,

- R., Nicholas, R. J., Plochocka, P., & Baranowski, M. Revealing the nature of photoluminescence emission in the metal-halide double perovskite Cs₂AgBiBr₆. *J. Mater. Chem. C* **2019**, *7*, 835–8356.
- [133] Wright, A. D., Buizza, L. R. V., Savill, K. J., Longo, G., Snaith, H. J., Johnston, M. B., & Herz, L. M. Ultrafast Excited-State Localization in Cs₂AgBiBr₆ Double Perovskite. *J. Phys. Chem. Lett.* **2021**, *12*, 3352–3360.
- [134] Li, T., Zhao, X., Yang, D., Du, M.-H., & Zhang, L. Intrinsic Defect Properties in Halide Double perovskites for Optoelectronic Applications. *Phys. Rev. Appl.* **2018**, *10*.
- [135] Wu, C., Zhang, Q., Liu, Y., Luo, W., Guo, X., Huang, Z., Ting, H., Sun, W., Zhong, X., Wei, S., Wang, S., Chen, Z., & Xiao, L. The Dawn of Lead-Free Perovskite Solar Cell: Highly Stable Double Perovskite Cs₂AgBiBr₆ Film. *Adv. Sci.* **2018**, *5*, 1700759.
- [136] Song, F.-L.; Wang, Y.-N.; Zhang, F.; Wu, S.-Y.; Xie, X.; Yang, J.-N.; Sun, S.-B.; Dang, J.-C.; Xiao, S.; Yang, L.-L.; Zhong, H.-Z.; Xu, X.-L. The g-Factor Anisotropy of Trapped Excitons in CH₃NH₃PbBr₃ Perovskite. *Acta Phys. Sin.* **2020**, *69*, 167102-1.
- [137] Steele, J. A., Puech, P., Keshavarz, M., Yang, R., Banerjee, S., Debroye, E., Kim, C. W., Yuan, H., Heo, N. H., Vanacken, J., Walsh, A., Hofkens, J., & Roeffaers, M. B. J. Giant Electron–Phonon Coupling and Deep Conduction Band Resonance in Metal Halide Double Perovskite. *ACS Nano*. **2018**, *12*, 8081–8090.
- [138] Fransson, J. Chiral phonon induced spin polarization. *Phys. Rev. Res.* **2023**, *5*, L022039.
- [139] Biswas, S., Zhao, R., Alowa, F., Zacharias, M., Sharifzadeh, S., Coker, D. F., Seferos, D. S., & Scholes, G. D. Exciton polaron formation and hot-carrier relaxation in rigid Dion-Jacobson-type two-dimensional perovskites. *Nat. Mater.* **2024**, *23*, 937–943.

- [140] Lei, H., Hardy, D., & Gao, F. Lead-Free Double Perovskite Cs₂AgBiBr₆ Fundamentals, Applications, and Perspectives. *Adv. Funct. Mater.* **2021**, 31, 2105898.
- [141] Mandal, P., & Viswanatha, R. Probing of Excitonic Transitions in All Inorganic Perovskite Quantum Dots (CsPbX₃: X= Cl, Br, I) by Magnetic Circular Dichroism Spectroscopy. **2023**, *arXiv:2311.12567*.
- [142] Najafi A, Sharma M, Delikanli S, Bhattacharya A, Murphy JR, Pientka J, Sharma A, Quinn AP, Erdem O, Kattel S, Kelestemur Y, Kovalenko MV, Rice WD, Demir HV, Petrou A. Light-Induced Paramagnetism in Colloidal Ag⁺-Doped CdSe Nanoplatelets. *J Phys Chem Lett.* **2021**, 12:2892-2899.
- [143] Manna, D., Das, T. K., & Yella, A. Tunable and Stable White Light Emission in Bi³⁺-Alloyed Cs₂AgInCl₆ Double Perovskite Nanocrystals. *Chem. Mater.* **2019**, 31, 10063–10070.
- [144] Han, P., Zhang, X., Mao, X., Yang, B., Yang, S., Feng, Z., Wei, D., Deng, W., Pullerits, T., & Han, K. Size effect of lead-free halide double perovskite on luminescence property. *Sci. China Chem.* **2019**, 62, 1405–1413.
- [145] Kale, A. J., Chaurasiya, R., & Dixit, A. Lead-Free Cs₂BB'X₆ (B: Ag/Au/Cu, B': Bi/Sb/Tl, and X: Br/Cl/I) Double perovskites and Their Potential in Energy Conversion Applications. *ACS Appl. Energy Mater.* **2022**, 5, 10427–10445.
- [146] Ran, Z., Wang, X., Li, Y., Yang, D., Zhao, X. G., Biswas, K., Singh, D. J., & Zhang, L. Bismuth and antimony-based oxyhalides and chalcogenides as potential optoelectronic materials. *npj Comput. Mater.* **2018**, 4, 1–7.

Appendix

Appendix A

Deconvolution for vacancy-ordered perovskites NCs

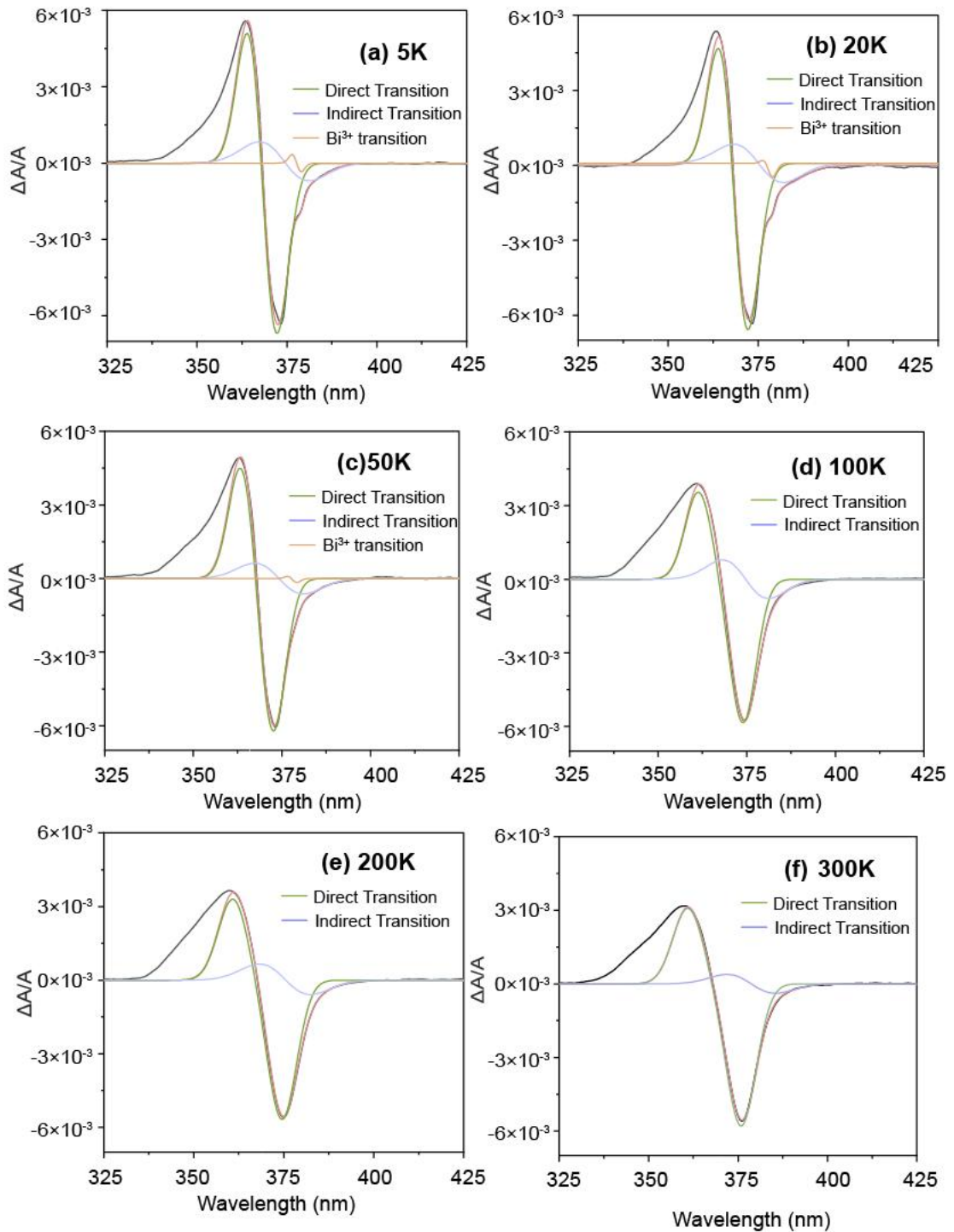


Figure A.1. MCD spectra of $\text{Cs}_3\text{Bi}_2\text{Cl}_9$ collected at (a) 5 K (b) 20 K (c) 50 K (d) 100 K (e) 200 K (f) 300 K. (Legend: black line - normalized MCD data; pink line - cumulative peak; green line - simulated direct transition; purple line - simulated indirect transition; orange line - Bismuth s-p transition)

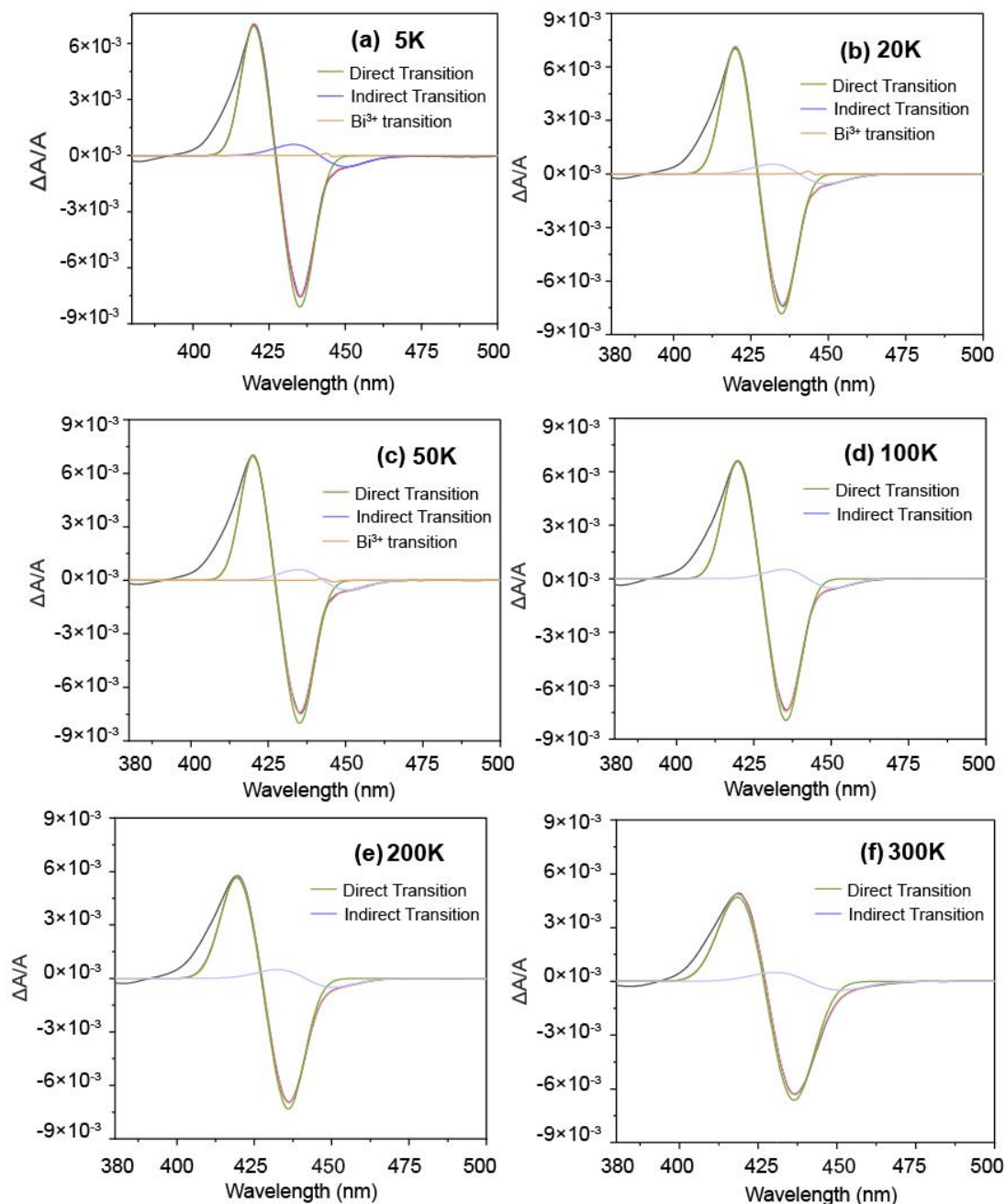


Figure A.2. MCD spectra of $\text{Cs}_3\text{Bi}_2\text{Br}_9$ collected at (a) 5 K (b) 20 K (c) 50 K (d) 100 K (e) 200 K (f) 300 K. (Legend: black line - normalized MCD data; pink line - cumulative peak; green line - simulated direct transition; purple line - simulated indirect transition; orange line - Bismuth s-p transition)

Appendix B

Deconvolution for double perovskites NCs

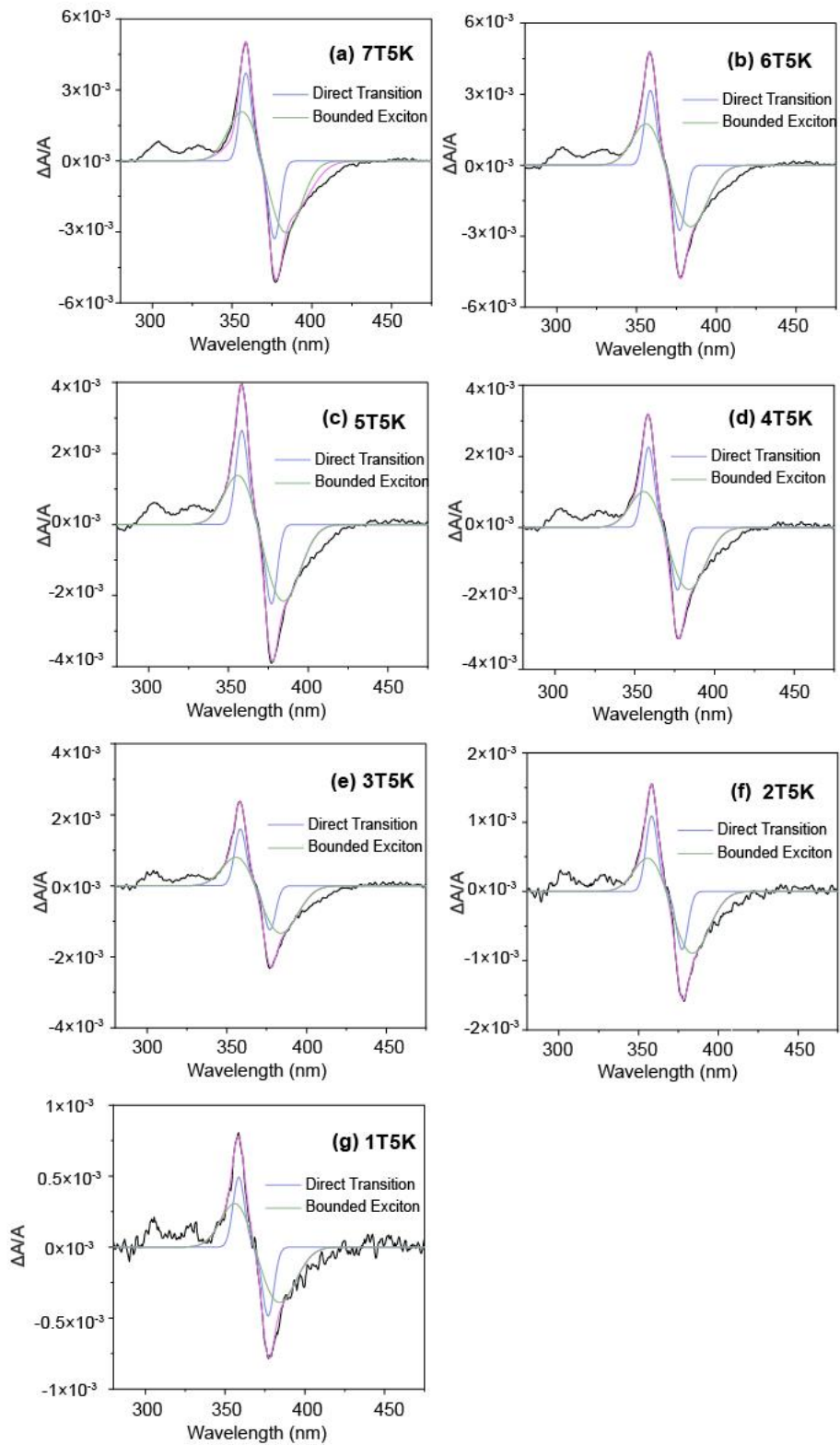


Figure B.1. MCD spectra of Cs₂AgBiCl₆ collected at (a) 5 K-7 T (b) 5 K-6 T (c) 5 K-5 T (d) 5 K-4 T (e) 5 K-3 T (f) 5 K-2 T (g) 5 K-1 T. (Legend: black line - normalized MCD data; pink line - cumulative peak; blue line - simulated direct transition; green line - simulated bound exciton transition)

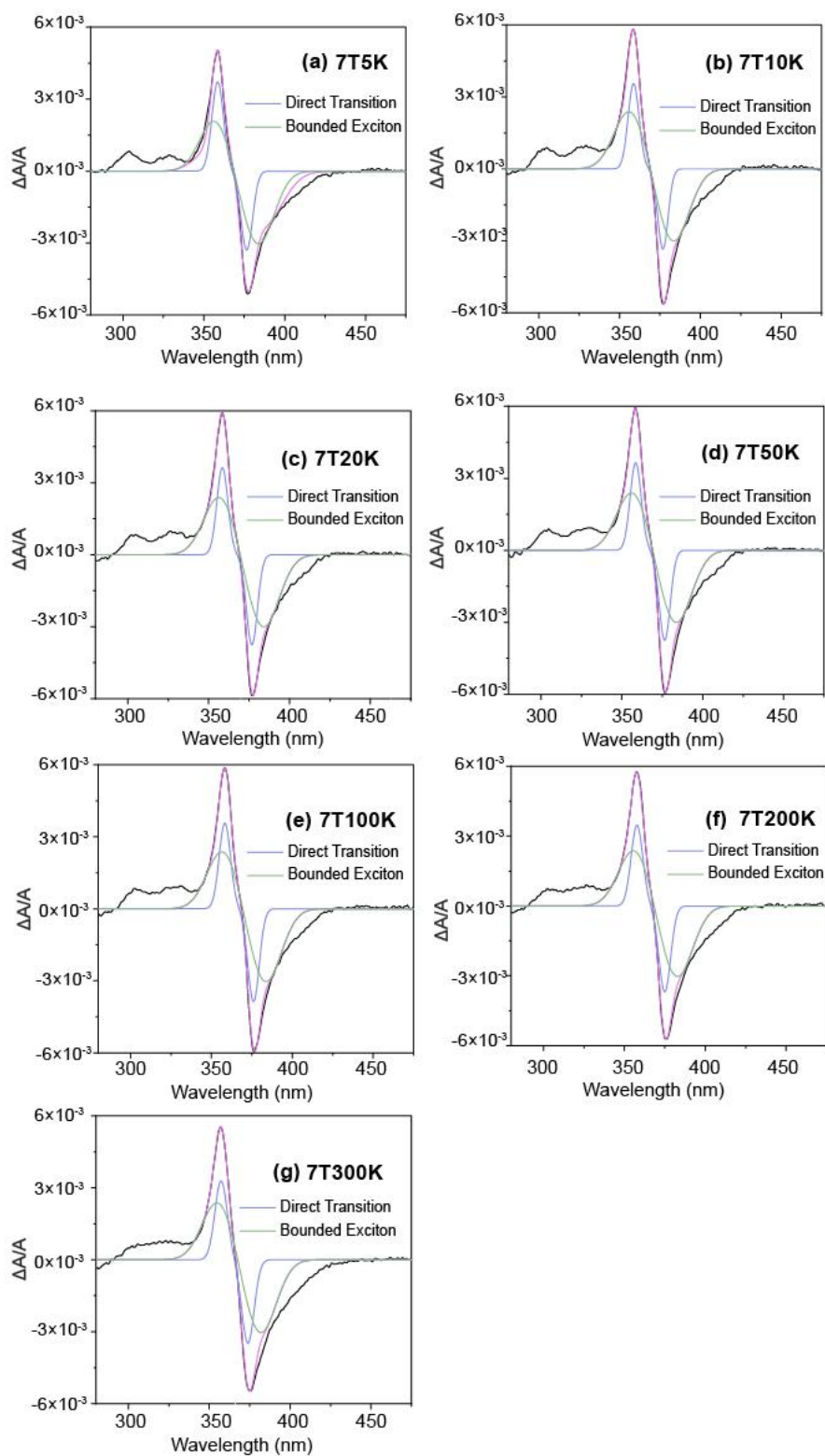


Figure B.2. MCD spectra of $\text{Cs}_2\text{AgBiCl}_6$ collected at (a) 5 K (b) 10 K (c) 20 K (d) 50 K (e) 100 K (f) 200 K (g) 300 K. (Legend: black line - normalized MCD data; pink line - cumulative peak; blue line - simulated direct transition; green line - simulated bound exciton transition)

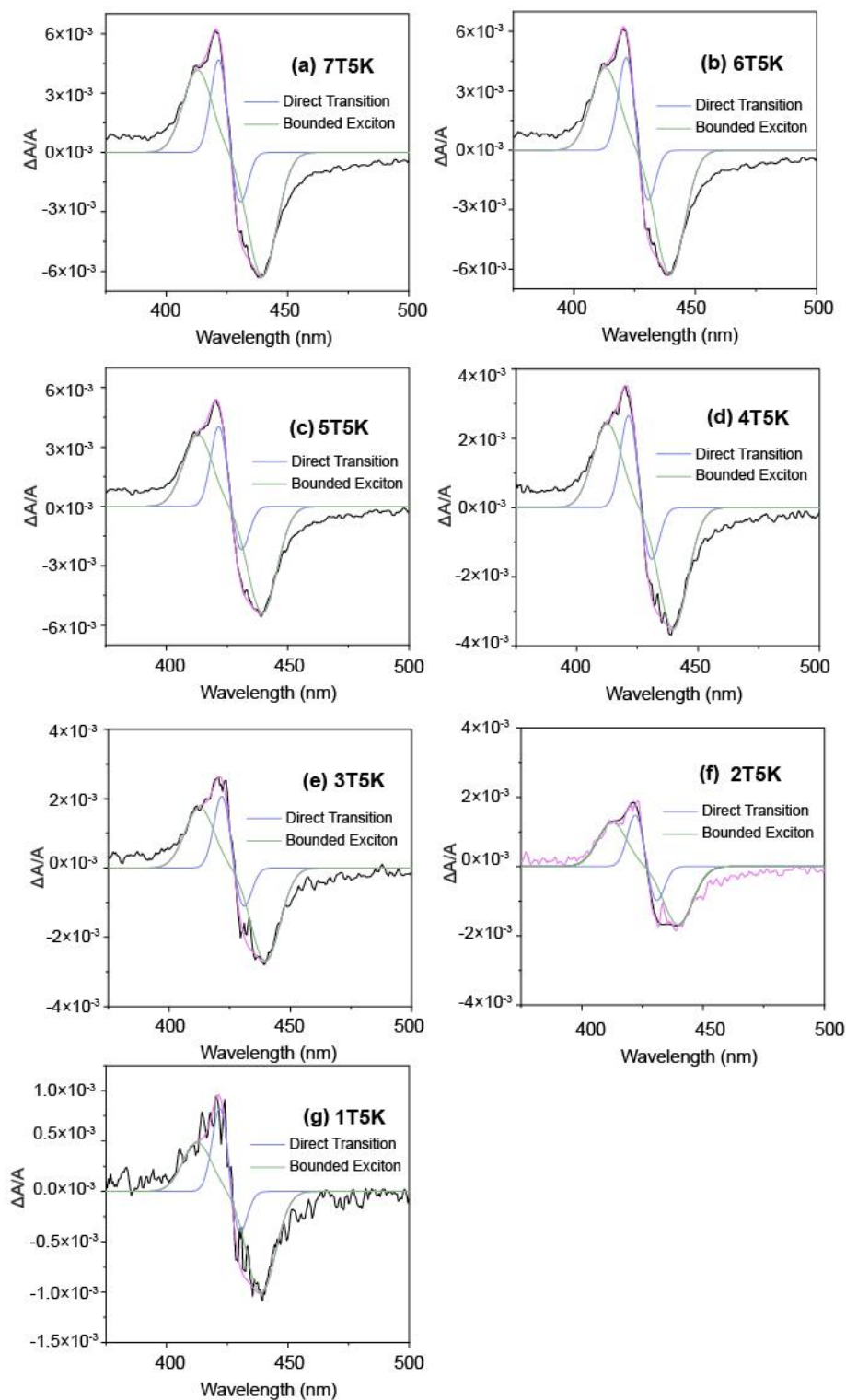


Figure B.3. MCD spectra of Cs₂AgBiBr₆ collected at (a) 5 K-7 T (b) 5 K-6 T (c) 5 K-5 T (d) 5 K-4 T (e) 5 K-3 T (f) 5 K-2 T (g) 5 K-1 T. (Legend: black line - normalized MCD data; pink line - cumulative peak; blue line - simulated direct transition; green line - simulated bound exciton transition)

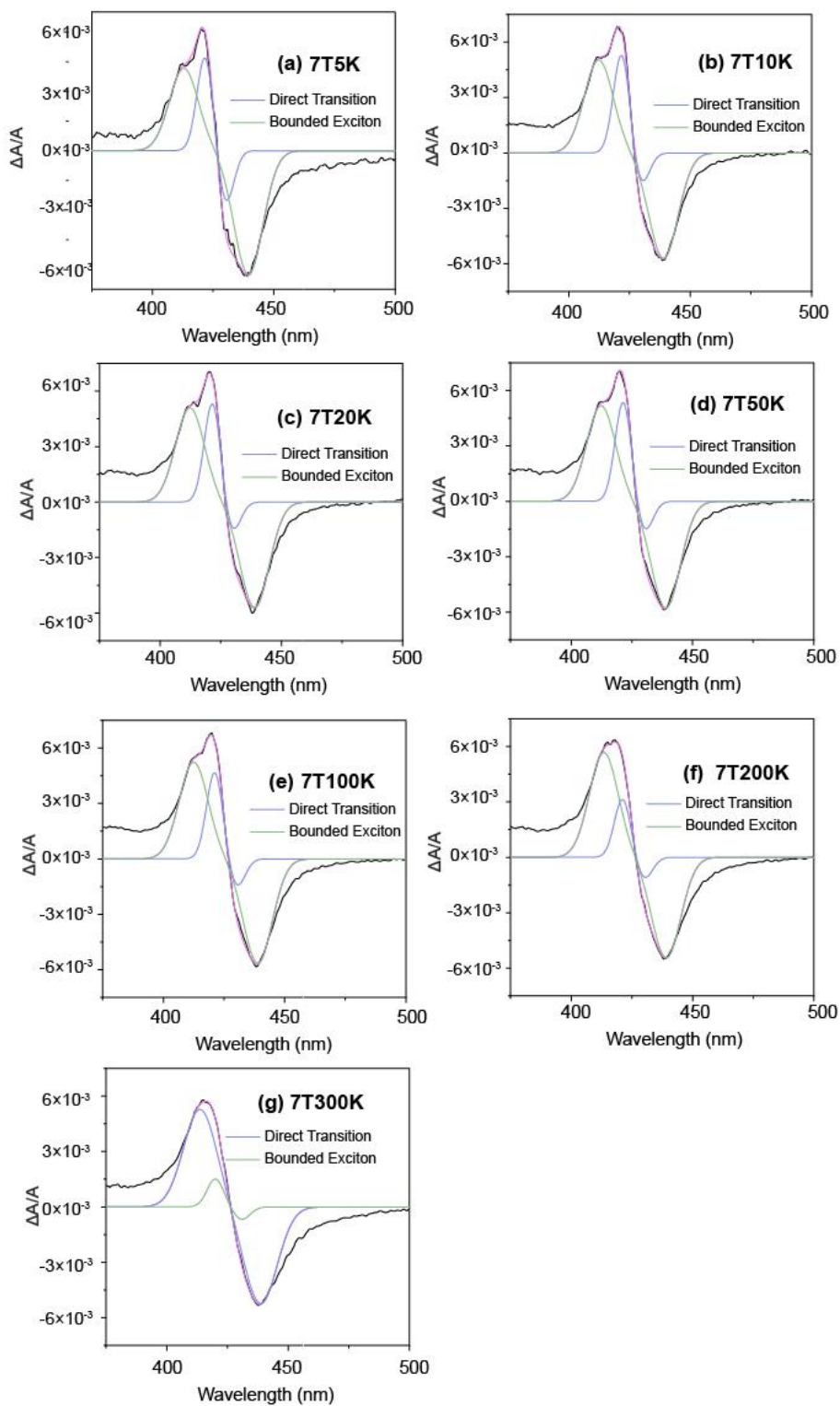


Figure B.4. MCD spectra of Cs₂AgBiBr₆ collected at (a) 5 K (b) 10 K (c) 20 K (d) 50 K (e) 100 K (f) 200 K (g) 300 K. (Legend: black line - normalized MCD data; pink line - cumulative peak; blue line - simulated direct transition; green line - simulated bound exciton transition)

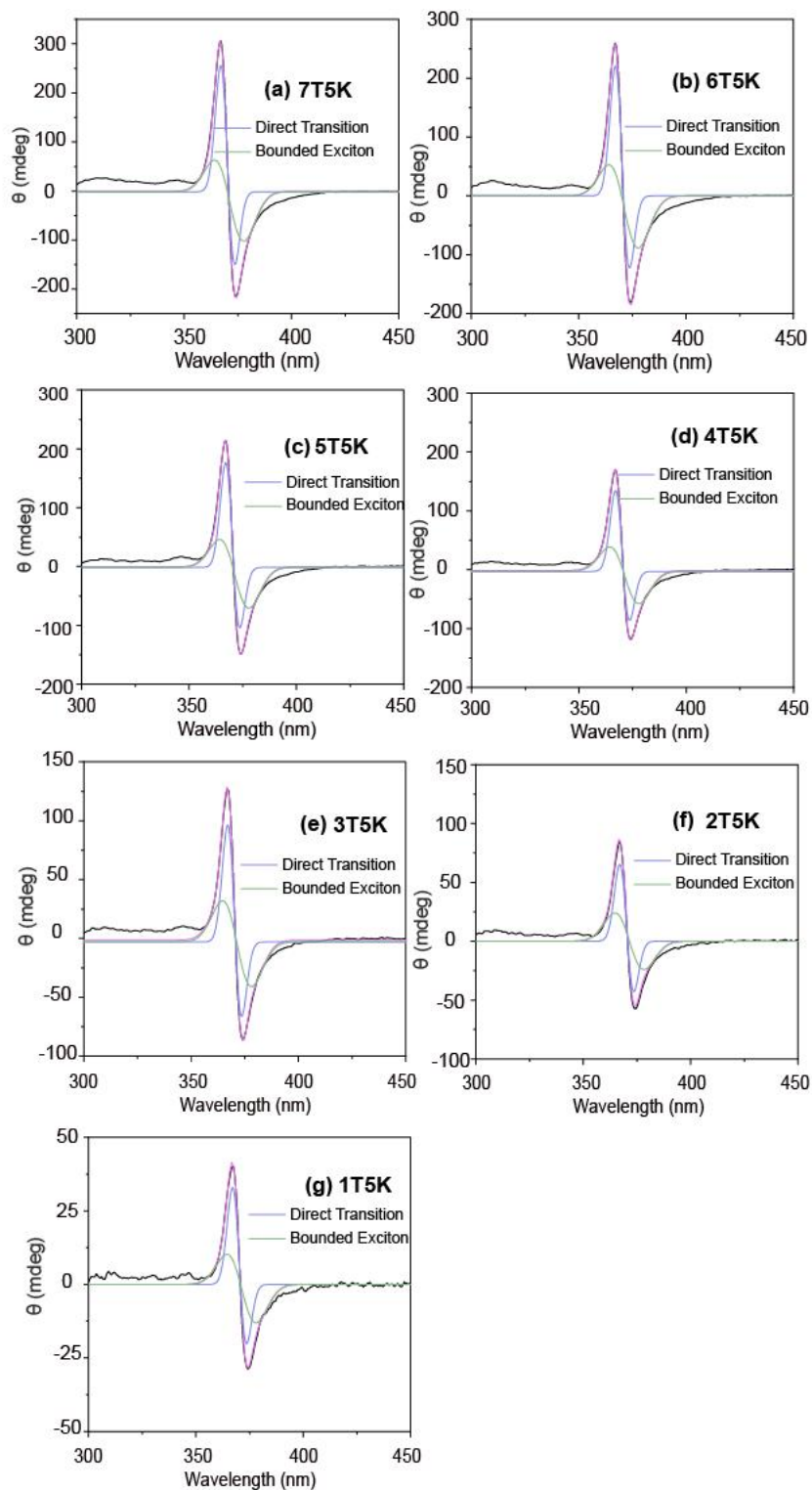


Figure B.5. MCD spectra of $\text{Cs}_2\text{AgIn}_{0.5}\text{Bi}_{0.5}\text{Cl}_6$ collected at (a) 5 K-7 T (b) 5 K-6 T (c) 5 K-5 T (d) 5 K-4 T (e) 5 K-3 T (f) 5 K-2 T (g) 5 K-1 T. (Legend: black line - MCD data; pink line - cumulative peak; blue line - simulated direct transition; green line - simulated bound exciton transition)

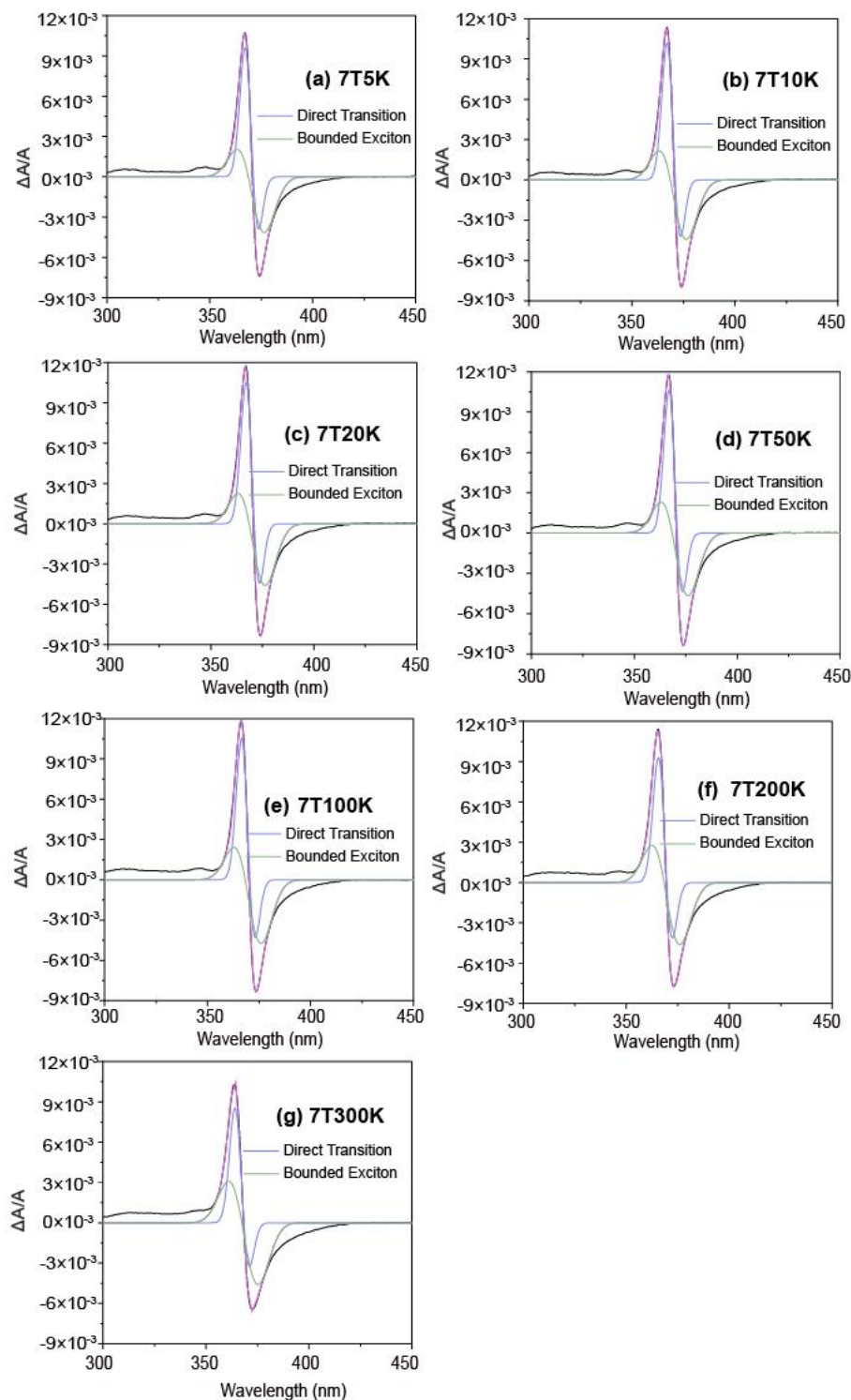


Figure B.6. MCD spectra of $\text{Cs}_2\text{AgIn}_{0.5}\text{Bi}_{0.5}\text{Cl}_6$ collected at (a) 5 K (b) 10 K (c) 20 K

(d) 50 K (e) 100 K (f) 200 K (g) 300 K. (Legend: black line - normalized MCD data; pink line - cumulative peak; blue line - simulated direct transition; green line - simulated bound exciton transition)